Large-eddy Spray Simulation under Direct-injection Spark-ignition Engine-like Conditions

By

Hongjiang Li

A dissertation submitted in partial fulfillment of
the requirements for the degree of

Doctor of Philosophy

(Mechanical Engineering)

at the

UNIVERSITY OF WISCONSIN–MADISON

2019

Date of final oral examination: 1/8/2019

The dissertation is approved by the following members of the Final Oral Committee:

Christopher J. Rutland, Phil & Jean Myers Professor, Mechanical Engineering
David A. Rothamer, Associate Professor, Mechanical Engineering
Mario F. Trujillo, Associate Professor, Mechanical Engineering
Sage L. Kokjohn, Assistant Professor, Mechanical Engineering
Samuel N. Stechmann, Professor, Mathematics

"He who learns but does not think, is lost!

He who thinks but does not learn is in great danger."

— Confucius

ACKNOWLEDGMENTS

First and most, I like to express my deep gratitude to my advisor, Professor Christopher J. Rutland, for his support and constructive feedback in my work, and the freedom he left me in exploring and in finding out an interesting topic I have studied. I learned a great deal from him. Being his graduate student has truly been an enjoyable and rewarding experience.

I would also like to thank my committee members: Professors David Rothamer, Mario Trujillo, Sage Kokjohn in the Engine Research Center and Professor Samuel Stechmann in the Math department, for their insights and useful critiques.

I wish to thank Joshua Leach, for his technical support; Professor Noah Van Dam, for sharing with me the DISI meshes used in this work, Dr. Chi-wei Tsang, for helping me set up the OpenFOAM code, and Dr. Federico Perini, for sharing with me his Speed-CHEM fast-chemistry solver. Working with the other ERC students generated many good memories over the last five years. To name a few, they are Dr. Yangdongfang Yang, Dr. Zhenkuo Wu, Dr. Yaopeng Li, Dr. Zongyu Yue, Xinlei Liu, Jing Li, Tyler Strickland, Jonathan Blanco, and Arun Ravindran.

I appreciate the financial support for my graduate study from the China Scholarship Council and the Wisconsin Engine Research Consultants. Special thanks for the discussions with and the support from Professor Hong G. Im and Dr. Francisco E. Hernández Pérez in the Clean Combustion Research Center at the King Abdullah University of Science and Technology.

Finally, I would like to thank my family for their endless love and support. I am deeply indebted to my girlfriend, Shujin, for her incredible patience and selfless support.

CONTENTS

LIST OF TABLES

LIST OF FIGURES

NOMENCLATURE

Acronyms

NS Number of species

ADM Approximate Deconvolution Method

CPBLS Combined Primary Breakup and Lagrange Spray

DBI Diffused Back-illumination Imaging

DDB Droplet Deformation and Breakup

DDF Droplet Distribution Function

DISI Direct-injection Spark-ignition

DNS Direct Numerical Simulation

DRW Discrete Random Walk

ECN Engine Combustion Network

ERC Engine Research Center

GDI Gasoline Direct Injection

GM General Motors

HPC High-performance Computing

KH Kelvin-Helmholtz

LE Lagrangian-Eulerian

LES Large-eddy Simulation

LHS Latin-hypercube Sampling

LISA Linearized Instability Sheet Atomization

MC Monte Carlo

MMC Mimic Mie-scatter

NSRDS National Standard Reference Data System

PCE Polynomial Chaos Expansion

PDF Probability Distribution Function

PDPA Phase Doppler Particle Analyzer

PFI Port Fuel Injection

PLV Projected Liquid Volume

RANS Reynolds-averaged Navier–Stokes

ROI Rate of Injection

RT Rayleigh-Taylor

SDE Stochastic Differential Equation

SGS Sub-grid Scale

SIDI Spark-ignition Direct-injection

SMD Sauter Mean Diameter

TAB Taylor Analogy Breakup

UQ Uncertainty Quantification

VBD Variance-Based Decomposition

VOF Volume of Fluid

Greek Symbols

α Thermal diffusivity

χ Resolved species flux

Δ Filter width

ϵ Normalized drift velocity

γ Scaling factor in the SGS energy dissipation rate model

Γ_{ij} Molecular stress tensor

λ Droplet stretching rate

Λ_{KH} Wavelength of the fastest-growing KH instability wave

Λ_{RT} Wavelength of the fastest-growing RT instability wave

μ Viscosity (default phase: gas)

μ_C Characteristic viscosity in the SGS energy dissipation rate model

ν Kinematic viscosity (default phase: gas)

Ω_{KH} Frequency of the fastest-growing KH instability wave

Ω_{RT} Frequency of the fastest-growing RT instability wave

Φ^{sgs} SGS species flux

Ψ Multivariate polynomials

ρ Density (default phase: gas)

σ Surface tension

τ_{bag} Reduced time of bag rupture

τ_{disp} Characteristic time scale in the SGS turbulent dispersion model

τ_{KH} KH breakup time

τ_{RT} RT breakup time

τ_e Eddy lifetime

τ_i Droplet-eddy interaction time

τ_p Characteristic time for a droplet to pass an eddy

τ_{ij}^{sgs} SGS stress tensor

υ Scaling factor in the SGS energy dissipation rate model

ϱ Pearson's correlation coefficient

ξ Random variable

ζ Mode strength

h_f° Enthalpy of formation

L_v Latent heat of vaporization

Q Droplet surface heat flux

u_C Characteristic velocity in the DRW model

Non-dimensional parameters

Oh Ohnesorge number

Re Reynolds number

Ta Taylor number

We Weber number

Operators

$\bar{\ }$ Mean

$\circledast$ Convolution operator

$\ddot{\ }$ Double derivative with respect to time

$\dot{\ }$ Derivative with respect to time

$\| \|_\infty$ Infinity norm

$\mathbb{R}^3$ Set of real numbers

$\sim$ Logical negation

$\sum_d$ Summation of all droplets within a mesh cell

$\widehat{\ }$ Test-level filtering operator

$\widetilde{\ }$ Density weighted average(i.e., Favre filtering)

$E[\cdot \mid \cdot]$ Conditional expected value

$E[\cdot]$ Expected value

$V(\cdot)$ Expected variance

$V(\cdot \mid \cdot)$ Conditional expected variance

Roman Symbols

$\mathcal{V}$ Filter volume

$\mathrm{d}W_i$ An increment of the Wiener process

ϕ_{bag} Volume fraction of the liquid bag when it ruptures

θ Plume direction (i.e., spray-axis angle)

$\mathrm{We}_{\mathrm{bag}}$ Transitional We for bag breakup

$\mathrm{We}_{\mathrm{crit}}$ Critical We for droplet breakup

a Droplet acceleration

B_0 Characteristic size constant in the KH breakup model

B_1 Characteristic time constant in the KH breakup model

C_1 Parameter in the bag growth model

C_2 Parameter in the bag growth model

C_{bag} Parameter in the bag growth model

C_β RT breakup length constant in the IAB model

C_{disp} Coefficient in the calculation of τ_{disp}

C_ϵ Parameter in the SGS energy dissipation rate model

C_{RT} Characteristic size constant in the RT breakup model

C_{sgs} Parameter in the SGS energy dissipation rate model

C_τ Characteristic time constant in the RT breakup model

C_a Area contraction coefficient

C_B RT breakup length constant in the KH-RT model

C_D Discharge coefficient

C_d Droplet drag coefficient

C_k Parameter in the SGS energy dissipation rate model

C_p Specific heat

C_V Velocity coefficient

$C_{\tau,\text{bag}}$ Characteristic time constant in the bag rupture model

$C_{h,\text{bag}}$ Characteristic size constant in the bag rupture model

c_{ij} SGS stress tensor coefficient

d_c Child droplet diameter

d_r Tube diameter of the torus ring

F Scaling function in the SGS energy dissipation rate model

F_d Droplet drag force

G Filter convolution kernel

g Gravitational force

G^{-1} Inverse of the filter kernel

h Liquid disk thickness

h^{sgs} SGS heat flux

h_s Sensible enthalpy

K Resolved kinetic energy

k_{sgs} SGS kinetic energy

L_B RT breakup length

m Mass

n_c Number of child droplets

P Pressure (default phase: gas)

P_{stag} Liquid pressure at the front stagnation point of a deforming droplet

$P_{\kappa_{max}}$ Liquid pressure at the liquid-gas border where the curvature is the maximum

q Heat transfer rate

Q_{chem} Chemical reaction heat release rate

S_{ij} Strain rate tensor

T Temperature (default phase: gas)

t Time

T^* Characteristic time in the bag growth model

t^* Reduced time

u Velocity vector

u_g Instantaneous gas-phase velocity seen by droplet

u_i Fluctuating part of instantaneous gas-phase velocity

u_i^* Deterministic part of instantaneous gas-phase velocity

$u_{k,\mathrm{sgs}}$ Characteristic SGS velocity

v Velocity vector

x Position vector

Y Specie mass fraction

d Diameter

M Number of terms

S Main effect sensitivity index

T Total effect sensitivity index

U Velocity magnitude

X Response variable

Sub-/Superscripts

Rel Relative quantity between liquid- and gas-phase

noz Nozzle

0 Initial conditions

bag Liquid bag

d Droplet

g Gas-phase

l Liquid-phase

ABSTRACT

The focus of this dissertation is on the development and improvement of spray models for large-eddy simulation (LES) of turbulent two-phase flows in direct-injection spark-ignition (DISI) engines. The work can be regarded as a continuation of the development of LES framework at the Engine Research Center (ERC). The LES two-phase governing equations are solved using the Lagrangian-Eulerian (LE) approach in a variation of the OpenFOAM-2.3.x code developed by the OpenFOAM Foundation. A mixed-type one-equation dynamic structure turbulence model is used as the basis for turbulence modeling.

LES models are developed for DISI spray breakup, Sub-grid scale (SGS) turbulent dispersion, and SGS energy dissipation rate. The spray breakup model builds on top of the hybrid Kelvin-Helmholtz (KH)/Rayleigh-Taylor (RT) model by incorporating the bag/bag-stamen breakup regimes. A concept of RT breakup length is introduced to account for the plume-interactions and the effective nozzle diameter of DISI spray. The SGS models are developed in the context of LES and require the SGS kinetic energy, which is obtained by solving its transport equation in the turbulence model.

The performance of the new models is evaluated against a wide range of DISI spray experiments covering both early and late injection engine-like conditions. Examination of spray characteristics is performed for both global and local quantities such as penetration length, Sauter mean diameter (SMD), droplet velocity, liquid-phase concentrations, and spray envelop. The discussion focuses primarily on the DISI spray breakup, followed by *a posteriori* test results of the SGS models. An uncertainty quantification (UQ) study is also performed to analyze the impact of spray boundary conditions and breakup model

parameters on LES of DISI sprays.

LES results show that the addition of models for bag/bag-stamen breakup regimes results in more accurate predictions of spray characteristics. The modified breakup length concept also predicts more realistic penetration curves across a range of ambient temperature and density conditions without tuning the model parameters. The improved SGS dispersion model correctly predicts local liquid-phase characteristics such as velocity and projected liquid volume fraction. A preliminary study of SGS dissipation rate modeling also shows that the SGS model is able to accurately predict the energy balance between the resolved and the SGS fields across various mesh resolutions.

1 INTRODUCTION

1.1 Motivation

DISI engines, also known as gasoline direct injection (GDI [1]) or spark-ignition direct-injection (SIDI) engines, offer many advantages over contemporary port-fuel injection (PFI) engines such as [1]:

- Improved fuel economy due to less pumping loss, higher compression ratio, and increased volumetric efficiency,
- Precise fuel metering and air-fuel ratio control,
- Reduction in cold-start emissions.

Successfully realization of above benefits relies heavily on the quality of fuel injection and subsequent air-fuel mixing, especially for the spray-guided stratified charge combustion systems, in which precise matching between the mixture formation and spark location is essential for stable combustion and optimal performance.

The injector is the key component of DISI fuel injection systems and its design needs to meet more stringent requirements than that of the port-fuel injector. Modern DISI injectors have multi-hole design similar to that used in diesel engines. Spray characteristics of such configuration have been proven to have less dependence on ambient conditions, unlike the swirl-type injectors. Multi-hole injectors also have the flexibility to direct spray plumes at desired locations, which helps meet the combustion system require-

[1] Although been widely used for many years, the acronym "GDI" is actually a registered trademark of Mitsubishi Motors Corporation.

ments. On the other hand, DISI injectors operate at a much lower pressure compared to diesel injection system pressures, leading to several times lower liquid jet velocity at the nozzle exit. Gasoline fuel also has a lower density and viscosity than diesel fuel. As a result, the breakup process is considerably different between gasoline and diesel sprays, as has been demonstrated by previous studies [2, 3].

Despite decades of continuous efforts by researchers, the fuel atomization and breakup processes have not been thoroughly understood, especially in the near-nozzle region where experimental measurements are hardly accessible. One way to overcome this challenge is to perform high-fidelity simulations such as direct numerical simulation (DNS) to resolve the atomization completely. However, all turbulence length scales, from the smallest Kolmogorov scales to the largest integral scales, must be resolved in DNS. This requires a significant amount of computational resources that even with modern high-performance computing (HPC) systems, the engineering application of DNS is very limited.

An alternative approach is LES, which provides more detailed flow structures, eddies, and vortices compared to Reynolds-averaged Navier–Stokes (RANS). LES requires significantly less computational resources compared to DNS, and it is considered as one of the most promising approaches for modeling of high Reynolds number turbulent engine flows. The heart of LES is the filtering (i.e., spatial averaging) of variables of interests such as velocity, species concentration, and enthalpy, into resolved and unresolved parts. The resolved part, which can be computed directly, contains most of the energy, does most of the transporting work, and varies most from flow to flow [4]. The unresolved, or SGS quantities, are not directly available thus need to be modeled using SGS models.

For turbulent engine flows, LES is still a relatively new approach and thus many SGS models still follow the RANS approach. For instance, accurate description of spray development in turbulent engine flows requires the instantaneous carrier fluid velocity "seen" by liquid droplets. This carrier fluid velocity is determined not only by the resolved flow fields, but also by the local SGS flow structures. The SGS velocity therefore directly influences the droplet dispersion by determining the relative velocity magnitude between carrier phase and liquid droplets. In most LES applications to engine flows, the RANS-type stochastic dispersion approach remains the most common use. The main issue with extending this approach to LES comes from the fact that it builds on statistical averages, whereas the LES flow field is deterministic and instantaneous. Another example is the SGS energy dissipation rate, which is responsible for the energy removal from the unresolved scales. The quality of the SGS energy dissipation rate model is crucial for maintaining a correct energy budget in LES. However, modeling SGS energy dissipation rate is a challenging task. Very few models and/or semi-empirical correlations exist due to the scarce literature on experiments or DNS performed in conditions of practical interests in engine flows.

1.2 Objective and approach

The objectives of this work are twofold. First, a breakup model for use in DISI sprays will be developed, incorporating the bag/bag-stamen breakup mechanisms found in DISI sprays. Second, SGS models for turbulent dispersion and energy dissipation rate will be developed. The former will close the Lagrangian governing equations for liquid droplets, and the later will replace the ad hoc formula in the transport equation of the SGS kinetic

energy, an auxiliary LES quantity that is used in one-equation turbulent models.

The OpenFOAM-2.3.x, provided by the OpenFOAM foundation [5], is used in this study as the CFD platform to implement and test new models. Many advanced sub-models, developed at the Engine Research Center and implemented into the OpenFOAM-2.1.1 by Dr. Chi-wei Tsang [6], were adopted into this more recent version by the author. Testing of the new models is carried out using hexahedral meshes provided by Dr. Noah Van Dam [61].

The remainder of this dissertation is organized as follows. Chapter 2 provides necessary background. Chapter 3 reviews in detail the relevant work currently available. Chapter 4 contains the LES governing equations and formulation of new models. Chapter 5 then presents the results and discussions of spray tests conducted with the breakup model and SGS models, respectively. Finally, Chapter 6 summarizes this work and proposes future directions.

2 BACKGROUND

2.1 Liquid jet breakup regimes

Depending on the relative velocity and fluid properties such as density, surface tension, and viscosity, the breakup of liquid jet can be classified into four different regimes [7]. These are the Rayleigh, first wind-induced, second wind-induced, and atomization regimes. The boundaries between these four breakup regimes can be found in the Ohnesorge - Reynolds diagram shown in Figure 2.1, in which the liquid Ohnesorge and Reynolds numbers are defined as

$$\mathrm{Oh}_{\mathrm{noz}} = \frac{\mu_l}{\sqrt{\rho_l d_{\mathrm{noz}} \sigma}}, \tag{2.1}$$

$$\mathrm{Re}_{\mathrm{noz}} = \frac{U_{\mathrm{Rel}} d_{\mathrm{noz}} \rho_l}{\mu_l}, \tag{2.2}$$

where d_{noz}, ρ_l, μ_l, σ, and U_{Rel} are the nozzle diameter, liquid-phase density, liquid-phase viscosity, surface tension, and the relative velocity between the liquid jet and ambient surroundings, respectively.

Figure 2.2 presents a schematic description of the four different jet breakup regimes. If the nozzle geometry and fluid properties are fixed, then the only variable that determines the breakup regime is the relative velocity, U_{Rel}. At very low velocities, the jet breakup happens at locations many times larger than the nozzle diameter, resulting in child droplets that are larger than the nozzle diameter. Increasing the relative velocity further will cause the breakup to happen at distances close to the nozzle exit. In the first wind-induced breakup regime, child droplets are formed with diameters of the order of

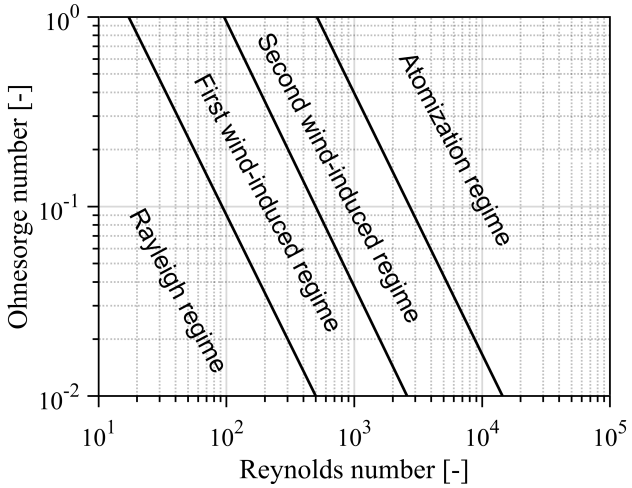

Figure 2.1: Jet breakup regimes as functions of Reynolds and Ohnesorge numbers [8].

nozzle diameter. In the second wind-induced and atomization regimes, liquid jet breaks due to unstable surface waves initiated by turbulent in-nozzle flows and amplified by aerodynamic drag forces. Breakup starts at some nozzle diameters downstream of the nozzle, and the child droplets are smaller than the nozzle diameter.

The major difference between second wind-induced and atomization regimes is that in the atomization regime, the breakup happens immediately after the jet leaves the nozzle exit. As shown in Figure 2.2, there may still be a small conical region where an intact liquid core presents. Among all jet breakup regimes, only the atomization is relevant to engine sprays, due to the high injection pressures of modern fuel injection systems.

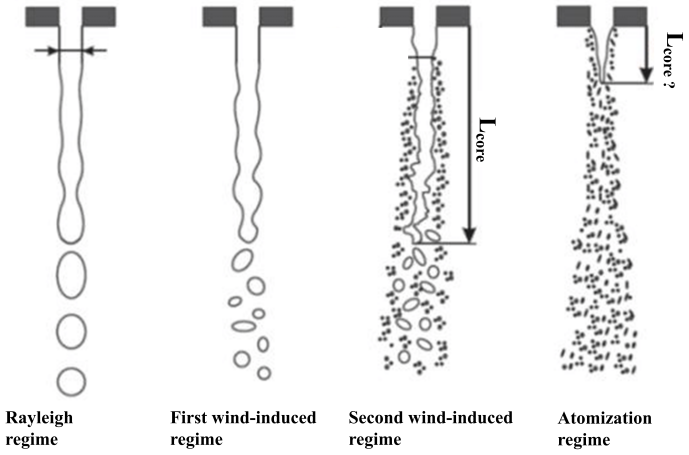

Figure 2.2: Schematic illustration of jet breakup regimes [9].

2.2 Droplet breakup regimes

When a droplet forms from atomization at or near the nozzle exit, the aerodynamic force causes the droplet to deform and break into fragments. On the other hand, surface tension force tends to resist the deformation and restore the droplet to a spherical shape. As a result, the ratio of aerodynamic force to surface tension force, defined as the We number, becomes the most important non-dimensional parameter when describing the droplet breakup. Another widely used non-dimensional number is the Oh number, which is defined in Equation 2.1 using the droplet diameter. Definitions of We and Oh are written as

$$\mathrm{We} = \frac{\rho U_{\mathrm{Rel}}^2 d_d}{\sigma}, \tag{2.3}$$

$$\mathrm{Oh} = \frac{\mu_l}{\sqrt{\rho_l d_d \sigma}}, \tag{2.4}$$

where ρ, d_d are the gas-phase density and droplet diameter, respectively.

Depending on the values of We and Oh numbers, the physics involved in droplet breakup can be very different. Various researchers have identified multiple breakup regimes through experimental studies involving droplets exposed to disruptive gas flow fields. Those experiments were mainly carried out in shock tubes and wind tunnels. Classic references on this topic are those of Pilch and Erdman [10], Krzeczkowski [11], Faeth *et al*. [12–17], Reitz *et al*. [18, 19], Opfer *et al*. [20], Theofanous *et al*. [21], Gelfand [22], and the theoretical work of Girin [23]. It has been generally accepted that the transitions among different breakup regimes are continuous functions of We and Oh numbers [24]. Figure 2.3 presents the Weber - Ohnesorge diagram of droplet breakup mechanisms, where five regimes are identified. Note that the transitions are nearly independent of Oh for Oh less than 0.1 [14]. In the diagram, We–Oh regimes of typical gasoline and diesel sprays are marked with dashed and dotted lines, respectively. Clearly, there is only a small overlap between diesel and gasoline sprays, and the governing breakup mechanisms between them are quite different. While the majority of diesel sprays break due to either catastrophic or sheet-thinning mechanisms, only a small amount of gasoline sprays reaches to the sheet-thinning regime. In fact, most of the gasoline sprays break due to multi-mode or bag mechanisms, some of them even touch the lowest end of the map – the oscillation/deformation breakup regime.

Breakup regimes and the associated transition We numbers reported in various experiments are summarized in Table 2.1. The inconsistencies in reported We values among listed studies are primarily due to the experimental uncertainties (non-sphericity of droplets and uncertainties associated with velocity measurements) and the fact that the

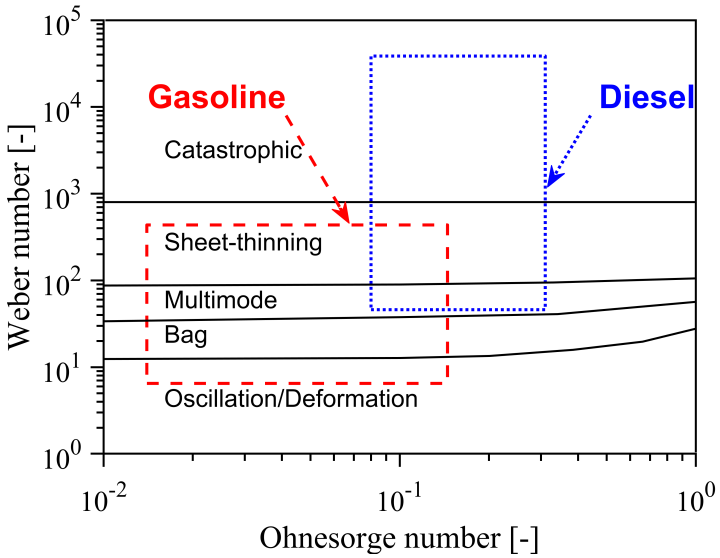

Figure 2.3: Map of droplet breakup regimes as functions of Weber and Ohnesorge numbers [25]. The breakup regimes of typical gasoline and diesel sprays are enclosed by dashed and dotted lines, respectively.

transitions are continuous processes. Each breakup regime will be discussed in detail in the following sections.

Oscillation and deformation breakup

The first stage of droplet breakup is droplet deforming into an oblate spheroid shape, normally aligned to the gas flow direction. This is caused by the unequal pressure distribution over the droplet surface when a spherical droplet enters a disruptive gas field. If the aerodynamic force is comparable to the surface tension force, oscillation may develop at the natural frequency of the droplet. Under certain conditions, the oscillation becomes unstable and leads to droplet breakup [24]. However, this does not happen in every instance, and even when it occurs, the overall breakup time is much longer com-

Table 2.1: Breakup regimes and associated transition We numbers identified in various experimental studies. Note that the listed breakup regimes maybe termed differently in the reported work. For simplicity, the names of these regimes have been changed to those commonly used today.

	Oscillation Deformation	Bag	Bag-Stamen	Plume/Sheet -thinning	Sheet thinning	Catastrophic
			Multi-Mode			
Pilch and Erdman [10]	$We < 12$	$12 < We < 50$	$50 < We < 100$	-	$100 < We < 350$	$We > 350$
Girin [26]	-	$8 < We < 32$	$32 < We < 60$	-	-	-
Giffen, Edmund [27]	$12 < We < 16$	$16 < We < 45$	$45 < We < 100$		$100 < We < 1000$	$We > 1000$
Faeth *et al.* [12, 14, 15]	$We < 13$	$13 < We < 35$	$35 < We < 80$		$We > 80$	-
Chou, Faeth [16]	-	$13 < We < 25$	-	-	-	-
Dai, Faeth [17]	-	-	$18 < We < 40$	$40 < We < 80$	-	-
Theofanous *et al.* [21]	-	$26 < We < 44$		-	$We > 1000$	-
Krzeczkowski [11]	$We < 10$	$10 < We < 18$	$18 < We < 30$	$30 < We < 63$	$We > 63$	-

pared to the other mechanisms listed in Table 2.1. Therefore, many authors ignore this regime and take the bag breakup as the first droplet breakup mode.

Bag breakup

Based on the experimental observations by Chou and Faeth [16], the bag breakup process can be divided into four stages as shown in Figure 2.4: 1) deformation stage, during which the droplet deforms from its initial spherical shape into a liquid disk, ii) bag growth stage, during which the center of the liquid disk deforms into a thin membrane-like bag and continues to grow, iii) bag rupture stage, where the bag breaks into a liquid torus ring and many micro-size droplets, and finally iv) torus breakup stage, where the torus ring breaks into a few child droplets.

The physical mechanisms of bag breakup are very complex and no experimental investigations have been capable of measuring the local droplet and ambient flow fields that lead to the formation and disintegration of the bag structure [24]. However, it is generally accepted that the thin hollow bag forms at the stagnation point of the flattened droplet and continues to be blown downstream because of the pressure difference between the inside and outside of the bag.

The mechanisms that lead to bag rupture is not well understood. Liu and Reitz [18] suggested that the thin bag ruptures because of gradually enlarging small holes appearing on the bag sheet, producing micro-size child droplets. The formation of original holes is caused by disturbances in the air stream or presence of particles in the liquid bag that serve as inception sites. Jalaal and Mehravaran [28] studied the fragmentation of falling liquid droplets in a quiescent media using DNS, their results also suggest that the

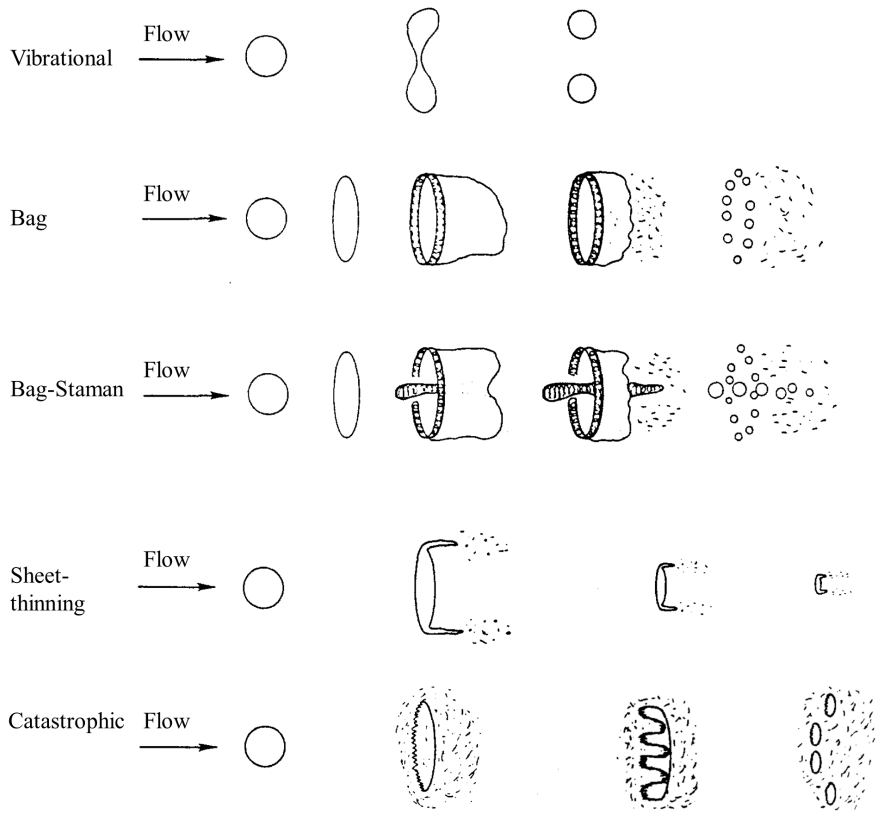

Figure 2.4: Schematic of breakup processes for various droplet breakup regimes [10].

thin bag ruptures due to small holes forming on the bag sheet. In addition, their results demonstrate that the remaining liquid torus ring will break rapidly into child droplets and ligaments due to Rayleigh instabilities.

Sheet-thining breakup

As the ambient velocity increases further, droplet breakup occurs at the droplet equator. A mechanism proposed by Ranger and Nicolls [29] involves a viscous boundary layer developed inside the droplet. This boundary layer is assumed to become unstable at

the droplet periphery, resulting in droplets being stripped away at the equator. This mechanism is generally referred to as "boundary-layer stripping" or "shear" mechanism. However, as later pointed out by Liu and Reitz [18], this mechanism does not necessarily represent the right physics due to the following reasons:

- The mechanism assumes that the dominant forces are viscous shear forces, and thus the breakup process should scale with the Reynolds number. However, experimental investigations have shown that the droplet breakup regimes scale with We number instead [18],
- The mechanism ignores the droplet flattening that has been observed experimentally during the breakup process [18].

An alternative theory proposed by Liu and Reitz [18], termed as the "sheet-thinning" mechanism, suggests that the breakup actually occurs at the flattening sheets at the edge of the droplet instead of the droplet equator. This sheet forms because the periphery of the deformed droplet is deflected in the ambient flow direction. Following the formation, this thin sheet breaks into small ligaments and then individual droplets. In addition to their experimental investigations, a number of recent numerical simulations support this mechanism as reviewed by Guildenbecher and Lopez-Rivera [24].

Multi-model breakup

Multi-mode breakup happens between the bag and sheet-thinning regimes, and thus resembles a combination of these two regimes. At We number close to the bag breakup, the droplet center core is blown downstream (called "stamen" or "plume") along with the

formation of a thin hollow bag, as illustrated in Figure 2.4. The bag ruptures first, then disintegration of the rim and stamen-structure follows. This sub-mode of multi-mode regime is terms as "bag-stamen" by Pilch and Erdman [10] and "bag/plume" by Faeth *et al*. [12, 14–16, 30]. At We close to the sheet-thinning regime, the so-called "plume/sheet-thinning" happens where no bag is formed. Rather, child droplets are stripped continuously from the liquid plume in a manner similar to the sheet-thinning breakup.

Catastrophic breakup

As We number continues to increase, the dynamic pressure on the droplet surface becomes larger, causing unstable waves to grow on the droplet leading surface. Liu and Reitz [31] suggested that the unstable waves may be described as either RT or KH instabilities. RT waves form when a density discontinuity is accelerated toward the lighter end, which eventually penetrates the droplet creating several child droplets as shown in Figure 2.4. KH instabilities occur at the droplet periphery where the relative velocity is the largest. Wavelengths of KH instabilities are much shorter compared to those of RT, and these waves are stripped from the surface to produce micro-size droplets.

2.3 Structure of multi-hole engine sprays

A schematic of the plume structure of a typical multi-hole spray is given in Figure 2.5. Moving from upstream to downstream, the spray plume can be divided into three regions:

1. **Atomization region:** Immediately after exiting the nozzle hole, the liquid jet starts to undergo atomization (or primary breakup) and forms large ligaments

and droplets. As discussed in Section 2.1, an intact liquid core may exist in this region, as suggested by the electrical conductivity measurements performed by Hiroyasu [32]. However, as summarized by Baumgarten [8], more recent optical measurements in combination with a transparent nozzle in real size geometry prove that the disintegration of high-pressure diesel sprays begins inside the nozzle hole, and thus the "intact liquid core" does not exist. For modern DISI multi-hole injection systems, the injection pressure can be as high as 30 MPa, which results in highly turbulent internal flows. Volatile components of gasoline fuel can also experience in-nozzle phase-change phenomena like flash-boiling and cavitation. Therefore, in DISI sprays this region may only consist of liquid ligaments and droplets.

2. **Dense spray region:** breakup of droplets and ligaments occurs through various mechanisms described in Section 2.2. In this region, the liquid has a lower volume fraction and droplet-to-droplet interactions such as collision, coalescence, and droplet wake can happen [33].

3. **Dilute spray region:** Droplets are well formed and have a strong interaction with the ambient flow. The breakup and evaporation of these droplets are greatly determined by the ambient conditions such as gas-phase temperature and density. Small droplets may even reach a dynamic equilibrium with their surroundings (i.e., droplets move with the ambient flow) due to their low inertia.

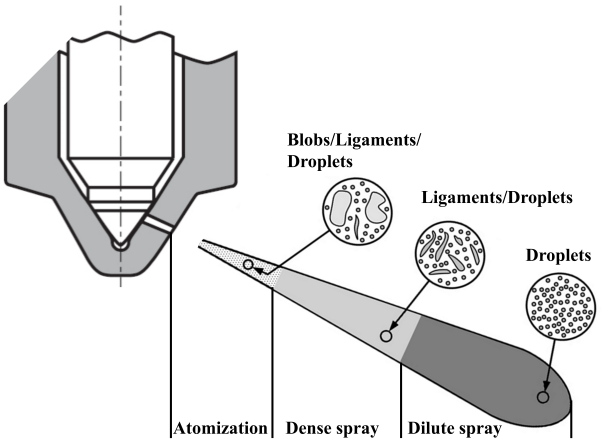

Figure 2.5: Schematic of typical spray structures from a VCO multi-hole injector [34].

2.4 Droplet dispersion in turbulent flows

Turbulent dispersion implies that a portion of the turbulent energy contributes to the dispersing of fuel droplets. As reviewed by Crowe *et al.* [35], small droplets tend to follow the gas flows due to their small inertia. Large droplets, on the other hand, will penetrate through turbulent eddies. A timescale ratio is used to assess the different behaviors (i.e., Stokes number)

$$\mathrm{St} = \frac{\tau_m}{\tau_F} = \frac{\rho_l d_d^2 U_{\mathrm{Rel}}}{18\mu_l \Delta}, \tag{2.5}$$

where $\tau_m = \rho_l d_d^2/18\mu_l$ is the aerodynamic response time, and $\tau_F = \Delta/U_{\mathrm{Rel}}$ is a characteristic time scale associated with the large-scale structure. A schematic of the effects of Stokes number on droplet dispersion is given in Figure 2.6. Droplets with $\mathrm{St} \ll 1$ maintain near velocity equilibrium with the ambient flow, whereas droplets with $\mathrm{St} \gg 1$ travel through the flow structures because the ambient flow does not have sufficient time to influence the droplets motion. Droplets with $\mathrm{St} \sim 1$ may be "centrifuged" by nearby

turbulent eddy.

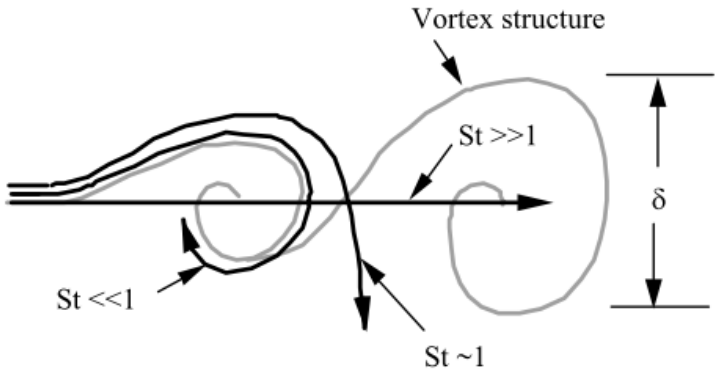

Figure 2.6: Schematic of the effects of Stokes number on droplet dispersion in large-scale turbulent structures [35].

2.5 Energy dissipation in turbulent flows

Energy dissipation can be explained by the Richardson's view of turbulent flows:

> *Big whorls have little whorls,*
>
> *Which feed on their velocity;*
>
> *And little whorls have lessor whorls,*
>
> *And so on to viscosity (in the molecular sense)*

Simply put, energy is transferred from large eddies to small eddies via a cascade process, then these small eddies transfer energy to yet smaller eddies in a similar fashion. This process continues until the molecular viscosity is effective in dissipating the kinetic energy. This notion is important because it puts the energy dissipation at the end of the

energy cascade process. The whole process can be explained in detail by Figure 2.7, which sketches the energy cascade process in turbulent flows at very high Reynolds number.

Three ranges can be found in Figure 2.7, namely: energy containing range, which as the name implies, contains the bulk of energy; inertial subrange, in which the turbulent motions are determined by the inertial effects; and dissipation range, where the molecular viscosity is responsible for essentially all energy dissipation. Various length scales are also sketched including L_{EI} and L_{DI}, which are boundaries among the aforementioned three ranges. In addition, two other length scales are defined: the Kolmogorov length scale, η, which is the smallest length scale in turbulent flows; and the integral length scale, l_0, which is the length scale of the largest eddies.

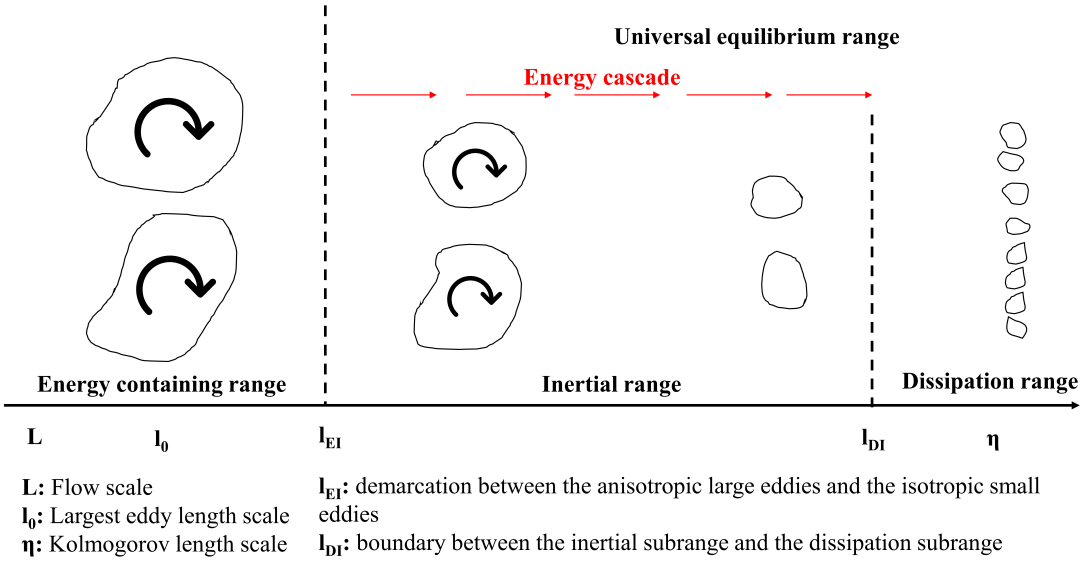

Figure 2.7: Schematic of energy cascade at very high Reynolds numbers, sketched as blobs representing turbulent eddies (i.e., vortices) (sketched based on [36]).

The energy cascade process can also be sketched on the energy spectrum, where the

energy density is plotted as a function of wavenumber for very-high Reynolds-number turbulent flow. The energy containing range is clearly illustrated in Figure 2.8. For a stationary system, we can argue that [36]

$$\frac{dk}{dt} \approx P - \Gamma_{EI}, \tag{2.6}$$

$$0 \approx \Gamma_{EI} - \Gamma_{DI}, \tag{2.7}$$

$$0 \approx \Gamma_{DI} - \varepsilon, \tag{2.8}$$

where P is the production rate in the energy containing range, Γ_{EI} and Γ_{DI} are the spectral energy transfer rates from energy containing range to the inertial range, and from the inertial range to the dissipative range, respectively.

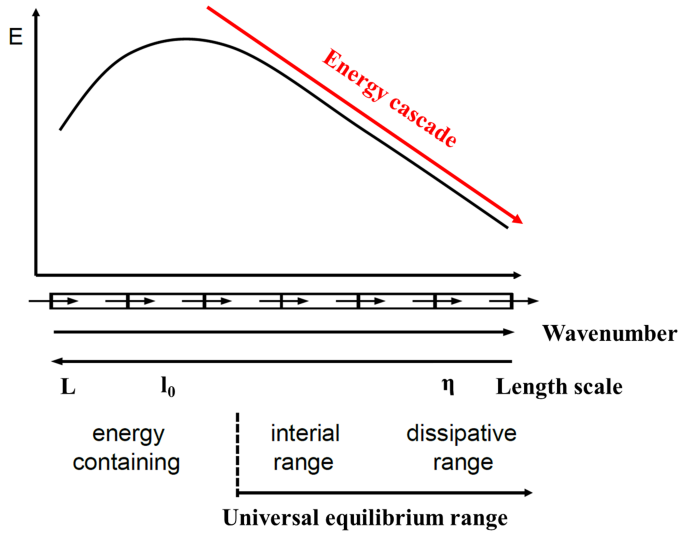

Figure 2.8: Schematic of energy cascade at very high Reynolds numbers, sketched on the energy spectrum (sketched based on [36]).

This implies that in turbulent flows at very high Reynolds number, the rate of energy transfer from the energy containing range to the inertial range, Γ_{EI}; equals to the rate of

energy transfer from the inertial range to the energy dissipation range, Γ_{DI}, and hence the dissipation rate, ε.

3 LITERATURE REVIEW

3.1 Breakup modeling of engine sprays

Since the pioneering work of Amsden and O'Rourke [37], the LE approach has been a well-established method for spray simulations in engine applications. In this approach, dispersed liquid droplets are represented as stochastic point processes in a continuous Eulerian frame and the liquid-gas interactions are accounted for as source terms in the gas-phase governing equations. Other representations of liquid-phase such as Eulerian (e.g., volume of fluid, VOF) or Eulerian-Lagrangian (i.e., Eulerian liquid-core and Lagrangian droplets) are reported in the literature and encouraging results were obtained [38, 39]. However, the computational requirement of such approaches is substantial so that the engine applications are still under development. Therefore, the literature review herein is focused on the LE approach only.

Atomization

Atomization, or primary breakup, provides initial/boundary conditions for the subsequent mixture formation process, and for this reason, it is essential to have a physical representation of this process in spray simulations [8]. However, modeling atomization represents a particularly difficult challenge since many complications such as turbulent internal flow, in-nozzle phase change, and nozzle geometries contribute to the breakup process. A reasonable approximation is to inject a "parcel" or "blob" of liquid fuel with characteristic size equals to the nozzle orifice diameter [40]. Each parcel can contain several to hundreds of liquid droplets with the same properties such as diameter, temper-

ature, and compositions. The justification of this approximation is that atomization of the liquid jet and droplet breakup near the nozzle exit are indistinguishable processes, as discussed in Section 2.3. As depicted in Figure 3.1, liquid parcels resembling the dense spray region or possibly “liquid core” are predicted to exist in the near-nozzle region. These liquid parcels then experience atomization and secondary breakup described by a breakup model or a combination of models.

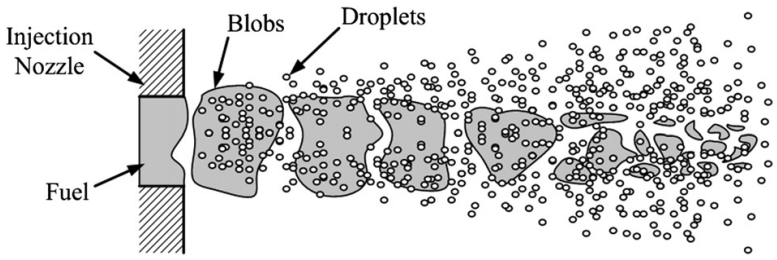

Figure 3.1: Schematic of the "blob" method.

A modification of the “blob” method is to assign droplet sizes at nozzle exit based on a probability distribution function (PDF). Experimental measurements of the droplet size distributions are hardly feasible at the nozzle exit. Thus, the droplet size PDF must be guessed and tuned to match spray characteristics further downstream of the injector exit. An example of such modification is given by Levy *et al.* [41], in which the parcel diameters are sampled from a χ^2-law in order to get a good agreement with experiments.

Some studies were focused on the atomization caused by internal turbulence or cavitation. Huh and Gosman [42] proposed a phenomenological model for turbulence-induced atomization for diesel sprays. The model assumes that the internal turbulence produces the initial surface perturbations. Those perturbation waves will then amplify according to the KH instability theory until new droplets are formed. Arcoumanis *et*

al. [43] developed a liquid core atomization model considering in-nozzle turbulence, cavitation, and aerodynamic drag. Child droplets are assumed to have a velocity equal to the liquid-core velocity, and their sizes are randomly selected from a calculated PDF depending on which mechanism led to the atomization. Baumgarten *et al*. [44] developed a model for cavitation and turbulence induced atomization, which also has the capability to map the asymmetric nozzle flow on droplet breakup. However, a multi-zone simulation of the internal flows is needed as input for the secondary breakup.

Secondary breakup

The "TAB" model family

One of the first and most widely used breakup models for engine spray is the Taylor analogy breakup (TAB) model proposed by O'Rourke and Amsden [37]. The model is based on an analogy between an oscillating and distorting droplet and a spring-mass system. The restoring force of the spring is analogous to the surface tension force, and the external force on the mass is analogous to the disruptive aerodynamic drag force. They also added the damping force due to liquid viscosity. Many studies have been done in which the TAB model was employed to describe the droplet breakup [45–48]. However, as summarized in Refs. [3, 24], the TAB model has a number of shortcomings:

1. The breakup is assumed to occur instantaneously while experimental studies have shown that the breakup occurs over a finite time,

2. In applications to diesel sprays, the droplet sizes are typically over-predicted at low pressure and under-predicted at high pressures,

3. The predicted frontal area of the distorted droplet is not accurate, which may lead to the incorrect prediction of droplet trajectory,

4. The breakup criteria is somewhat arbitrary,

5. The model only keeps tracking of one oscillation mode, while in reality, more than one mode exists.

The enhanced-TAB (ETAB) model proposed by Tanner [49] utilizes the oscillation dynamics and breakup criteria of the original TAB model but treats the breakup process differently. The rate of formation of child droplet is assumed to be proportional to the number of child droplets, with the proportionality coefficient being a function of We number. The model was shown to perform better than the TAB model for a diesel spray.

Another alternative to the TAB model is the droplet deformation and breakup (DDB) model proposed by Ibrahim *et al*. [50]. In this model, dynamics of the mass center of the half-droplet are tracked through a non-linear differential equation derived based on the energy balance between the internal energy of the half-droplet and the work done by pressure and viscous forces. However, a study performed by Park *et al*. [51] has shown that the DDB model predicts instantaneous breakup when We number is less than 19, which limits its application to engine sprays.

Other variations of the TAB model were reported in the literature. Examples include the modified TAB (MTAB) model by Senda *et al*. [52], the improved TAB (ITAB) model by Park *et al*. [51], and the cascade atomization and breakup (CAB) model by Tanner [53]. Due to the limited pages allowed in this dissertation, discussions of these models will not be provided herein. Note that each model in the "TAB" family has its

own advantages and limitations and some of them are still being used in industrial spray simulations.

The "stability analysis" model family

The Wave model, developed by Reitz and Diwakar [54] and further improved by Reitz [40], is based on a linear stability analysis of a cylindrical liquid surface subjected to perturbations. The outcome is a dispersion equation that relates the wavelength of the most unstable surface wave and its growth rate. It is assumed that a new parcel containing child droplets will be created once the mass of liquid being stripped exceeds a certain criterion. The fuel vapor distribution predicted by this model matches the experiments near the nozzle exit. However, since in real world the breakup times are influenced by surface disturbance levels, internal turbulent flows, and nozzle geometry, the breakup time constant in the Wave model is considered to be adjustable over a broad range.

Su *et al*. [55] combined the Wave model with RT instability theory for spray droplets and proposed the well-known KH-RT model. The new model was found to predict better droplet size distributions than the Wave model for a high-pressure spray. Ricart *et al*. [56] improved the KH-RT model by introducing the concept of RT breakup length. In the model, the RT sub-model is deactivated until the droplets pass beyond a pre-estimated breakup length. The modified KH-RT model was shown to give more realistic liquid- and vapor-phase penetrations over a wide range of engine operating conditions. Beale and Reitz [57] later postulated that droplets outside of the liquid-core should be affected by the RT instabilities as well even though they might lie within the breakup length. They also modified the RT sub-model so that a Rosin-Rammler distribution will be applied to

newly created child droplets. The modifications were found to give satisfactory results and to significantly improve the temperature dependency of the liquid penetration of diesel sprays.

Another known breakup model developed based on stability analysis is the linearized instability sheet atomization (LISA) model proposed by Schmidt *et al*. [48]. The model was specifically tailored for hollow-cone sprays from pressure-swirl injectors. The model is divided into three stages: 1) film formation, 2) sheet breakup, and 3) primary breakup. Each stage is treated separately and a secondary breakup mode like the TAB model will take over the breakup simulations once stage three is complete. The predicted penetration and droplet size were compared favorably to experimental measurements.

Recently, Tsang and Rutland [6] developed a stochastic KH-RT model aiming to reduce the sensitivity of optimal model parameters on ambient conditions. The stochastic model determines the time and length scales of the KH and RT unstable waves in a stochastic and dynamic manner. The model was found to give reasonable predictions of the liquid penetrations over a wide range of operating conditions without tuning the model parameters.

Hybrid model family

Aiming to develop a breakup model for modeling a variety of fuel sprays in IC engines, Chryssakis and Assanis [2] proposed a unified model composed of three main parts, namely, primary breakup model, droplet deformation and aerodynamic drag, and secondary droplet breakup. The primary breakup is modeled based on the turbulence-induced atomization model by Huh *et al*. [42] or LISA model by Schmidt *et al*. [48],

depending on the injector geometries. The secondary breakup is divided into four sub-models according to the breakup regimes reviewed in Section 2.2. Each regime is treated differently with a corresponding phenomenological model. The model was validated against several non-evaporating gasoline and diesel sprays, covering a wide range of typical engine applications from very low to very high We numbers. Spray characteristics like penetration rate, SMD, and spray envelops were examined and the overall agreement is good with small discrepancies. One interesting finding from their study is that the bag and multi-mode breakup are important for gasoline sprays, whereas the sheet-thinning (termed as the shear breakup in their publication) and catastrophic mechanisms dominate diesel spray breakup process.

Other hybrid models were reported in the literature, in which two or more atomization/breakup models were combined targeting various types of engine sprays. Examples of those include the Hug-Gosman/KH-RT model by Li *et al*. [58], the LISA-TAB model by Schmidt *et al*. [48], and the flashing KH-RT model by Shen *et al*. [59].

Large-eddy gasoline spray simulations

Most of the reported work on LES of gasoline sprays were achieved by combining RANS spray models with an LES turbulence model. Arai *et al* [45] performed an LES study of spray injection into turbulent duct flows that have properties easy to understand as a basis of engine simulations. The fuel (dry solvent) was injected from a slit injector with an initial velocity close to GDI injectors ($\approx$ 150 m/s). In their work, the primary breakup was not modeled. Rather, droplet diameters at the nozzle exit were assigned based on a droplet distribution function to mimic the primary breakup. The TAB model was used

to describe the secondary breakup. Results showed that LES can resolve the inhomogeneous small eddies and flow structures induced by spray itself. The cross-sectional view of parcels also showed that droplets tend to avoid regions of high vorticity.

Nishad *et al*. [46,47] proposed a comprehensive model for simulating GDI processes. The model includes a LISA-based sub-model for the primary breakup and the TAB model for the secondary breakup. It also has a droplet collision model that is independent of mesh resolution. The spray sub-models were coupled to the Smagorinsky LES turbulence model. The complete model was implemented in KIVA-4 CFD code and validated against both non-evaporating and evaporating GDI sprays. The results showed good agreement with experiments in terms of penetration rates and droplet size distributions.

One issue of using RANS spray models with LES turbulence model is that the RANS spray source term in the transport equation of sub-grid kinetic energy, k_{sgs}, is modeled only as a sink, which usually leads to severe over-prediction of penetration rates. However, in the context of LES, the spray can be either a source or a sink [4]. In order to address this issue, Bharadwaj *et al*. [60] developed a model of the spray source term in the k_{sgs} transport equation. The model can act both as a source or a sink for k_{sgs}, depending upon the aerodynamic drag and sub-grid velocity vectors. The model was implemented in the KIVA-3V LES code and tested against diesel spray experiments in a constant volume chamber. Results showed that the new spray source term model predicts liquid-phase penetration that matches the experiments.

Van Dam and Rutland [61] further explored the possibility of applying this improved LES spray simulation framework to DISI gasoline sprays. The LES models were validated against DISI sprays in a constant volume chamber over a wide range of ambient

conditions covering both homogeneous and stratified charge engine operations. Spray penetration rates (both liquid and vapor phases), as well as spray images, were examined against experimental measurements. A functional relationship between KH-RT model parameters and liquid-gas density ratio was found after a careful calibration of the KH-RT model. This functional relationship, though struggles to accurately capture both liquid- and vapor-phase penetrations, predict good vapor contours compared to the Schlieren measurements. An interesting finding from their work is that detailed chamber geometry, especially near the nozzle exit, is of great importance to accurate LES predictions. Therefore, including the nozzle geometry into CFD mesh will properly guide the flow near the nozzle exit and accurately predict the recirculation zone inside the multi-plume spray structure.

The lack of understanding of atomization near nozzle exit and in particular the impact of nozzle geometry and internal flow often requires modelers to assume a droplet size distribution as the initial condition for Lagrangian spray simulations (for example, Rosin-Rammler distribution or χ^2-distribution). The assumed initial droplet size distribution often has to be tuned with experimental results. In order to address this issue, various studies that use coupled high fidelity internal flow solver and Lagrangian spray simulation have been done. Bode *et al*. [62] proposed a new approach which combines high-fidelity primary breakup simulation in the vicinity of the nozzle exit and Lagrangian spray simulation. The so-called combined primary breakup and Lagrange spray (CPBLS) approach divides the simulation into three parts: 1) the internal flow is solved by a statistically stationary LES in which the quasi-steady but fluctuating velocity profile at the nozzle exit is recorded, 2) the atomization is computed by DNS of the

liquid jet into a rectangular domain, and 3) a Lagrangian spray simulation is conducted with initial conditions taking from the DNS computation. The secondary breakup is described by the KH-RT model. The CPBLS approach was implemented into an in-house CFD code called CIAO wherein the SGS stresses and scalar fluxes are closed with dynamic Smagorinsky-type models. The results of CPBLS simulations for a 6-hole GDI spray were compared to common Lagrangian spray simulation and experimental data. As expected, predicted penetration rates and normalized droplet size distributions from CPBLS are better than those from Lagrangian spray simulation and in very good agreement with experiments.

Bode *et al*. [63] further incorporated an internal nozzle cavitation model and a hydraulic flip model (which accounts for gas entrainment from outside the nozzle orifice) into the CPBLS approach. The improved model was applied to two different 3-hole GDI sprays and results were compared against X-ray and phase Doppler particle analyzer (PDPA) experiments. Results showed that simulations with the cavitation model predict better penetration rates, droplet velocities, and size distributions, while simulations with the hydraulic flip model show better far-field droplet size distributions.

3.2 SGS dispersion modeling in engine flows

In the LE approach, the dispersing effects of turbulent flow structures on fuel droplets are expressed via aerodynamic drag forces exerted by ambient surroundings, which ultimately traces back to the instantaneous carrier fluid velocity “seen” or “felt” by droplets themselves. The fluid velocity directly influences the relative velocity between the carrier phase and liquid droplets, and thus the subsequent droplet trajectories, breakup, and

evaporation. In LES applications to engines, the most popular approach to consider this effect is to divide the instantaneous gas velocity at the droplet location into two parts: 1) a deterministic part which can be readily obtained from the filtered velocity, and 2) an SGS part which can be related to the unresolved field. The SGS velocity cannot be evaluated directly, and therefore requires a droplet dispersion model.

Currently, the most common approach to estimate the SGS velocity is the stochastic approach developed by Gosman and Loannides [64], in which the turbulence is assumed to be isotropic and to possess a Gaussian probability distribution. The SGS velocity is then sampled from a Gaussian distribution with zero mean and a variance related to the SGS turbulent kinetic energy. The main issue with extending this approach to LES comes from the fact that it builds on statistical averages, whereas the LES flow field is deterministic and instantaneous. A typical history of the SGS velocity estimated using this approach is shown in Figure 3.2a. As the figure shows, a sampled velocity remains fixed until the droplet is assumed to pass a turbulent eddy. The next sample is independent of the previous one, and therefore produces an SGS velocity history that is discontinuous in time. This model is therefore also termed as the "discrete random walk (DRW)" model.

Some work on LES has focused on the SGS dispersion modeling. One popular approach is to apply the approximate deconvolution method (ADM) on the resolved fluid field, resulting in a deterministic, instantaneous velocity field that can be used to evolve the spray droplets [65, 66]. It has been shown that results obtained through ADM are in good agreement with those obtained by DNS in some cases. However, in practice, ADM can only retrieve the SGS motions of the order of LES cut-off width, whereas the

effects of smaller scales are neglected. Recently, Pozorski and Apte [67] argued that the SGS flow field can be assumed to be locally isotropic and proposed a stochastic differential equation (SDE) to reconstruct the SGS fluid velocity along particle trajectories. Figure 3.2b shows an SGS velocity history determined from this model. As can be seen, the "steps" of the DRW model are eliminated and therefore the model suits LES to some extent. The SDE model by Pozorski and Apte is able to simulate the randomizing effect of SGS dispersion for large-inertia particles. However, for small-inertia particles that tend to follow the flow scales filtered out by LES, the model fails to predict the preferential concentration since it is diffusive in nature.

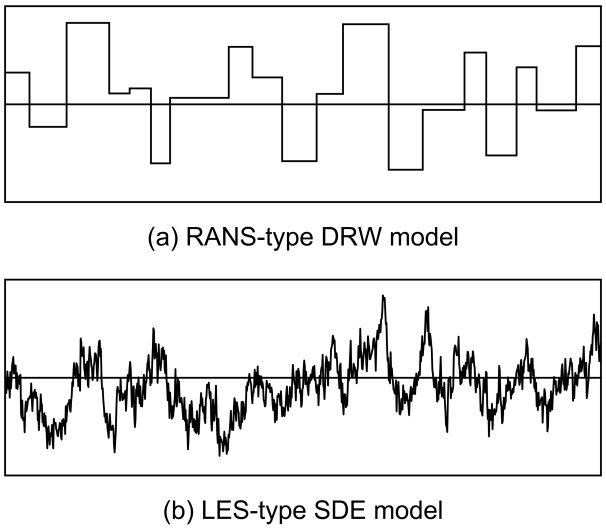

Figure 3.2: Schematic of the SGS dispersion velocity predicted by RANS-type DRW model and LES-type SDE model.

Recently, Tsang *et al.* [68] studied the effects of SGS dispersion on a diesel spray with a hybrid model. In their model, the instantaneous gas velocity is divided into three parts: 1) the filtered gas velocity directly available from the resolved field, 2) a deterministic

SGS velocity part obtained using the ADM method, and 3) a stochastic SGS velocity part which is assumed to possess a Gaussian distribution. The model was successfully validated against high-fidelity VOF simulations [68] of a low injection velocity spray.

3.3 SGS energy dissipation rate in engine flows

Depending on which turbulence model is used in the LES simulation, the term "SGS energy dissipation rate" may have different meanings. For zero equation LES turbulence models like the Smagorinsky model, the "SGS energy dissipation rate" might refer to the energy flux from the resolved field to the SGS fields. This can be illustrated in Figure 3.3b, where the residual motions (colored by gray shade) have a clear boundary with the resolved field. The boundary corresponds to the LES filer size. For one equation LES turbulence model like the dynamic structure non-viscosity model by Pomraning and Rutland [69], the "SGS energy dissipation rate" refers to the energy removal from the SGS kinetic energy (illustrated as gray shade in Figure 3.3a). The boundary between "SGS energy dissipation" and the others becomes indistinct because the length scale associated with the SGS kinetic energy can only be estimated. Figure 3.3 also demonstrates one advantage of using one-equation turbulence model in engine flows: it allows coarser grids to be used as commonly found in Engine CFD, due to the better modeling of SGS shear stress tensor provided by a transport equation for SGS kinetic energy [4]. For the remainder of this dissertation, the term "SGS energy dissipation rate" refers to the energy removal from SGS kinetic energy, k_{sgs}.

Modeling of the energy dissipation rate in LES of engine flows is very scarce. A classic

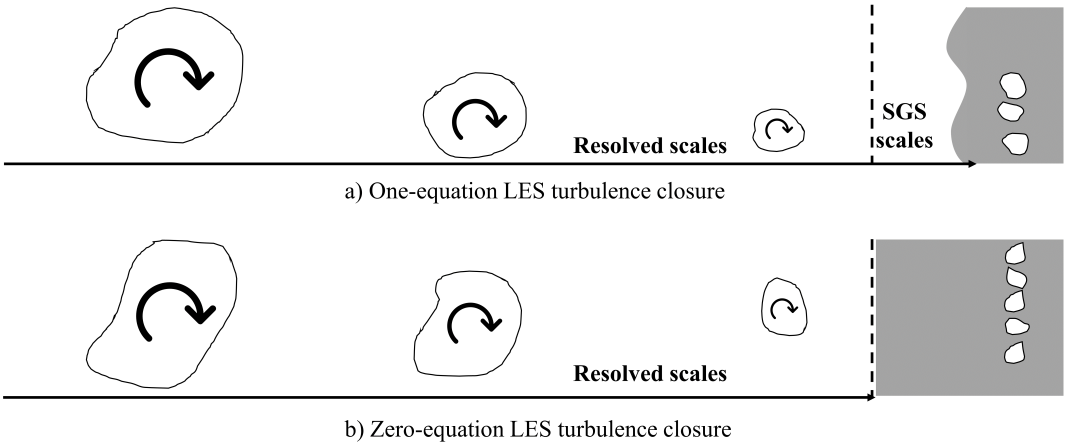

Figure 3.3: Schematic of SGS energy dissipation modeling in LES..

model is written as [70]

$$\varepsilon_{\text{sgs}} = C\rho\frac{k_{\text{sgs}}^{3/2}}{\Delta}, \tag{3.1}$$

where C, Δ are a model parameter and the LES filter width, respectively. The model was derived based on dimensional analysis, an approach commonly used in turbulence modeling. As Equation 3.1 demonstrates, this model guarantees positive dissipation (i.e., a sink) thus better stability. However, the value of C requires *a priori* knowledge of the target flow and often needs to be tuned to provide a better matching.

Equation 3.1 also shows that the SGS energy dissipation rate scales with $k_{\text{sgs}}^{3/2}$. This power law scaling $\varepsilon_{\text{sgs}} \propto k_{\text{sgs}}^{\upsilon}$ has indeed observed in various studies [71, 72]. The scaling factor, υ, however, varies from 0.5 to 1.0 depending on the filter size and the flow conditions [72]. The *ad hoc* scaling of $\varepsilon_{\text{sgs}} \propto k_{\text{sgs}}^{1.5}$ in Equation 3.1 is therefore poorly justified. Recently, analogous Leonard-type SGS dissipation rate models have been developed [71]. *a prior* test shows that those models perform better than Equation 3.1. However, *a posteriori* test in engine sprays has yet to be conducted to further evaluate

their performance. Another alternative approach to modeling the energy dissipation rate is to add an additional transport equation for ε_{sgs}. One example is given by Pomraning and Rutland [69]. However, this brings more difficulties such as unclosed terms in the ε_{sgs}-transport equation.

4.1 Eulerian gas-phase equations

LES gas-phase equations are obtained by applying a spatial filtering to the fundamental conservation equations of mass, momentum, and energy. For a flow variable $\phi\left(\vec{x},t\right)$, the filtering process is defined as

$$\overline{\phi}\left(\vec{x},t\right)=\phi\left(\vec{x},t\right)\circledast G=\int_{\mathbb{R}^3}\phi\left(\vec{x},t\right)G\left(\vec{x}'-\vec{x}\right)\mathrm{d}\vec{x}', \tag{4.1}$$

where $\circledast$ and $\mathbb{R}^3$ denote the convolution operator and the set of real numbers. The filter convolution kernel G must satisfy the following constraint

$$\int_{\mathbb{R}^3}G\left(\vec{x}'\right)\mathrm{d}\vec{x}'=1. \tag{4.2}$$

There are many types of filter kernels G used in LES [73]. The one used in the current study, which also remains the most common one, is the "box" or "top-hat" filer written as

$$G\left(\vec{x}'\right)=\begin{cases}0 & \left\|\vec{x}'\right\|_\infty>\Delta/2\\ 1/\mathcal{V} & \left\|\vec{x}'\right\|_\infty\leq\Delta/2\end{cases}, \tag{4.3}$$

where Δ is the filter width, and $\mathcal{V}$ is the filter volume defined as Δ^3.

Conservation equations

Fuel droplets in the LE approach are represented as point processes that occupy zero volumes. Contributions from droplets to the gas-phase conservation equations are then

treated as source terms. Assuming the filtering operator commutes with temporal and spatial differentiation, the LES governing equations can be obtained [60,74]

$$\frac{\partial \overline{\rho}}{\partial t} + \frac{\partial \overline{\rho}\widetilde{u}_j}{\partial x_j} = \mathrm{S_I}, \tag{4.4}$$

$$\frac{\partial \overline{\rho}\widetilde{u}_i}{\partial t} + \frac{\partial \overline{\rho}\widetilde{u}_i\widetilde{u}_j}{\partial x_j} = -\frac{\partial \overline{P}}{\partial x_i} - \frac{\partial \overline{\Gamma}_{ij}}{\partial x_j} - \frac{\partial \overline{\rho}\tau_{ij}^{\mathrm{sgs}}}{\partial x_j} + \overline{\rho} g_i + \mathrm{S_{II,i}}, \tag{4.5}$$

$$\frac{\partial \overline{\rho}\widetilde{h}_s}{\partial t} + \frac{\partial \overline{\rho}\widetilde{u}_j\widetilde{h}_s}{\partial x_j} = -\frac{\partial \overline{\rho}\widetilde{K}}{\partial t} - \frac{\partial \overline{\rho}\widetilde{u}_j\widetilde{K}}{\partial x_j} + \frac{\partial \overline{P}}{\partial t} - \frac{\partial \overline{q}_j}{\partial x_j} - \frac{\partial h_j^{\mathrm{sgs}}}{\partial x_j} + \widetilde{Q}_{\mathrm{chem}} + \mathrm{S_{III}}, \tag{4.6}$$

$$\frac{\partial \overline{\rho}\widetilde{Y}_k}{\partial t} + \frac{\partial \overline{\rho}\widetilde{u}_j\widetilde{Y}_k}{\partial x_j} = -\frac{\partial \overline{\chi}_{j,k}}{\partial x_j} - \frac{\partial \Phi_{j,k}^{\mathrm{sgs}}}{\partial x_j} + \overline{\dot{\omega}}_k + \mathrm{S_{IV,k}}, \tag{4.7}$$

where $u, P, \Gamma_{ij}, \tau_{ij}^{\mathrm{sgs}}, g, h_s, K, q, h^{\mathrm{sgs}}, Q_{\mathrm{chem}}, Y, \overline{\chi}, \Phi^{\mathrm{sgs}}, \dot{\omega}$ are the gas-phase velocity, pressure, molecular stress tensor, SGS stress tensor, gravitational force, sensible enthalpy, resolved kinetic energy, heat transfer rate, SGS energy flux, chemical reaction heat release rate, species mass fraction, resolved species flux, SGS species flux, and chemical reaction rate, respectively. Subscripts i, j are coordinate directions and k represents fuel species k. The operator $\widetilde{\ }$ denotes a density weighted average (i.e., Favre filtering)

$$\widetilde{\phi} = \frac{\overline{\rho\phi}}{\overline{\rho}}. \tag{4.8}$$

The SGS stress tensor, τ_{ij}^{sgs}, SGS energy flux, h_j^{sgs}, and SGS species flux, $\Phi_{j,k}^{\mathrm{sgs}}$, are unclosed terms that cannot be evaluated directly from the resolved fields. In CFD applications to engines, LES is often used to indicate the turbulent closure for τ_{ij}^{sgs} only [4].

The modeled forms of the latter two are

$$h_j^{\text{sgs}} = -\frac{\mu_{\text{sgs}}}{\text{Pr}_t}\frac{\partial \widetilde{h}_s}{\partial x_j}, \tag{4.9}$$

$$\Phi_{j,k}^{\text{sgs}} = -\frac{\mu_{\text{sgs}}}{\text{Sc}_t}\frac{\partial \widetilde{Y}_k}{\partial x_j}, \tag{4.10}$$

where Pr_t, Sc_t are the turbulent Prandtl and Schmidt numbers, respectively.

The other terms in Equations 4.4 - 4.7 are closed by

$$K \equiv \frac{1}{2}\widetilde{u}_i\widetilde{u}_i, \tag{4.11}$$

$$\overline{\Gamma}_{ij} = -\mu\left[\frac{\partial \widetilde{u}_i}{\partial x_j} + \frac{\partial \widetilde{u}_j}{\partial x_i}\right] + \frac{2}{3}\mu\frac{\partial \widetilde{u}_k}{\partial x_k}\delta_{ij}, \tag{4.12}$$

$$\overline{q}_j = -\alpha\overline{\rho}\frac{\partial \widetilde{h}_s}{\partial x_j}, \tag{4.13}$$

$$\widetilde{Q}_{\text{chem}} = \int_{k=1}^{\text{NS}} -\Delta h_f^\circ \overline{\dot{\omega}}_k, \tag{4.14}$$

$$\overline{\chi}_{j,k} = -\mu\frac{\partial \widetilde{Y}_k}{\partial x_j}, \tag{4.15}$$

where $\alpha, \mu_{\text{sgs}}, \text{NS}, \Delta h_f^\circ$ are the thermal diffusivity, SGS viscosity, number of species, and enthalpy of formation, respectively.

LES turbulence model

The SGS stress tensor in Equation 4.5 is defined as

$$\tau_{ij}^{\text{sgs}} = \widetilde{u_i u_j} - \widetilde{u}_i\widetilde{u}_j. \tag{4.16}$$

The term is closed based on a mixed approach developed by Tsang *et al*. [75]. The model builds on the dynamic structure one-equation non-viscosity model developed by Pomraning and Rutland [69] and utilizes a modified Smagorinsky eddy-viscosity model. According to this approach

$$\tau_{ij}^{\text{sgs}} = 2c_{ij}k_{\text{sgs}} - 2\nu_{\text{noz}}\left(\widetilde{S}_{ij} - \frac{1}{3}\,\text{Tr}(\widetilde{S}_{ij})\right), \tag{4.17}$$

where $c_{ij}, \nu_{\text{noz}}, \widetilde{S}_{ij}$ are the SGS stress tensor coefficient, near-nozzle artificial viscosity, and the strain rate tensor obtained from the resolved fields, respectively. The operator Tr denotes the trace operator and is applied on the 2nd rank tensor. Definitions of $c_{ij}, k_{\text{sgs}}, \nu_{\text{noz}}, \widetilde{S}_{ij}$ are

$$c_{ij} = \frac{L_{ij}}{\text{Tr}(L_{ij})}, \tag{4.18}$$

$$k_{\text{sgs}} \equiv \frac{1}{2}\left(\widetilde{u_i u_i} - \widetilde{u}_i\widetilde{u}_i\right), \tag{4.19}$$

$$\nu_{\text{noz}} = \begin{cases} C_{\text{noz}}\Delta k_{\text{sgs}}^{1/2} & |\widetilde{S}_{ij}| \geq |\widetilde{S}_{ij}|_{max} \\ 0 & \text{otherwise} \end{cases}, \tag{4.20}$$

$$\widetilde{S}_{ij} = \frac{1}{2}\left(\frac{\partial \widetilde{u}_j}{\partial x_i} + \frac{\partial \widetilde{u}_i}{\partial x_j}\right). \tag{4.21}$$

The Leonard stress tensor, L_{ij}, in Equation 4.18 is defined as

$$L_{ij} = \widehat{\widetilde{u}_i\widetilde{u}_j} - \widehat{\widetilde{u}}_i\widehat{\widetilde{u}}_j, \tag{4.22}$$

where the operator $\widehat{\ }$ denotes a test-level filtering on an additional cell layer around the computational mesh. Equation 4.20 indicates that the eddy viscosity is only imposed

on a specific region where the strain rate magnitudes are larger than a given threshold, $|\widetilde{S}_{ij}|_{max}$. The SGS kinetic energy is modeled using an additional transport equation given by Bharadwaj and Rutland [76]. The modeled form of this equation is written as

$$\frac{\partial \bar{\rho} k_{\text{sgs}}}{\partial t} + \frac{\partial \bar{\rho} \widetilde{u}_j k_{\text{sgs}}}{\partial x_j} = \frac{\partial}{\partial x_j}\left(\mu_{\text{sgs}} \frac{\partial k_{\text{sgs}}}{\partial x_j}\right) + P_{\text{sgs}} - \varepsilon_{\text{sgs}} + \dot{W}^s_{\text{sgs}}, \tag{4.23}$$

where $P_{\text{sgs}}, \dot{W}^s_{\text{sgs}}$ are the SGS production and spray source rates, respectively. The SGS production term is written as

$$P_{\text{sgs}} = -\bar{\rho}\Gamma_{ij}\frac{\partial \widetilde{u}_i}{\partial x_j}, \tag{4.24}$$

and the SGS viscosity is characterized with the SGS kinetic energy and a characteristic length. Lilly [77] postulates that

$$\mu_{\text{sgs}} = C_k \rho \Delta k^{1/2}_{\text{sgs}}, \tag{4.25}$$

where C_k is a model parameter. Table 4.1 lists the values of parameters in equations described in this section. Note that those values are kept as constants throughout this work, unless specified otherwise.

Table 4.1: Summary of parameter values in equations described in Section 4.1. Note that the parameter values are kept constant throughout this study, unless specified otherwise.

Parameter	**Value**
Pr_t	1.0
Sc_t	0.7
C_{noz}	4.6
C_k	0.05

4.2 Lagrangian liquid-phase equations

The dispersed liquid-phase is described by solving the droplet distribution function (DDF), which consists of independent variables such as Lagrangian position, velocity vector, and diameter. Additional variables can be added to the DDF without violating the generality. A valid statistical description of the spray development requires a tremendous amount of spray droplets. To reduce the computational cost, liquid "parcels" are used in most CFD code. Each parcel contains several to hundreds of droplets with the same physical properties. Sub-models for the spray breakup, evaporation, and collision processes are applied to each individual parcel. The Lagrangian equations for liquid droplets are

$$\frac{\mathrm{d}x_{d,i}}{\mathrm{d}t} = v_{d,i}, \tag{4.26}$$

$$\frac{\mathrm{d}v_{d,i}}{\mathrm{d}t} = \frac{F_{d,i}}{m_d}, \tag{4.27}$$

$$\frac{\mathrm{d}T_d}{\mathrm{d}t} = \frac{1}{m_d C_{p,d}} \left(Q + \dot{m}_d L_v\right), \tag{4.28}$$

$$\frac{\mathrm{d}m_d}{\mathrm{d}t} = \dot{m}_d, \tag{4.29}$$

where $x_{d,i}$, $v_{d,i}$, T_d, and m_d are droplet position, velocity, temperature, and mass, respectively. In Equations 4.28 and 4.29, $C_{p,d}$ is the droplet specific heat, Q is the heat flux at the droplet surface, L_v is the latent heat of vaporization, and $\dot{m}_d$ is the rate of change of droplet mass. The aerodynamic drag force $F_{d,i}$ is calculated using a linear drag law [37]

$$F_{i,d} = C_d \frac{3}{4} \frac{\overline{\rho}}{\rho_l} \frac{|u_{g,i} - v_{d,i}|}{d_d} m_d \left(u_{g,i} - v_{d,i}\right), \tag{4.30}$$

where C_d, $u_{g,i}$ are the drag coefficient and the instantaneous gas-phase velocity "seen" by the liquid droplet, respectively. The drag coefficient, C_d, is calculated as follows

$$C_d = \begin{cases} \frac{24}{\mathrm{Re}}\left[1 + \frac{1}{6}\mathrm{Re}^{2/3}\right] & \mathrm{Re}_d \leq 1000 \\ 0.424 & \mathrm{Re}_d > 1000 \end{cases}, \tag{4.31}$$

where Re is the Reynolds number,

$$\mathrm{Re} = \frac{\overline{\rho}|u_{g,i} - v_{d,i}|d_d}{\mu}. \tag{4.32}$$

The heat flux at the droplet surface, Q, and the rate of change of droplet mass, $\dot{m}_d$, are calculated using the Ranz-Marshall correlation and an evaporation model based on the Sherwood number. Details of these two models are given by Tsang [78].

Spray source terms in Equations 4.4 - 4.7 and 4.23 are given by

$$S_{\mathrm{I}} = \frac{-\sum_d \dot{m}_d}{V_{\mathrm{cell}}}, \tag{4.33}$$

$$S_{\mathrm{II,i}} = \frac{-\sum_d \left(F_{i,d} + \dot{m}_d u_{d,i}\right)}{V_{\mathrm{cell}}}, \tag{4.34}$$

$$S_{\mathrm{III}} = \frac{\sum_d}{V_{\mathrm{cell}}}\left[\dot{m}_d\left(L_v + \frac{1}{2}|u_{g,i} - v_{d,i}|^2\right) - \rho_l C_{p,d}\dot{T}_d - F_{d,i}\left(v_{d,i} - u_{g,i}\right)\right], \tag{4.35}$$

$$S_{\mathrm{III,k}} = \frac{-\sum_d \dot{m}_k}{V_{\mathrm{cell}}}, \tag{4.36}$$

$$\dot{W}^s_{\mathrm{sgs}} = -\frac{\sum_d F_{d,i}}{V_{\mathrm{cell}}}\left(2\widetilde{u_i} - 3\widetilde{\widetilde{u_i}} + \widetilde{\widetilde{\widetilde{u_i}}}\right). \tag{4.37}$$

The operator $\sum_d$ indicates that the contributions from individual droplets are summed over all droplets within a specific cell, and V_{cell} is the cell volume.

4.3 The integrated atomization/breakup model

In the IAB model, atomization and breakup of liquid parcels are treated as indistinguishable processes and two integrated sub-models are used to track them. Descriptions of both models will be provided first, followed by the analysis of bag characteristics at various We numbers.

The KH-RT sub-model

The KH-RT hybrid model refers to the one developed by Su *et al*. [55] based on the work of Reitz and Diwakar [54] and Reitz [40]. The model was later improved by Ricart *et al*. [56] by introducing the RT breakup length to account for different penetration rates within and beyond a certain distance from the nozzle exit. KH instability waves are assumed to grow on the liquid-gas interface due to liquid inertia, surface tension, viscous and aerodynamic forces on liquid jets and droplets. The frequency of the fastest-growing wave, Ω_{KH}, and the corresponding wavelength, Λ_{KH}, are given by

$$\Omega_{\mathrm{KH}} = \frac{0.34 + 0.134\mathrm{We}^{1.5}}{(1 + 1.414\mathrm{Oh})(1 + 1.4\mathrm{Ta}^{0.6})}\sqrt{\frac{8\sigma}{\rho_l d_d^3}}, \tag{4.38}$$

$$\Lambda_{\mathrm{KH}} = \frac{4.51 d_d(1 + 0.535\sqrt{\mathrm{Oh}}(1 + 0.4\mathrm{Ta}^{0.7}))}{(1 + 0.272\mathrm{We}^{1.67})^{0.6}}, \tag{4.39}$$

where Ta is the Taylor number defined as $\mathrm{Ta} = \mathrm{Oh}\sqrt{\mathrm{We}}$. Child droplets are formed with diameter d_c such that $d_c = 2B_0\Lambda_{\mathrm{KH}}$ with the constant $B_0 = 0.61$. The rate of change of parent droplet diameter is then inversely proportional to the KH time constant, τ_{KH}

$$\frac{\mathrm{d}d_d}{\mathrm{d}t} = \frac{d_d - d_c}{\tau_{\mathrm{KH}}}, \tag{4.40}$$

where the KH time constant is defined as

$$\tau_{\mathrm{KH}} = \frac{1.863 B_1 d_d}{\Lambda_{\mathrm{KH}} \Omega_{\mathrm{KH}}}. \tag{4.41}$$

RT instability waves are due to droplet acceleration or deceleration. The fastest-growing frequency, Ω_{RT}, and the corresponding wavelength, Λ_{RT}, are given by

$$\Omega_{\mathrm{RT}} = \sqrt{\frac{2}{3\sqrt{3\sigma}} \frac{[-a(\rho_l - \rho)]^{1.5}}{\rho_l + \rho_g}}, \tag{4.42}$$

$$\Lambda_{\mathrm{RT}} = 2\pi C_{\mathrm{RT}} \sqrt{\frac{3\sigma}{-a(\rho_l - \rho)}}, \tag{4.43}$$

where a is the acceleration in the direction of travel, C_{RT} is a model parameter typically equals to 0.1. The growth time of RT instability wave is tracked if the wavelength, Λ_{RT}, is smaller than the droplet diameter, d_d. The droplet is assumed to break if the wave growth time exceeds the RT breakup time, $\tau_{\mathrm{RT}} = C_\tau \Omega_{\mathrm{RT}}$, where C_τ is a model parameter which typically equals to one. The diameter of child droplets is assumed to be Λ_{RT}.

The KH-RT hybrid model builds on the idea that only the KH breakup is activated if the distance between liquid parcels and the nozzle exit is within a pre-calculated RT breakup length, L_B. Beyond that length, both KH and RT instability waves compete to break the droplet. The following formula is commonly used in previous studies to estimate this length as proposed by Ricart *et al.* [56]

$$L_B = 9.12 C_b d_{\mathrm{noz}} \sqrt{\frac{\rho_l}{\rho}}. \tag{4.44}$$

In this study, the RT breakup length is calculated using the following formula

$$L_B = \frac{\sqrt{C_a} d_{\text{noz}}}{C_\beta \sin(\theta)} \sqrt{\frac{\rho_l}{\rho}}, \tag{4.45}$$

where C_a is the orifice area contraction coefficient, d_{noz} is the nozzle diameter, C_β is a model parameter, and θ is the plume direction (i.e., spray-axis angle).

Equation 4.45 is proposed based on the mixing-limited vaporization model of Siebers [79], where L_B projected to the injector centerline is proportional to the characteristic liquid length defined by Siebers [79]. Although the model was developed for single-hole diesel sprays, it can be applied to multi-hole DISI sprays with some success [80]. In Equation 4.45, the product of the square root of area contraction coefficient and the nozzle diameter represents the effective orifice diameter. The impact of plume interactions is considered by taking the sine of plume direction, θ.

The bag breakup sub-model

A phenomenological model for the bag and bag-stamen breakup is developed based on the experimental observations of Chou and Faeth [16]. In this model, the breakup process is divided into three stages as illustrated in Figure 4.1: i) droplet deformation and bag growth stage, during which the droplet deforms from its initial spherical shape into a liquid disk and forms a continuously growing thick membrane-like bag, ii)bag rupture stage, where the bag bursts into a liquid torus ring and many micros-size droplets, and finally iii) torus breakup stage, where the torus ring breaks into a few child droplets. Two characteristic sizes are expected, one corresponds to the bag rupture and the other to the torus breakup. This may lead to bi-modal droplet size distributions [24, 81].

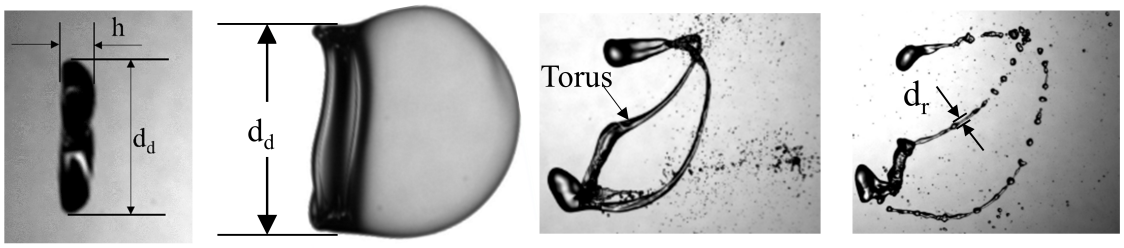

i) droplet deformation and bag growth ii) bag rupture iii) torus breakup

Figure 4.1: Schematic of the bag breakup process [20]. Note that the expected "bi-modal" droplet distribution from the bag rupture and torus breakup.

Stage i: bag growth model

Assuming the liquid droplet is subjected to an inviscid, incompressible ambient flow, Villermaux and Bossa [82] gave the following equation describing the droplet deformation and bag growth

$$\frac{1}{8}d_d\ddot{d}_d = \frac{1}{\rho_l}\{P_{\text{stag}} - P_{\kappa_{max}}\}, \tag{4.46}$$

where P_{stag} and $P_{\kappa_{max}}$ are the liquid pressures at the front stagnation point and liquid-gas border where the curvature is the maximum. Operator $\ddot{}$ denotes the double derivative with respect to time. The stagnation pressure is given by Ref. [82]

$$P_{\text{stag}} = \rho\frac{U_{\text{Rel}}^2}{2}. \tag{4.47}$$

Liquid pressure $P_{\kappa_{max}}$ is equal to the gas-phase pressure at the droplet surface plus a jump proportional to the droplet surface curvature, κ, and to the droplet surface tension, σ. In this work, we assume

$$P_{\kappa_{max}} = P_{\text{stag}} - C_1\frac{\rho\lambda^2 d_d^2}{32} + C_2\frac{2\sigma}{h}, \tag{4.48}$$

where C_1 and C_2 are two constants accounting for the variations of stretching rate and surface curvature with time, λ, h are the droplet stretching rate and liquid disk thickness, respectively. According to Villermaux and Bossa [82], λ and h can be estimated using

$$\lambda = \frac{4U_g}{d_0}, \tag{4.49}$$

$$h = \frac{2d_0^3}{3d_d^2}, \tag{4.50}$$

where d_0 is the initial droplet diameter. Assuming $C_1 = C_2 = C_{\text{bag}}^2/4$ and substituting Equations 4.47 - 4.50 into Equation 4.46 gives

$$\frac{\ddot{d}_d}{d_d} = \frac{C_{\text{bag}}^2}{T^{*2}}\left(1 - \frac{6}{\text{We}_0}\right), \tag{4.51}$$

where T^* is a characteristic time scale proposed by Ranger and Nicholls [29]

$$T^* = \frac{d_0}{U_g}\sqrt{\frac{\rho_l}{\rho_g}}. \tag{4.52}$$

Solving Equation 4.51 gives the following equation to describe the ratio of cross-stream diameter, d_d, to the initial droplet diameter, d_0

$$\frac{d_d}{d_0} = f(t^*, \text{We}_0) = \exp\left[C_{\text{bag}} t^* \sqrt{1 - \frac{6}{\text{We}_0}}\right], \tag{4.53}$$

where t^* is the ratio of elapsed time, t, to the characteristic time, T^*, and We_0 is the droplet We number calculated using the initial droplet diameter, $\text{We}_0 = \rho U_{\text{Rel}}^2 d_0/\sigma$. In this work, the value of C_{bag} is selected to be a function of We_0 and t^* based on a

non-linear regression of available experimental data

$$C_{\text{bag}} = t^* \left[0.2983 - \frac{0.2691}{1 + \left(\frac{\text{We}_0}{14.013} \right)^{13.629}} \right]. \tag{4.54}$$

Equations 4.53 and 4.54 can be rearranged so that C_{bag} is just a function of We_0

$$\frac{d_d}{d_0} = \exp \left[C_{\text{bag}} t^{*2} \sqrt{1 - \frac{6}{\text{We}_0}} \right], \tag{4.55}$$

$$C_{\text{bag}} = \left[0.2983 - \frac{0.2691}{1 + \left(\frac{\text{We}_0}{14.013} \right)^{13.629}} \right]. \tag{4.56}$$

Stage ii: bag rupture model

Chou and Faeth [16] argued that the bag rupture starts at approximately $t^* = 3$, while Opfer *et al.* [20] identified the rupture to happen at about $t^* = 2$. In this study, the initiation time of bag rupture, τ_{bag}, is determined using a correlation based on various experimental data

$$\tau_{\text{bag}} = \frac{C_{\tau,\text{bag}}}{1.0 - \frac{1.018}{\text{We}_0^{0.1818}}}, \tag{4.57}$$

which is a monotonically decreasing function of We_0 and $C_{\tau,\text{bag}}$ is a model constant with a nominal value of 0.8.

It is important to know the volume fractions of the bag and the remaining liquid torus ring in order to estimate the child droplet size. Chou and Faeth [16] have shown that the liquid bag can contain about 50% of the initial droplet volume. Assuming the liquid bag attached to the torus ring has a hemispherical shape, then the bag thickness,

h_{bag}, can be determined from mass conservation of the droplet

$$\frac{1}{2}h_{\text{bag}}\pi d_d|^2_{t^*=\tau_{\text{bag}}} = \phi_{\text{bag}}\frac{1}{6}\pi d_0^3, \tag{4.58}$$

where $d_d|_{t^*=\tau_{\text{bag}}}$, ϕ_{bag} are the cross-stream diameter and volume fraction of the liquid bag at $t^* = \tau_{\text{bag}}$, respectively. According to Equation 4.55, the cross-stream diameter is

$$d_d|_{t^*=\tau_{\text{bag}}} = d_0 f(t^*, \text{We}_0)|_{t^*=\tau_{\text{bag}}}. \tag{4.59}$$

Substituting Equation 4.59 into Equation 4.58 gives

$$h_{\text{bag}} = \frac{\phi_{\text{bag}} d_0}{3}\left[\frac{1}{f(t^*, \text{We}_0)|_{t^*=\tau_{\text{bag}}}}\right]^2. \tag{4.60}$$

Child droplets formed after the bag rupture are assumed to have a size proportional to the bag thickness, $d_c = C_{h,\text{bag}} h_{\text{bag}}$, where $C_{h,\text{bag}}$ is an adjustable constant with a nominal value of one. The number of child droplets formed by the bag rupture is

$$n_c = \frac{6 m_{d0}\phi_{\text{bag}}}{\pi \rho_l d_c^3} \tag{4.61}$$

Stage iii: liquid torus breakup model

After the bag rupture, the remaining liquid torus ring is assumed to continuously expand outwardly in the cross-stream direction with a constant rate equal to

$$\frac{\partial f(t^*, \text{We}_0)}{\partial t^*}|_{t^*=\tau_{\text{bag}}} = 2C_{\text{bag}}\tau_{\text{bag}}\sqrt{1-\frac{6}{\text{We}_0}}\exp\left[C_{\text{bag}}\tau_{\text{bag}}^2\sqrt{1-\frac{6}{\text{We}_0}}\right]. \tag{4.62}$$

Combining Equations 4.55 and 4.62 gives the following expression for bag and torus growth throughout the whole breakup process

$$\frac{d_d}{d_0} = \begin{cases} \exp\left[C_{\text{bag}} t^{*^2} \sqrt{1 - \frac{6}{\text{We}_0}}\right] & t^* \leq \tau_{\text{bag}} \\ \left[1 + 2C_{\text{bag}}\tau_{\text{bag}}\sqrt{1 - \frac{6}{\text{We}_0}}\left(t^* - \tau_{\text{bag}}\right)\right] \exp\left[C_{\text{bag}}\tau_{\text{bag}}^2\sqrt{1 - \frac{6}{\text{We}_0}}\right] & \text{otherwise} \end{cases}. \tag{4.63}$$

The liquid torus will eventually break into a few child droplets due to the RT instabilities [15, 28]. Thus, the breakup in this stage is tracked by the RT instability theory. The frequency of the fastest growing RT wave and its wavelength are calculated using the same formula as Equations 4.42 and 4.43. The RT instability wave is assumed to grow on the liquid torus surface if its wavelength is smaller than the liquid torus diameter, d_d. Once the wave begins to grow, the growth time is tracked and compared to the RT breakup time, τ_{RT}. The torus is assumed to break if the elapsed time is larger than τ_{RT}. The child droplet diameter is equal to the tube diameter of the torus ring, d_r, which can be estimated from the mass conservation

$$\frac{\pi d_r^2}{4}\pi d_d = \left(1.0 - \phi_{\text{bag}}\right)\frac{1}{6}\pi d_0^3, \tag{4.64}$$

which can be simplified and rearranged

$$d_r = d_0\sqrt{\frac{2\left(1.0 - \phi_{\text{bag}}\right)}{3\pi} f(t^*, \text{We}_0)^{-1}}, \tag{4.65}$$

and the number of child droplets is

$$n_c = \frac{6m_0\left(1.0 - \phi_{\text{bag}}\right)}{\pi\rho_l d_r^3} \tag{4.66}$$

Model implementation

A flow chart of the IAB model is provided in Figure 4.2. Note that the choice of sub-models depends on the droplet We number. If We is smaller than the critical We for breakup, We_{crit}, no breakup is assumed to happen since the droplet is in the oscillation/deformation breakup regime. If We is larger than We_{crit} and smaller than the transitional We for bag breakup We_{bag}, the phenomenological bag breakup sub-model is used. Finally, the KH-RT hybrid model is used if We is larger than We_{bag}. The value of We_{crit} is generally set to 12, though lower values (≈ 7) were found in the literature [21, 23]. In this work, its value is set to 6 since in Equation 4.55, a droplet with We larger than this value is predicted to form a slowly growing bag structure. However, the value of We_{crit} seems to have little impact on the spray characteristics. The We_{bag} number, on the other hand, has a negative impact on the predicted liquid penetration, based on the findings from a previous UQ study [83]. The reported values of We_{bag} in Table 2.1 range from 18 to 100. In this work, it is set to 56, a value roughly equals to the mean.

Bag characteristics

Bag characteristics at various We_0 numbers within the bag breakup regime are analyzed using Equations 4.56 and 4.63. Available experimental data from Chou and Faeth [16], Krzeczkowski [11], and Kulkarni [81] are used for validation purpose. The measurements were carried out with different experimental setups, but they all included a droplet generator, a wind tunnel or a shock tube, and optical diagnostic systems for velocity and droplet size measurements. For the sake of clarity, only the results along with the characteristic We_0 and Oh numbers are reported here. Figure 4.2 presents the temporal

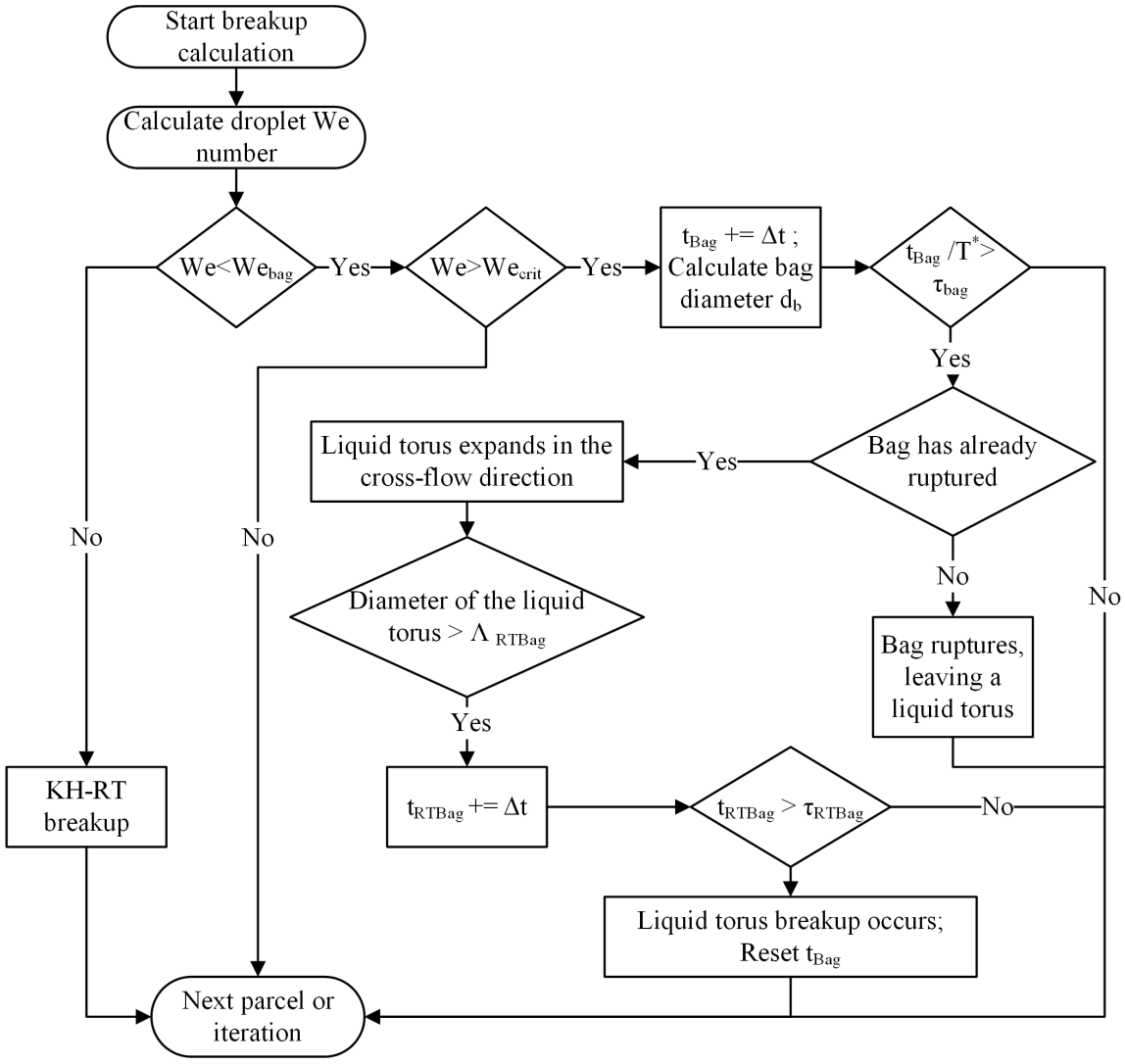

Figure 4.2: Flow chart of the IAB model.

evolution of measured and predicted cross-stream diameter ratios at various We_0 and Oh numbers. As the figure shows, the diameter ratio increases slowly during a short period after the droplet enters the disruptive gas field, indicating the transition from a spherical droplet to a relatively thin liquid disk. Then a liquid bag forms at the center of the deforming disk and grows rapidly due to the pressure difference inside and outside the bag. The rapid growth of the liquid bag also causes the thick torus ring attached to the open end of the bag to expand in the cross-stream direction. Finally, after the bag rupture, the remaining torus ring will continue to expand with constant velocity until it breaks due to RT instabilities. Note that the rate of cross-stream expansion is the largest when the bag structure still exists, which agrees with the findings in Ref. [16]. It is also interesting to notice that the droplet Oh number has little to no impact on the bag growth for the Oh range considered in Figure 4.2.

Predicted non-dimensional times of the start of bag rupture using Equation 4.57 are plotted in Figure 4.4 as a function of We_0, for Oh less than 0.1. The results also include measurement data of Opfer *et al*. [20], Krzeczkowski [11], Dai and Faeth [17], and the numerical predictions of Sachin *et al*. [84] using the VOF method. The We_0 range spans from the bag to sheet-thinning breakup regimes. As Figure 4.4 shows, the qualitative trend of the initiation time is well captured by present calculations and the VOF predictions. However, there exist some discrepancies among plotted data, which may be attributed to the vague definition of $t^* = 0$ among different studies.

It is of importance to understand how the model performs beyond the scope of experiments as illustrated in Figure 4.3. Hence, Figure 4.5 shows the predicted cross-stream diameter ratios for We_0 from 6 to 56, a wide range covers the bag and bag-stamen

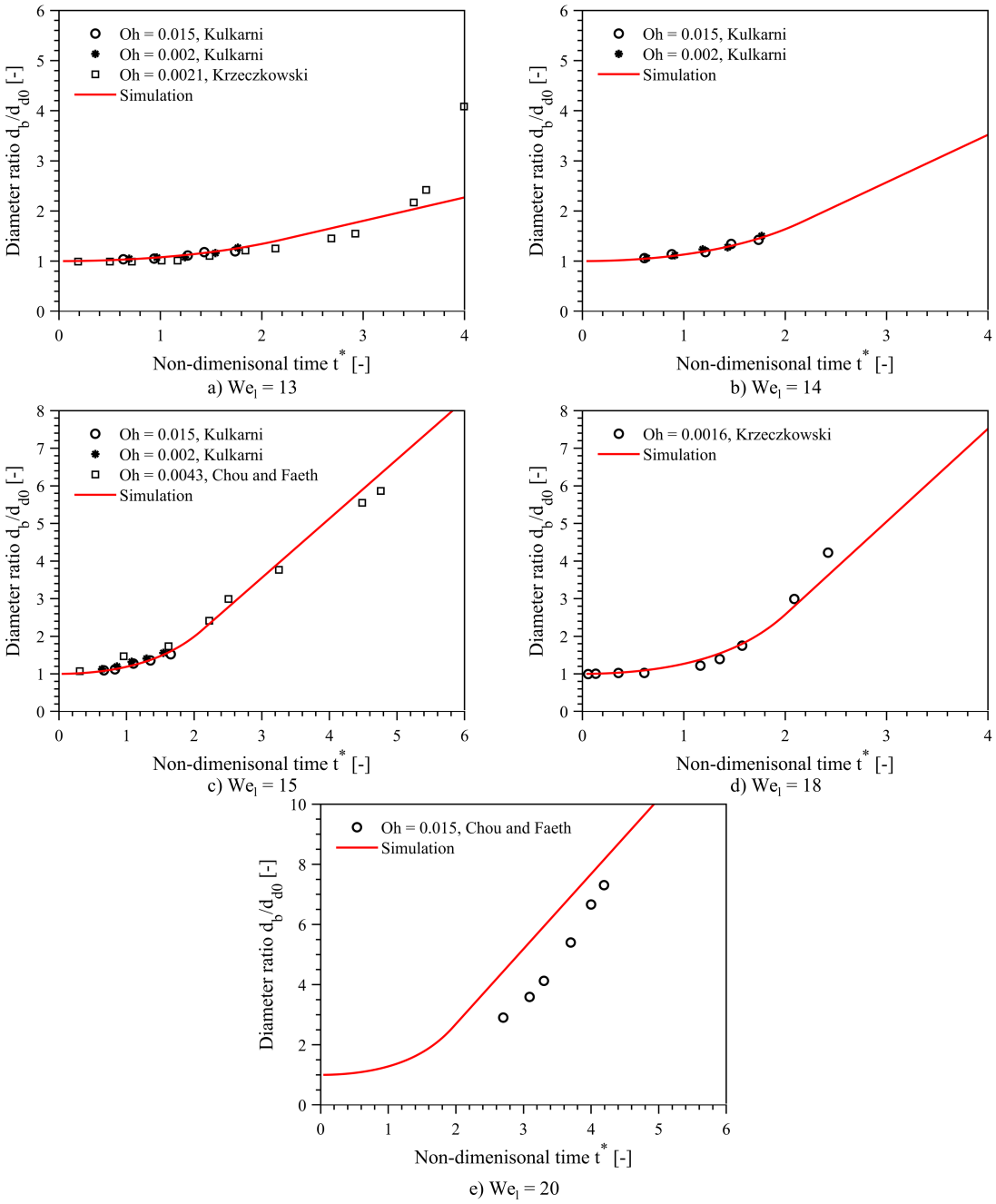

Figure 4.3: Measured and predicted cross-stream diameter ratio as a function of non-dimensional time at various We_0 and Oh numbers.

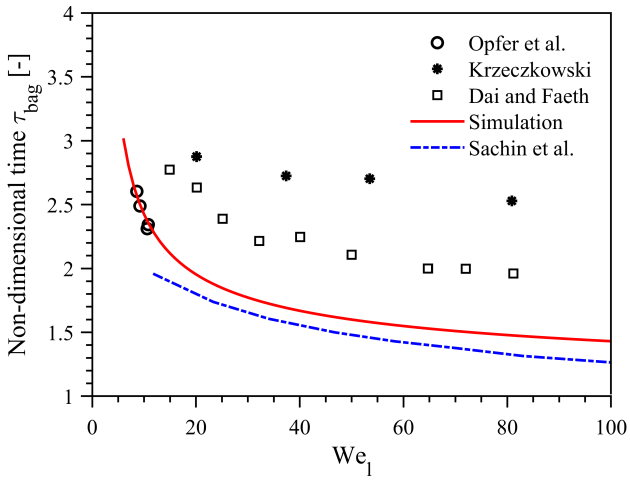

Figure 4.4: Measured and predicted non-dimensional time of the start of bag rupture as a function of We_0 number. Simulation results from Sachin *et al.* [84] using VOF method are also plotted for comparison purpose.

breakup. On each curve, the initiation time of bag rupture is also overlaid as an asterisk. At $We_0 = 6$, the droplet undergoes deformation/oscillation. Increasing We_0 further promotes a rapidly expanding liquid bag. On the other hand, the initiation time of bag rupture decreases as We_0 increases, leaving a shorter time for the torus ring to gain momentum from the growing bag. The competitive contributions from these two factors give a rather complicated behavior of the cross-stream diameter ratio. Before the bag ruptures, the growth rate increases monotonically with We_0 but the difference becomes less noticeable at higher We_0 values. After the bag ruptures, the liquid torus expands with a constant rate, whose value initially increases then decreases with increasing We_0. This behavior conveniently makes sure that the size of the liquid torus is not outrageously larger than the initial droplet diameter. It also offers some reassurance that the bag structure will not develop at very high We_0.

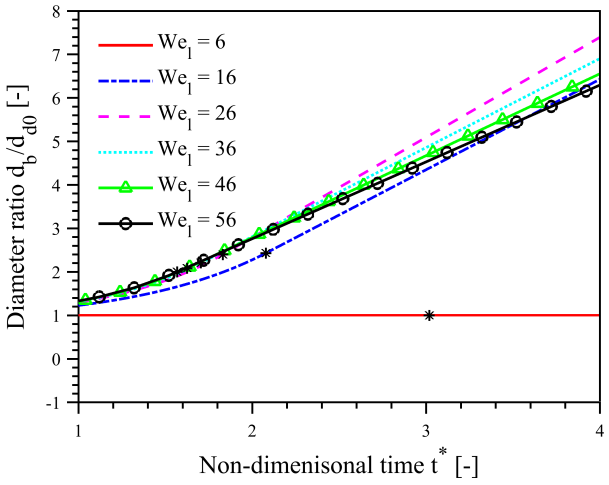

Figure 4.5: Predicted cross-stream diameter ratio as a function of non-dimensional time at various We_0 numbers. Asterisks are overlaid on each curve to illustrate the time of bag rupture.

4.4 Turbulent dispersion model

The SGS turbulent dispersion effects are expressed via the instantaneous gas-phase velocity at the droplet location, $u_{g,i}$, as in Equation 4.30. A common approach is to assume $u_{g,i}$ to contain two parts

$$u_{g,i} = u_i^* + u_i'', \tag{4.67}$$

where u_i^* and u_i'' are the deterministic and fluctuating parts, respectively. Depending on which approach to use, u_i^* and u_i'' can be estimated using various expressions. In the remaining of this section, the DRW model commonly found in the literature and the SGS dispersion model developed in this work will be described.

DRW model

In the DRW model, u_i^* is obtained from the resolved fields, $u_i^* = \widetilde{u}_i$. The fluctuating part, $u_i"$, is selected from a Gaussian distribution with a standard deviation equals to the characteristic SGS velocity

$$u_{k,\text{sgs}} = \sqrt{\frac{2k_{\text{sgs}}}{3}}. \tag{4.68}$$

The Gaussian-distribution has a mean of zero and it is given by [64]

$$G(u_i") = \frac{1}{\sqrt{2\pi u_{k,\text{sgs}}^2}} \exp\left(-\frac{{u_i"}^2}{2u_{k,\text{sgs}}^2}\right). \tag{4.69}$$

The fluctuating velocity, $u_i"$, is kept as constant until the droplet is estimated to pass a turbulent eddy. This droplet-eddy interaction is determined by two characteristic timescales, one corresponds to the time required for the droplet to pass through an eddy, τ_p, and the other to the eddy lifetime, τ_e. Various proposals have been reported in the literature to estimate τ_p, as reviewed by MacInnes and Bracco [85]. One of the most commonly used method, proposed by Gosman and Ioannides [64], assumes it to be

$$\tau_p = 0.1643\rho \frac{k_{\text{sgs}}^{1.5}}{\varepsilon_{\text{sgs}}|u_C|}, \tag{4.70}$$

where u_C is a characteristic velocity which can be estimated using various formulas. In this work, it is set to be the relative velocity between droplet and ambient gas, i.e., $u_C = (u_{g,i} - v_{d,i})$. In the work of Gosman and Ioannides [64], it is estimated to be the current fluctuating velocity, $u_i"$. The eddy lifetime, τ_e, is estimated to be

$$\tau_e = \rho \frac{k_{\text{sgs}}}{\varepsilon}. \tag{4.71}$$

Once $u_i"$ is selected from Equation 4.69, its lifetime is recorded and compared to the droplet-eddy interaction time, which can be written as [37]

$$\tau_i = \min\left(\tau_p, \tau_e\right). \tag{4.72}$$

If the lifetime of $u_i"$ is greater or equal to τ_i, a new $u_i"$ will be selected from Equation 4.69.

SGS model

In the SGS model, u_i^* is set to be the approximate deconvoluted velocity and $u_i"$ is the SGS part tracked by a stochastic differential equation (SDE). The approximate deconvolution method (ADM) is developed by assuming that the LES filter kernel G has an inverse G^{-1}, which can be approximated by the truncated Van Cittert series expansion [86]. Then u_i^* can be obtained by consecutively applying the filter

$$\begin{aligned} u_i" &= \sum_{\alpha=0}^{N} (I - G)^{\alpha} \circledast \widetilde{u}_i \\ &= \widetilde{u}_i + \left(\widetilde{u}_i - \widetilde{\widetilde{u}}_i\right) + \left(\widetilde{u}_i - 2\widetilde{\widetilde{u}}_i + \widetilde{\widetilde{\widetilde{u}}}_i\right) + \cdots . \end{aligned} \tag{4.73}$$

The first term on the right-hand side of Equation 4.73 is the filtered gas velocity obtained from Equation 4.5. The other terms represent the unresolved flow structures computed by filtering $\widetilde{u}_i$ with a test filter. The test filtering is defined in the real space and thus can be computed from the available LES field. It was found that the first three terms in Equation 4.73 can give reasonable results [60], and that including more terms may not improve the results significantly. Therefore, in this work only the first three

terms are included, which results in the following expression for u_i^*

$$u_i" = 3\widetilde{u}_i - 3\widetilde{\widetilde{u}}_i + \widetilde{\widetilde{\widetilde{u}}}_i. \tag{4.74}$$

Note that ADM can only recover flow scales on or larger than the LES filter size. The remaining SGS fluid velocity, $u_i"$, cannot be explicitly resolved and must be modeled. In the context of LES, liquid droplets subjected to the instantaneous SGS flow structures can be related to the Brownian motion (i.e., the apparently random movement of a particle in a fluid due to collisions with the molecules of the fluid) and, consequently, be governed by a Langevin-type equation. In the present study, the SDE proposed by Pozorski and Apte [87] is employed

$$du_i" = \frac{-u_i"}{\tau_{\text{disp}}}dt + \sqrt{\frac{2u_{k,\text{sgs}}^2}{\tau_{\text{disp}}}}\text{d}W_i \tag{4.75}$$

where τ_{disp} is a characteristic time scale and $\text{d}W_i$ is an increment of the Wiener process.

As discussed in Section 2.4, small and large droplets behave differently when subjected to a turbulent flow . To take this behavior into consideration, we proposed the following form of τ_{disp} based on the work of Pozorski and Apte [87]

$$\tau_{\text{disp}} = \begin{cases} C_{\text{disp}}\frac{\Delta}{u_{k,\text{sgs}}} & \text{St} \leq 1.0 \\ C_{\text{disp}}\frac{\Delta}{u_{k,\text{sgs}}\sqrt{1+\epsilon^2}} & \text{otherwise} \end{cases}, \tag{4.76}$$

where ϵ is the normalized drift velocity, $\epsilon = |\widetilde{u}_i - v_{d,i}|/u_{k,\text{sgs}}$, and C_{disp} is a constant with a nominal value of 0.1.

4.5 SGS energy dissipation model

As discussed in Chapter 1, the value of constant C in the classic energy dissipation rate model (i.e., Equation 3.1) requires *a priori* knowledge of the target flow and often needs to be tuned. In our experience, its value also needs to be scaled with a characteristic length in order to reach a good mesh independence of the vapor penetration. In this work, the characteristic length is selected to be the LES filter size close to the nozzle exit, Δ_{noz}. Once C is tuned for mesh a for a specific case, its value for mesh b is determined by

$$C_b = C_a \frac{\Delta_{\text{noz},b}}{\Delta_{\text{noz},a}}. \tag{4.77}$$

Another formulation of ε_{sgs} is developed based on the work of Chumakov and Rutland [73] and Pomraning and Rutland [69]. The proposed from of the model is

$$\varepsilon_{\text{sgs}} \approx \mu_C F \left[\widetilde{\frac{\partial \widetilde{u}_i}{\partial x_j} \frac{\partial \widetilde{u}_i}{\partial x_j}} - \frac{\widetilde{\partial \widetilde{u}_i}}{\partial x_j} \frac{\widetilde{\partial \widetilde{u}_i}}{\partial x_j} \right], \tag{4.78}$$

where μ_C is a characteristic viscosity, F is a function determined from *a priori* tests. The remaining part inside the bracket is a Leonard-type term, which is always positive for non-negative filters [70]. Examples of such filters are Box, Gaussian, and Linear filters [73]). Fourier cut-off filter assumes negative values in the real space so that the Leonard-type term may be negative as well. Fortunately, in engineering applications the Fourier cut-off filter is almost never used. Therefore, in this work a positive ε_{sgs} (i.e., sink for the SGS kinetic energy) is always implied.

Starting from the filtered momentum equation, a natural approach to estimate μ_C would be setting $\mu_C = \mu$. However, *a posteriori* test of this approach shows that us-

ing molecular viscosity would lead to severe under-estimation of the energy dissipation rate term, hence a proper budget of the SGS kinetic energy is not achieved. A second approach to model this term would be replacing it with the SGS viscosity: $\mu_C = \mu_{\text{sgs}}$. Recall that a convenient model for μ_{sgs} has already been given by Equation 4.25. Substituting it into Equation 4.78 leads to

$$\varepsilon_{\text{sgs}} \approx \rho C_k \Delta k_{\text{sgs}}^{0.5} F \left[\widehat{\frac{\partial \widetilde{u_i}}{\partial x_j} \frac{\partial \widetilde{u_i}}{\partial x_j}} - \frac{\widehat{\partial \widetilde{u_i}}}{\partial x_j} \frac{\widehat{\partial \widetilde{u_i}}}{\partial x_j} \right]. \tag{4.79}$$

Finally, the shape of function F needs to be found. From the study of Chumakov and Rutland [73], an appropriate approximation can be written as

$$F = C_\epsilon k^\upsilon \Delta^\gamma, \tag{4.80}$$

where υ and γ are scaling factors determined from *a priori* tests. Chumakov [72] found through DNS of forced isotropic turbulence that $\varepsilon_{\text{sgs}} \propto k_{\text{sgs}}^{0.5}$ for Δ close to the forcing scale. For Δ in the near viscous range, $\varepsilon_{\text{sgs}} \propto k_{\text{sgs}}^{1.0}$. Since the focus of this work is on engine sprays, where the size of Δ is considerably larger than the viscous length scale (i.e., Kolmogorov length scale), the value of υ is set to be zero, which effectively leads to the following scaling: $\varepsilon_{\text{sgs}} \approx k^{0.5}$.

According to the classic model of energy dissipation rate (i.e., Equation 3.1), ε_{sgs} scales inversely with Δ. Chumakov [72] argues that in the near viscous range, ε_{sgs} scales with the square of Δ. Assume this scaling is also valid for Δ in the forcing range, we can argue that

$$\varepsilon_{\text{sgs}} \approx \rho C_k C_\epsilon \Delta^2 k_{\text{sgs}}^{0.5} \left[\widehat{\frac{\partial \widetilde{u_i}}{\partial x_j} \frac{\partial \widetilde{u_i}}{\partial x_j}} - \frac{\widehat{\partial \widetilde{u_i}}}{\partial x_j} \frac{\widehat{\partial \widetilde{u_i}}}{\partial x_j} \right]. \tag{4.81}$$

The model constants C_k and C_ϵ can be combined together for practical implementations. Following a simple dimension check, we assume

$$C_k C_\epsilon = \frac{C_{\text{sgs}}}{d_{\text{noz}}}. \tag{4.82}$$

The final form of ε_{sgs} can therefore be written as

$$\varepsilon_{\text{sgs}} = \rho \frac{C_{\text{sgs}}}{d_{\text{noz}}} \Delta^2 k_{\text{sgs}}^{0.5} \left[\widehat{\frac{\partial \widetilde{u}_i}{\partial x_j}} \widehat{\frac{\partial \widetilde{u}_i}{\partial x_j}} - \widehat{\frac{\partial \widetilde{u}_i}{\partial x_j}} \widehat{\frac{\partial \widetilde{u}_i}{\partial x_j}} \right], \tag{4.83}$$

where the default value of C_{sgs} is set to be 0.11.

5 RESULTS AND DISCUSSION

Evaluation of the spray models developed in Chapter 4 is carried out in a step-wise fashion, from DISI spray breakup modeling to an uncertainty quantification (UQ) study, then from the SGS turbulent dispersion modeling to the SGS energy dissipation rate modeling. The discussion focuses primarily on the breakup modeling under DISI engine-like conditions. In the following sections, the spray experiments are briefly described, followed by the simulation setup. Then the experimental and numerical methods to obtain characteristics of the spray results will be introduced. Finally, the results and discussion will be provided.

5.1 Spray experiments

Two sets of experimental data are used in this work for the calibration and evaluation of LES spray models. One of them, termed as the "Spray G", is taken from the Engine Combustion Network (ECN). The remaining set, termed as the "GM DISI sprays", are taken General Motors (GM) publications described below.

The ECN Spray G condition, simulated by igniting a premixed combustible gas mixture that burns to completion, corresponds to a non-reacting early injection case in DISI engines [88]. The Spray G injector has eight symmetrically spaced holes, each with a nominal plume direction of 37°. Table 5.1 lists the injector specifications and operating conditions. Further details can be found on the ECN website [89]. GM DISI spray data are taken from the work of Parrish *et al.* [80, 90]. Measurements were conducted under late injection DISI engine-like conditions. Iso-octane was injected into a high-

temperature pressure vessel by a multi-hole DISI injector. The injector has eight symmetrically spaced holes, each with an inner orifice diameter of 0.140 mm. The measured plume direction of this injector is 25°. A continuous flow of nitrogen passing through the vessel is used to provide evacuation of fuel vapor and residual droplets. Test conditions and details of the injector are also listed in Table 5.1.

Table 5.1: Operating conditions and injector specifications for spray experiments used in this work.

Data type	**Spray G**	**GM DISI**
Ambient gas density (kg/m3)	3.5	3.0, 6.0, 9.0
Ambient gas composition (-)	N_2, CO_2, H_2O	N_2
Ambient gas temperature (K)	573	400, 500, 600, 700, 800, 900
Ambient gas pressure (bar)	6	3.56 - 24.04
Ambient gas velocity (m/s)	≈ 0	≈ 0
Fuel temperature (K)	363	363
Injector orifice diameter (mm)	0.172	0.14
Injection pressure (MPa)	20	20
Injection duration (ms)	0.78	0.865
Injected fuel mass (mg)	10	10
Plume direction (°)	35	25

The ambient conditions for both Spray G and GM DISI spray experiments are summarized in Figure 5.1. Note that for GM DISI sprays, the spray characteristics were acquired with ambient temperatures ranging from 400 to 900 K at intervals of 100 K. At each temperature, three test conditions corresponding to the ambient densities of 3.0, 6.0, and 9.0 kg/m^3, were defined by adjusting the ambient pressure. Four conditions, represented by cases 1 - 4 on the figure, are selected to validate the IAB model and to obtain an optimal value of the model parameter C_β in Equation 4.45.

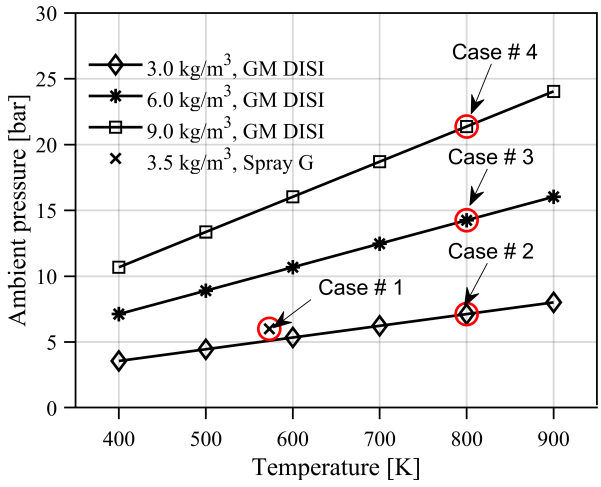

Figure 5.1: Experimental ambient conditions for ECN Spray G and GM DISI sprays. Symbols indicate conditions where experimental measurements were taken. Circles indicate four baseline conditions where the model validation and calibration are conducted.

5.2 Simulation setup

LES spray simulations are carried out using spray and turbulence models described in Chapter 4. Details of the simulation setup will be given in the following subsections.

CFD mesh and boundary conditions

A 100 × 100 × 100 mm cubical domain composed of hexahedra cells is used for LES spray simulations. The domain size is slightly smaller than the actual length of the constant volume vessel (108 mm) but is large enough to minimize the effects of boundary conditions on simulation results. The base mesh has a uniform cell size of 1.0 mm. Two additional meshes are generated with non-uniform node spacing for the sake of reasonable CPU time. Near-nozzle static mesh refinement is employed in both meshes, where the smallest cell sizes are 0.5 and 0.375 mm, respectively. Figure 5.2 shows an x-y cut-

plane of the 0.375 mm, in which a gradually increased node spacing is noticeable from the injector location to the mesh boundaries. Note that particular attention is paid to the representation of the injector tip in all three tested meshes, as the embedded sub-figure shows. According to a previous study of Van Dam and Rutland [91], the injector tip needs to be approximated in the mesh to prevent false entrainment of ambient gas. Wall boundary conditions are applied to the injector tip surfaces in each mesh. The total number of cells are approximately 1.1, 1.0, and 1.6 million for the 1.0, 0.5, and 0.375 mm meshes, respectively.

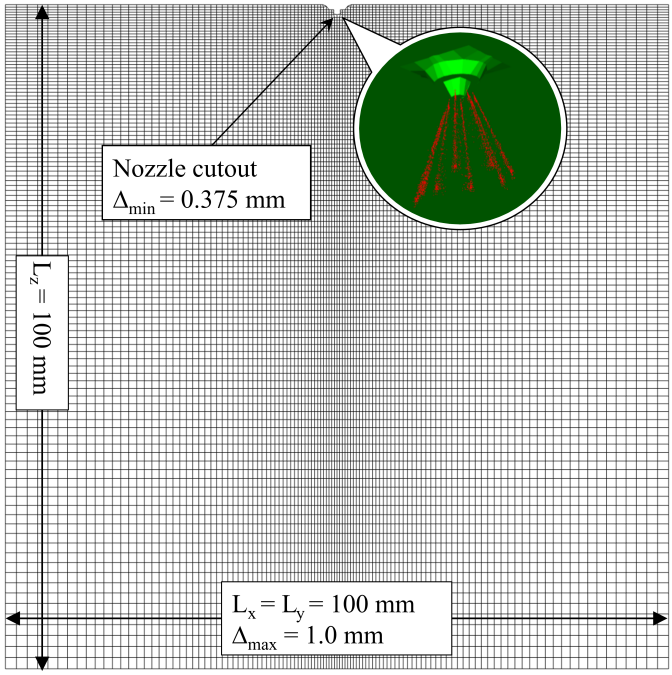

Figure 5.2: Cut-plane of the cubic mesh with a nominal cell size of 1.0 mm for spray simulations. A nozzle cutout approximating the geometry of the multi-hole injector is included to guide the air entrainment near nozzle exit [61], as the embedded sub-figure shows.

Details of the boundary conditions for spray simulations are provided in Table 5.2.

Table 5.2: Summary of boundary conditions applied on the meshes surfaces.

Term	Boundary conditions
Temperature	Dirichlet
Velocity	Dirichlet
Pressure	Neumann with zero gradient
Species mass fraction	Neumann with zero gradient

As a general rule of thumb, Neumann boundary conditions with zero gradients are set for pressure and species mass fractions on the mesh surfaces, while Dirichlet boundary conditions are applied for velocity and temperature on mesh surfaces representing the physical wall of the vessel. In this work, the DISI meshes resemble the actual vessel geometry (though slightly smaller), and hence constant temperatures and velocities are applied for all six mesh surfaces.

Discretization methods and initial conditions

The Eulerian gas-phase equations reviewed in Section 4.1 are discretized using different schemes depending on the terms, as summarized in Table 5.3. For the time derivatives in Equations 4.5, 4.6, and 4.23, the implicit Euler scheme is used. For the remaining gradient, divergence, and Laplacian terms, the Gauss's theorem is employed which relates the surface integrals with volume integrals. In OpenFOAM, values of variables are stored at the cell centers. Therefore, the surface integrals require the interpolation of values from cell centers to surface centers. The default interpolation scheme is linear which results in central differencing, but other schemes can be specified by the second entry for each term as listed in Table 5.3. In this work, second order cubic scheme is used for the convection term in the filtered Navier-Stokes equation, Equation 4.5; the linear

scheme is used for the resolved kinetic energy in Equation 4.6; and finally, the first-order upwind scheme is used for the remaining divergence terms. Note that evaluations of Laplacian terms require the calculation of surface normal gradient terms. In this work, the CFD meshes are typically aligned with the Cartesian coordinates system, with the exception of the nozzle cutout for DISI sprays. This conveniently guarantees that the gradients normal to cell surfaces are second-order accurate with central differencing. The explicit non-orthogonal correction is applied to those cell surfaces that are aligned with the coordinates system with an angle. More information about the numerical schemes in OpenFOAM can be found in Refs. [92, 93].

Table 5.3: Details of the numerical schemes for the finite volume discretization of LES gas-phase governing equations.

Term	**Finite Volume Scheme**
Time derivative	Implicit Euler
Gradient	Gauss linear
	Gauss cubic for Equation 4.5
	Gauss linear for K in Equation 4.6
Divergence	Gauss upwind for $\widetilde{h}_s$ in Equation 4.6
	Gauss upwind for Equation 4.7
	Gauss upwind for Equation 4.23
Laplacian	Gauss linear orthogonal
Surface normal gradient	Explicit non-orthogonal correction
Interpolation scheme by default	Central differencing

As described in Section 5.1, the spray experiments for comparison were carried out in constant volume vessels, hence the ambient gas velocities are initialized with zeros for all simulations. The mixed-type dynamic structure turbulence model utilizes a transport equation for k_{sgs}, therefore non-zero values should be initialized in order for k_{sgs} to

self-propagate. For Spray G, the initial k_{sgs} is set to be 0.0079 m^2/s^2, as recommend by ECN [94]. For GM DISI sprays, its value is set to be 0.00016 m^2/s^2 following a previous study of Van Dam and Rutland [91]. In our experience, the initial value of k_{sgs} has little impact on the results so long as its value is non-zero. The initial gas-phase pressure, temperature, and liquid-phase temperature are set according to the experimental conditions listed in Table 5.1.

The liquid jet velocities at nozzle exit are determined using the following equation

$$U = \frac{\dot{m}}{\rho_l C_A N_{\text{noz}} A_{\text{noz}}}. \tag{5.1}$$

where $\dot{m}$ is fuel mass flow rate that can be estimated from the measured rate of injection (ROI) profiles and the total injected quantities, C_A, N_{noz}, and A_{noz} are the area contraction coefficient, number of nozzle holes, and the nozzle orifice area, respectively. The recommended ROIs for spray experiments are plotted in Figure 5.3. Note that the ROI for GM DISI sprays is shifted to the right by 1 ms for a better illustration. Neither Spray G nor GM DISI spray has the sufficient injected quantity to promote steady spray structures and therefore result in highly transient sprays. Therefore, simulation results of Spray G presented in this work are the average of five realizations, each with a different random number seed in the cone-angle injection model (See Ref. [6] for more details), as suggested by Sphicas *et al.* [95]. In our experience, however, just by changing the random number seed in the injection model does not have a significant impact on the results, especially on the liquid- and vapor-phase penetrations, due to the fact that the random number seed only affects the directions of initial droplet velocity vectors. Therefore, the results of GM DISI sprays presented in the remaining of this work are

from single realizations. The number of parcels injected into the computational domain is fixed at 80000 for all spray simulations.

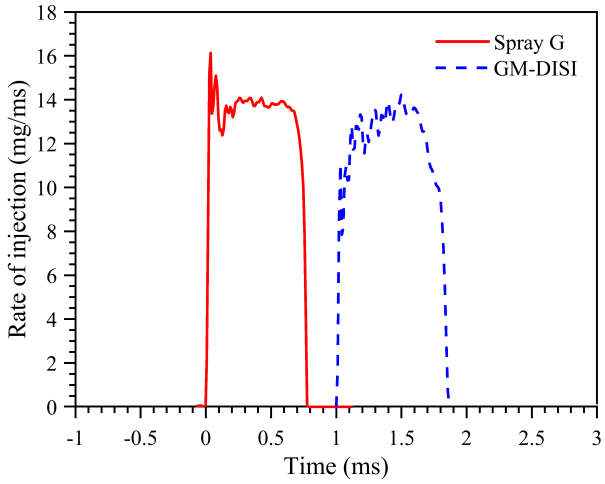

Figure 5.3: Rate of injection profiles for spray simulations. Note that the ROI for GM DISI sprays are shifted to the right by 1 ms for a clear illustration.

Another necessary input for the estimation of initial liquid velocity is the area-contraction coefficient, C_A, as shown in Equation 5.1. Unfortunately, extra measurements of the momentum flow rates are needed to determine the value of this coefficient. Therefore, most experimental work instead reports the discharge coefficient, C_D. The discharge coefficient is defined as the product of the area-contraction coefficient and the velocity coefficient, $C_D = C_A C_V$. The velocity coefficient, C_V, is the ratio of exit liquid velocity and the maximum potential liquid velocity determined from the Bernoulli's equation, hence its value is always smaller than 1.0. This generally leads to an over-estimation of liquid velocity at the nozzle exit if one simply assumes $C_A = C_D$ (which is unfortunately true for most spray modeling work in the literature). For diesel sprays, this assumption is generally considered to be acceptable since both C_A and C_D are very sim-

ilar in value. For example, the ECN Spray A diesel injectors have discharge coefficients around 0.90 and area-contraction coefficients around 0.98 [96], which leads to roughly 9% over-estimation of liquid jet velocity at the nozzle exit. For DISI sprays, however, the area-contraction coefficient is much lower than its diesel counterpart, possibly due to the high volatility of gasoline and relatively low injection pressure. In a recent study by Payri *et al*. [97], the average area-contraction coefficient for a Spray G injector is measured to be around 0.7, while the average discharge coefficient is measured to be below 0.5. The liquid velocity at the nozzle exit will be over-estimated by 40% if one assumes $C_A = C_D$. In this work, the area-contraction coefficients for spray simulations are estimated to be around 0.7 – 0.8.

Simulations of Spray G are carried out following the ECN convention displayed in Figure 5.4. Note that the coordinates origin has been defined as the tip of the injector, which means the eight nozzle-holes are located at slightly negative axial positions. The plume direction and plume cone angles are two critical parameters affecting plume-to-plume interactions, as one may expect. Unfortunately, these parameters can hardly be measured due to the difficulties and uncertainties associated with experimental measurements in the near-nozzle region. Consequently, the plume direction in this work is estimated using a variable profile ranging from 37° to 33° according to the experimental work of Manin *et al*. [98]. The plume cone angle is set to be 25° based on a previous study by Pickett [99].

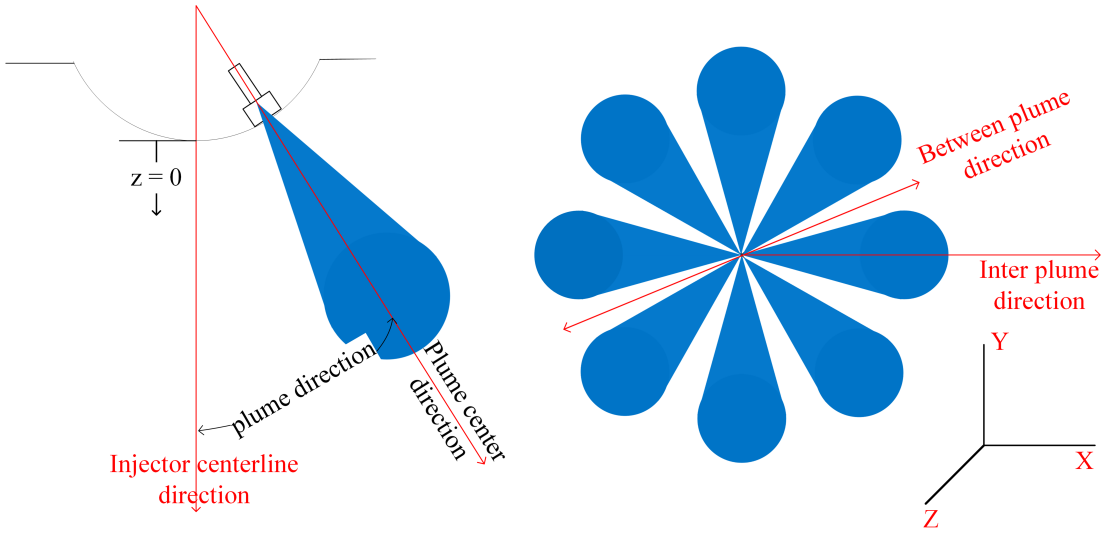

Figure 5.4: Schematic of Spray G coordinates for simulation setup and data processing.

Spray sub-models and test matrix

In addition to the spray models described in Sections 4.3 - 4.5, several spray-related sub-models are also employed in this work for LES spray simulations. Droplet heat transfer is described using the Ranz-Marshall model [100]. Droplet evaporation is described using a model based on the ideal gas assumption and droplet Sherwood number [6]. The droplet collision and coalescence are neglected. The liquid properties are calculated using the National Standard Reference Data System (NSRDS) functions. The gas properties are interpolated from the NIST-JANAF thermochemical tables [101]. Finally, the ambient is assumed to behave like an ideal gas.

Tests of spray models are carried out in a step-wise fashion. First, the IAB model is validated and calibrated for cases 1 - 4 as summarized in Table 5.4. Followed by this, it is applied to more GM DISI conditions without further tuning the model parameter

to evaluate its performance. An uncertainty quantification study is then performed for case 3 to examine the impact of uncertainties in spray boundary conditions and model parameters on spray characteristics. Following the breakup modeling, the test results of SGS dispersion and energy dissipation rate models are conducted for cases 1, which is further divided into five sub-cases as summarized in Table 5.5.

Table 5.4: Text matrix for the evaluation of spray models. For each specific case, a check mark indicates a study has been performed or a model has been tested, a cross mark means otherwise.

Case #	Description	IAB	UQ	SGS Dispersion	SGS Dissipation
1	Spray G	✓	✗	✓	✓
2	GM DISI, 800K, 3.0kg/m^3	✓	✗	✗	✗
3	GM DISI, 800K, 6.0kg/m^3	✓	✓	✗	✗
4	GM DISI, 800K, 9.0kg/m^3	✓	✗	✗	✗
-	Other GM DISI conditions	✓	✗	✗	✗

Table 5.5: Test matrix for the SGS dispersion and energy dissipation rate modeling using Case 1 from Table 5.4.

Case #	Dispersion model	Energy dissipation model
a	No dispersion	Classic w/ scaling
b	DRW	Classic w/ scaling
c	SGS	Classic w/ scaling
d	SGS	Classic w/o scaling
e	SGS	Dynamic

5.3 Data acquisition and processing

Experimental data are collected from the ECN website and the literature for comparison purposes. Those data include liquid- and vapor-phase penetrations, projected liquid

volume (PLV) fractions, liquid- and vapor-phase envelops, and spatial distributions of droplet velocities and SMD. Table 5.6 lists the specific data types and their sources for each spray experiments. In each entry, the measurement devices are also specified. Details of the experimental setup are not provided here for the sake of clarity.

Table 5.6: Summary of experimental data used in this work.

Data type	**GM DISI**	**Spray G**
Liquid penetration	Mie-Scatter, Scott Parrish [80, 90]	Mie-Scatter, Manin *et al.* [98]
Liquid extinction length	-	DBI, Manin *et al.* [98]
PLV profiles	-	DBI, Joshua Lacey [102]
Droplet velocity and SMD	-	PDI, Scott Parrish [103]
Liquid envelops	Mie-Scatter, Scott Parrish [80, 90]	DBI, Joshua Lacey [102]
Vapor envelops	Schlieren, Scott Parrish [80, 90]	-
Vapor penetration	Schlieren, Scott Parrish [80, 90]	Schlieren, ECN [104]

Simulation results are processed following the ECN standard and recommendations if applicable [105]. Macroscopic spray characteristics such as the liquid- and vapor-phase penetrations are calculated using the methods summarized in Table 5.7. The predicted vapor-phase penetration is defined as the axial distance along the nozzle centerline where the local fuel mixture fraction is 0.1%. Line-of-sight liquid-phase measurement techniques, such as volume-illuminated Mie-scatter imaging and diffused back-illumination imaging (DBI), are used by GM and ECN to define the liquid region and hence the penetration length. With Mie-scatter imaging, the light signal is proportional to the square of the incident particle diameter [106]. DBI or laser absorption use light extinction (light deflection or absorption) produced by the spray droplets, thus providing a measure related to the cube of droplet diameter [107]. On the other hand, the conventional way to determine liquid-phase penetration in most CFD studies is based on the accumulated

liquid mass fraction. To reduce the difference between the numerical and experimental methods of measuring liquid-phase penetration, line-of-sight integrated droplet surface area method (i.e., Mimic Mie-scatter or MMC) [91] and projected liquid volume fraction method (PLV) [102] are employed in this work.

Table 5.7: Post-processing methods for the estimation of liquid- and vapor-phase penetrations.

Data type	**Method**
Vapor penetration	Axial distance with a minimum fuel mass fraction of 0.1%
Liquid penetration	Mimic Mie-Scatter method for Mie-scatter imaging
Liquid extinction length	Projected liquid volume method for DBI measurements

A schematic of the line-of-sight methods is provided in Figure 5.5. Assuming the x-axis is the camera line-of-sight direction, then the total droplet surface area or volume for each CFD cell is calculated and projected along the x-direction, resulting in a two-dimensional map of integrated droplet surface area or volume. The liquid-gas bound is then defined using a predefined threshold. For the integrated droplet surface area method, this threshold is selected to be roughly equal to 3% of the maximum integrated surface area [91]. For the projected liquid volume method, two thresholds are used as recommend by ECN [107]: 2.0×10^{-4} mm^3-liquid / mm^2 (referred to as the "low" threshold) and 2.0×10^{-3} mm^3-liquid / mm^2 (referred to as the "high" threshold).

Predicted liquid-phase penetrations for case 1 using the aforementioned methods are provided in Figure 5.6. Also plotted are the liquid penetrations measured using Mie-scatter imaging and DBI from Manin *et al*. [98]. The predicted penetration curve using the conventional accumulated liquid mass method is also plotted for comparison purpose. The predicted liquid-phase penetrations are very close to each other during the

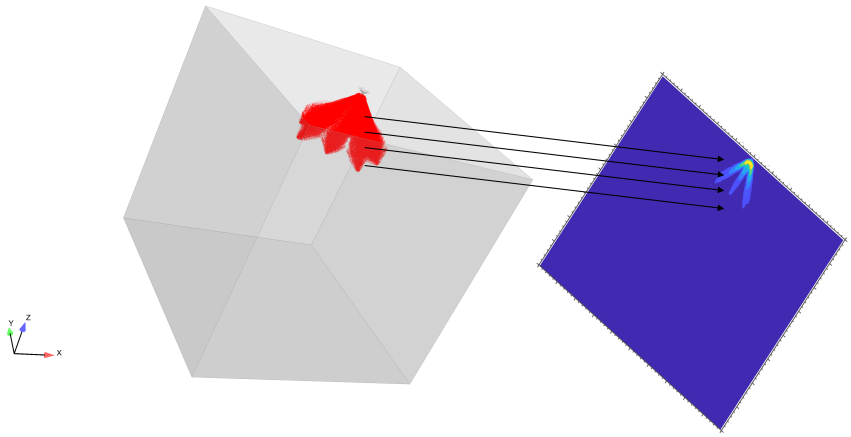

Figure 5.5: Schematic of the line-of-sight methods for the estimation of liquid-phase penetrations. Arrows indicate the camera line-of-sight direction. Figure on the left illustrates the liquid parcels in a CFD domain. Figure on the right shows the resulting line-of-sight integrated liquid surface area or volume.

initial period of injection. Small deviations are noticeable after the spray structure establishes a "quasi-steady" state at 0.5 ms ASOI. The predicted trends follow the measurement curves quite well until the end of injection, 0.78 ms ASOI. The accumulated mass method keeps giving non-zero penetration throughout the simulation, and thus fails to capture the retracting liquid tip. The MMS and PLV methods, on the other hand, are able to predict a rapid dropping of liquid penetration. Another interesting finding from Figure 5.6 is that there are some inconsistencies between the Mie-scatter imaging and DBI measurements, especially for the liquid residence time. DBI is recommended by ECN [107], but Mie-scatter imaging was used for GM DISI sprays and is more commonly found in the literature.

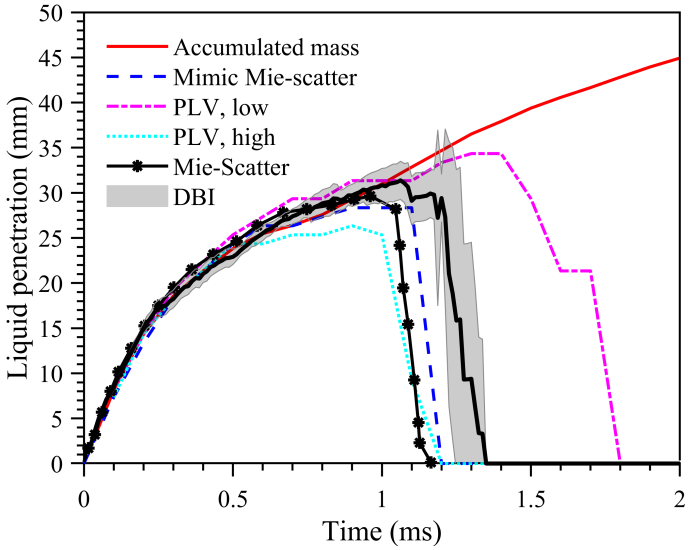

Figure 5.6: Comparison of liquid-phase penetrations estimated using various methods.

5.4 Spray breakup modeling

In this section, simulation results under DISI conditions illustrated in Figure 5.1 are presented and discussed. Targeted spray characteristics include penetrations, droplet velocity and SMD profiles as summarized in Table 5.6. The initial model validation and calibration will be presented first, followed by more discussions focusing on the IAB breakup characteristics. Then, an attempt to correlate the optimal breakup model parameter values with the ambient conditions is made and the found values are tested at more DISI spray conditions. Finally, results of the UQ study for case 3 is presented.

Mesh resolution study

For the mesh resolution study, single LES realizations are run with the IAB breakup model for case 1. Predicted liquid- and vapor-phase penetrations are shown in Figure 5.7.

Also plotted are experimental data obtained using Mie-scatter imaging and Schlieren from SNL and Institute Motori [98, 104]. For liquid-phase penetrations shown in Figure 5.7a, the results converge when the cell sizes are smaller or equal to 0.5 mm. The estimated liquid residence times (defined as the time when liquid-phase penetration falls back to zero) are the same among all three meshes. The 1.0 mm mesh predicts slightly higher liquid-phase penetration compared to the other two after 0.6 ms ASOI, but the difference is not significant, and the predicted trends follow each other closely. For the vapor-phase penetrations shown in Figure 5.7b, both 1.0 and 0.5 mm meshes predict very similar results throughout the simulation, and the 0.375 mm mesh predicts slightly higher vapor-phase penetration after 0.5 ms ASOI. Results from all three meshes match the Schlieren data from Institute Motori reasonably well but fail to match the SNL data. Overall, the LES results are less sensitive to the mesh sizes compared to Ref. [61], which may be attributed to three factors

1. The one-equation turbulence model has a transport equation for k_{sgs}. This provides an energy budget on the SGS level and works well in engine applications, where the number of grid cells must remain reasonable [4]

2. The modified near-nozzle geometry prevents the false air entrainment from above the nozzle hole exit locations and thus ensures that the expected flow pattern can be reproduced [91].

3. DISI injectors operate at much lower injection pressures compared to the diesel counterpart, therefore they do not require very fine mesh to capture the relevant turbulence scales [91].

The 1.0 mm mesh is therefore used for the remaining part of this work due to its uniformity and reduced computational cost, which is important considering the focus of this work is to develop spray models tailored for DISI engine simulations, where the mesh resolution must retain reasonable.

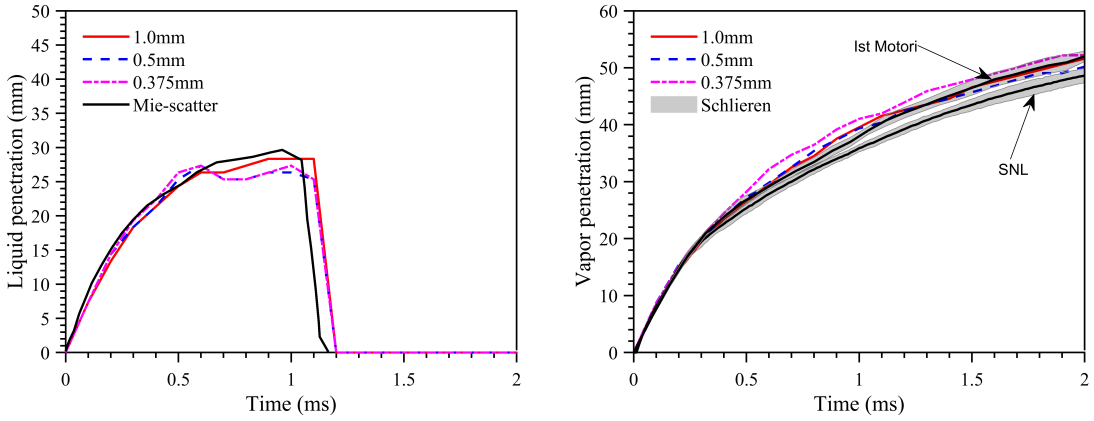

(a) Liquid-phase (b) Vapor-phase

Figure 5.7: Liquid- and vapor-phase penetrations for case 1 using three mesh resolutions of 1.0, 0.5, and 0.375 mm. The experimental data are plotted with the mean only. The simulation results are from single realizations for each mesh.

Model validation and calibration

Validation of the IAB model is performed by comparing its predictions with experimental data for cases 1 - 4 illustrated in Figure 5.1. The "best practice" results obtained using the KH-RT model are also presented for comparison purposes. In this work, "best-practice" is achieved by adjusting the spray model parameters until an optimal matching between the simulations and experiments are achieved for both the liquid- and vapor-phase penetrations.

Liquid- and vapor-phase penetrations

Predicted liquid- and vapor-phase penetrations for case 1 are plotted in Figures 5.8 - 5.10. In each figure, experimental data for penetration measurements are also plotted with the shaded area representing the 95% confidence levels or standard deviations, if available. Starting with Figures 5.8 - 5.9, where the liquid-phase penetrations (also called "liquid extinction length" if measured by DBI) calculated using the MMS and PLV methods are plotted. During the early period of injection ($t < 0.2$ ms ASOI), results with both models match the measured curves very well. Then, the penetration curves become parabolic due to droplet breakup and aerodynamic drag after approximately 0.2 ms ASOI. Noticeable differences between simulations are observed during the period of quasi-steady state of injection ($0.5 < t < 0.7$ ms ASOI), especially in Figures 5.9a and 5.9b where results are post-processed using the PLV profiles. A better matching to the experimental data is given by the IAB model during this period. The liquid penetration will eventually go to zero due to evaporation. The measured time of this transition spans from 1.1 to 1.35 ms ASOI due to difficulties in the measurements and large spray-to-spray variations. In Figure 5.8, both models capture this timing quite well. In Figures 5.9a and 5.9b, however, neither of them is able to match the measurements. The IAB model matches the measured trend. The KH-RT model, on the other hand, predicts the liquid-phase to keep penetrating further downstream.

The vapor-phase penetrations in Figure 5.10 show noticeable deviations from the measured data by SNL after the quasi-steady state is reached at around 0.5 ms ASOI. The difference is likely due to the somewhat arbitrarily defined plume cone angle in LES simulations. Since the plume interactions at the standard Spray G condition are

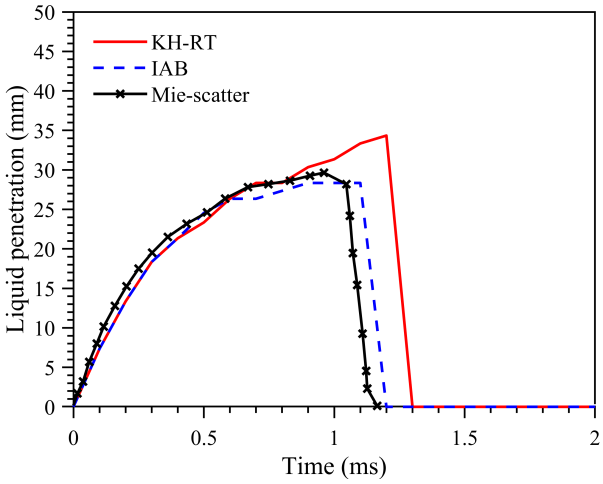

Figure 5.8: Liquid-phase penetrations for case 1 (Spray G condition). The predicted results are processed with the MMS method. The experimental data are plotted with the mean only.

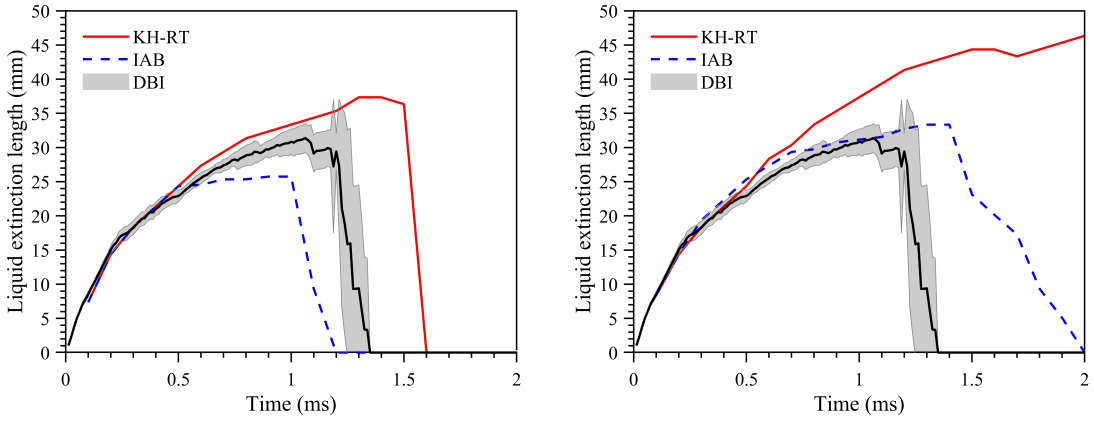

(a) "high" threshold

(b) "low" threshold

Figure 5.9: Liquid extinction lengths for case 1 (Spray G condition). The predicted results are processed from the PLV profiles with the “high” and "low" thresholds. The experimental data are plotted with the shaded area representing the standard deviations.

quite noticeable, estimating the plume cone angle from the Mie-scatter images seems to be impractical and inaccurate. In this study, the plume cone angle is approximated by a constant value of 25°. On the other hand, the measured curve by Institute Motori at the same condition is well represented by both the IAB and the KH-RT models, indicating a good agreement between simulations and experiments. The discrepancies between measurement data are likely due to the small differences in the optical setups and spray injectors (even though the nominal specifications are the same) between SNL and Institute Motori.

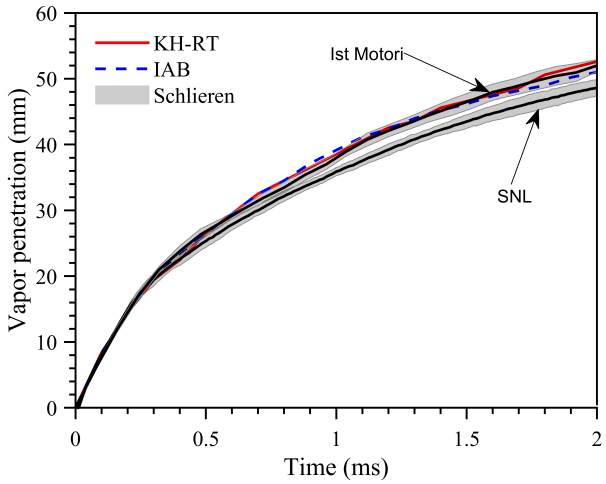

Figure 5.10: Vapor-phase penetrations for case 1 (Spray G condition). The predicted results are processed with a local fuel mass fraction of 0.001. The experimental data are plotted with the shaded area representing the 95% confidence levels.

Figures 5.11 – 5.13 show the measured and predicted penetration data for cases 2 – 4. An immediate observation is that simulations with the IAB model match the experimental data very well at all three conditions for the liquid-phase penetration. Similar to case 1, the spray structures reach quasi-steady states around 0.5 ms ASOI. The liquid

length (defined as the maximum liquid penetration) is well captured by the IAB model as well. On the other hand, the KH-RT model under-predicts the liquid penetration at both 3.0 and 6.0 kg/m^3. The effects of changing the ambient density on the liquid penetration while maintaining the temperature at 800 K are also shown in Figures 5.11a, 5.12a, and 5.13a. By normalizing with respect to the ambient density of 3.0 kg/m^3, the liquid length reduces by about 33% for the 6.0 kg/m^3 ambient density and 42% for the 9.0 kg/m^3 ambient density. The reduction in liquid length at higher ambient density is expected, since the enhanced breakup leads to increased total surface area, which greatly reduces the life span of small droplets.

The predicted vapor-phase penetrations in Figures 5.11b and 5.12b match the experimental data to within the 95% confidence levels except for the very end of simulation at 6.0 kg/m^3. In Figure 5.13b, both models tend to over-predict the penetration of vapor-phase just before the end of injection. Like the liquid-phase, increasing ambient density also causes a reduction in vapor penetration. Overall, the penetration results of vapor-phase show little difference between the KH-RT and the IAB models.

Droplet velocity and SMD distributions

Comparison of the droplet velocity and SMD distributions subject the models to a more rigorous examination. Data are sampled for case 1 in the inter plume direction at 15 mm axial position (as illustrated in Figure 5.4), a location where the experimental data are available. The ensemble-averaged droplet velocity and SMD distributions from eight plumes and five realizations are plotted with PDI data in Figures 5.14 and 5.15 at six selected times ASOI. Starting with sub-figures 5.14a and 5.14b, where the spray reaches

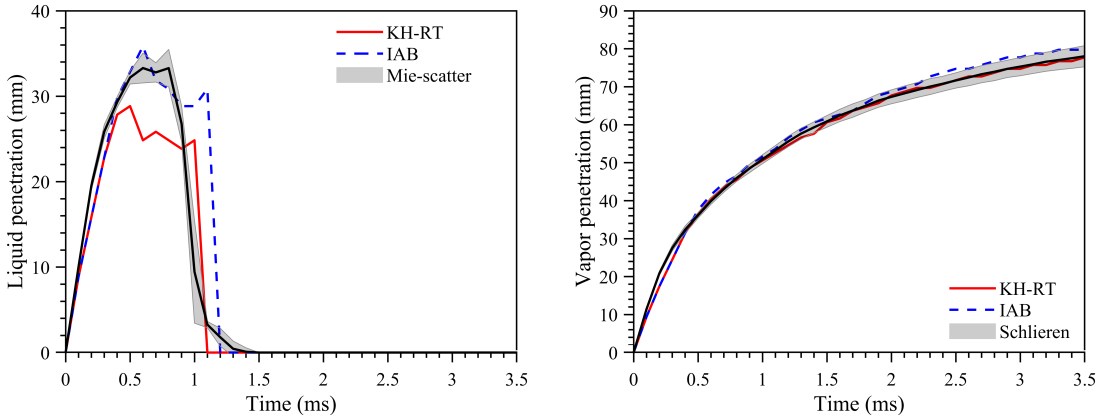

(a) Liquid-phase (b) Vapor-phase

Figure 5.11: Liquid- and vapor-phase penetrations for case 2 (GM DISI sprays at 800K, 3.0 kg/m^3). The experimental data are plotted with the shaded area representing the 95% confidence levels. Simulation results are from single-realizations.

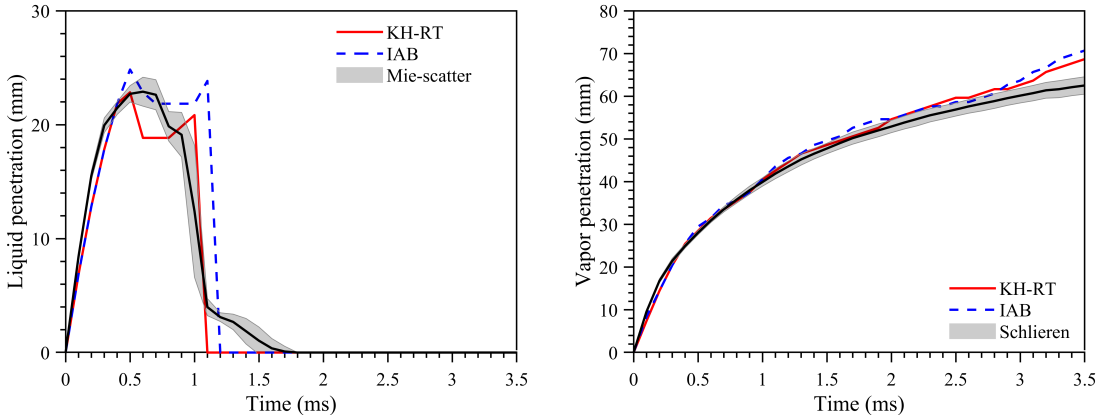

(a) Liquid-phase (b) Vapor-phase

Figure 5.12: Liquid- and vapor-phase penetrations for case 3 (GM DISI sprays at 800K, 6.0 kg/m^3). The experimental data are plotted with the shaded area representing the 95% confidence levels. Simulation results are from single-realizations.

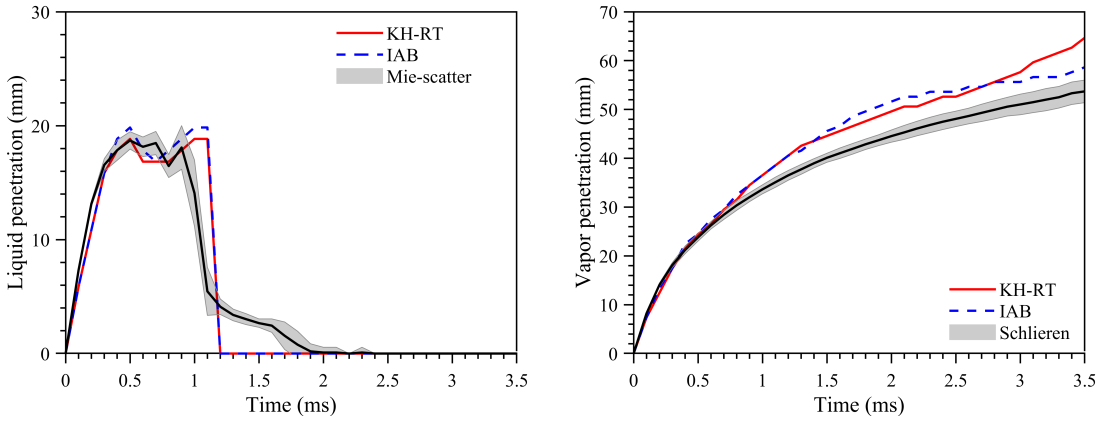

(a) Liquid-phase (b) Vapor-phase

Figure 5.13: Liquid- and vapor-phase penetration lengths for case 4 (GM DISI sprays at 800K, 9.0 kg/m^3). The experimental data are plotted with the shaded area representing the 95% confidence levels. Simulation results are from single-realizations.

quasi-steady state, the predicted droplet axial velocities show little differences and they both match the experimental data very well. However, the IAB model does show some improvements in terms of capturing the magnitude of the maximum droplet velocity. After the end of injection, the axial droplet velocities decrease with time and the spray plumes shift toward the injector centerline. Both simulation results match the measured data, as shown in sub-figures 5.14c - 5.14f. Small differences can be observed between simulations, especially at 1.3 and 1.5 ms ASOI.

Examining the SMD profiles in Figure 5.15, one can see that the simulation results extend to the outer edge of the spray plume before the end of injection, as shown in sub-figures 5.15a and 5.15b. The over-prediction of SMD distributions at the outer edge corresponds to a region of relatively large droplets with low speed. The maximum differences between measurements and simulations are about 6 and 30 μm for the IAB

and KH-RT models, respectively. Shortly after the end of injection, the predicted SMD distributions by the KH-RT model move closer to the measured data as shown in sub-figures 5.15c and 5.15d. The IAB model predicts a quasi-steady SMD distribution similar to the experimental data. At 1.3 and 1.5 ms ASOI, both models predict increased SMD, possibly due to the residual large droplets that just arrived from the near-nozzle region. A better representation compared to the experiments is given by the IAB model, especially at 1.5 ms ASOI. The reason for this improvement is that the droplet velocities are relatively low at 1.5 ms ASOI, leading most of the residual droplets into the bag and deformation breakup regimes, as will be discussed later. The bag sub-model is responsible for the breakup description of remaining "breaking" droplets (i.e., $We_l > We_{crit}$). The predicted droplet velocity and SMD distributions by the KH-RT model span further in the radial direction compared to the experimental data and the results by the IAB model, indicating that there are more residual droplets in the outer region of the spray.

IAB model characteristics

More insights into the IAB model can be gained by examining the occurrence percentage of each breakup sub-model (see Section 4.3) for cases 1 - 4. Results are reported against time in Figure 5.16, in which the occurrence percentage is defined as the ratio of the number of liquid parcels "evolving" by that sub-model to the total number of existing liquid parcels at that time. As the figure shows, a decrease in either the ambient temperature or ambient density will lead more parcels to have We numbers lower than We_{crit}. Therefore, they undergo oscillation/deformation. As the ambient temperature increases, the evaporation rate increases as well, which reduces the lifespan of small droplets and

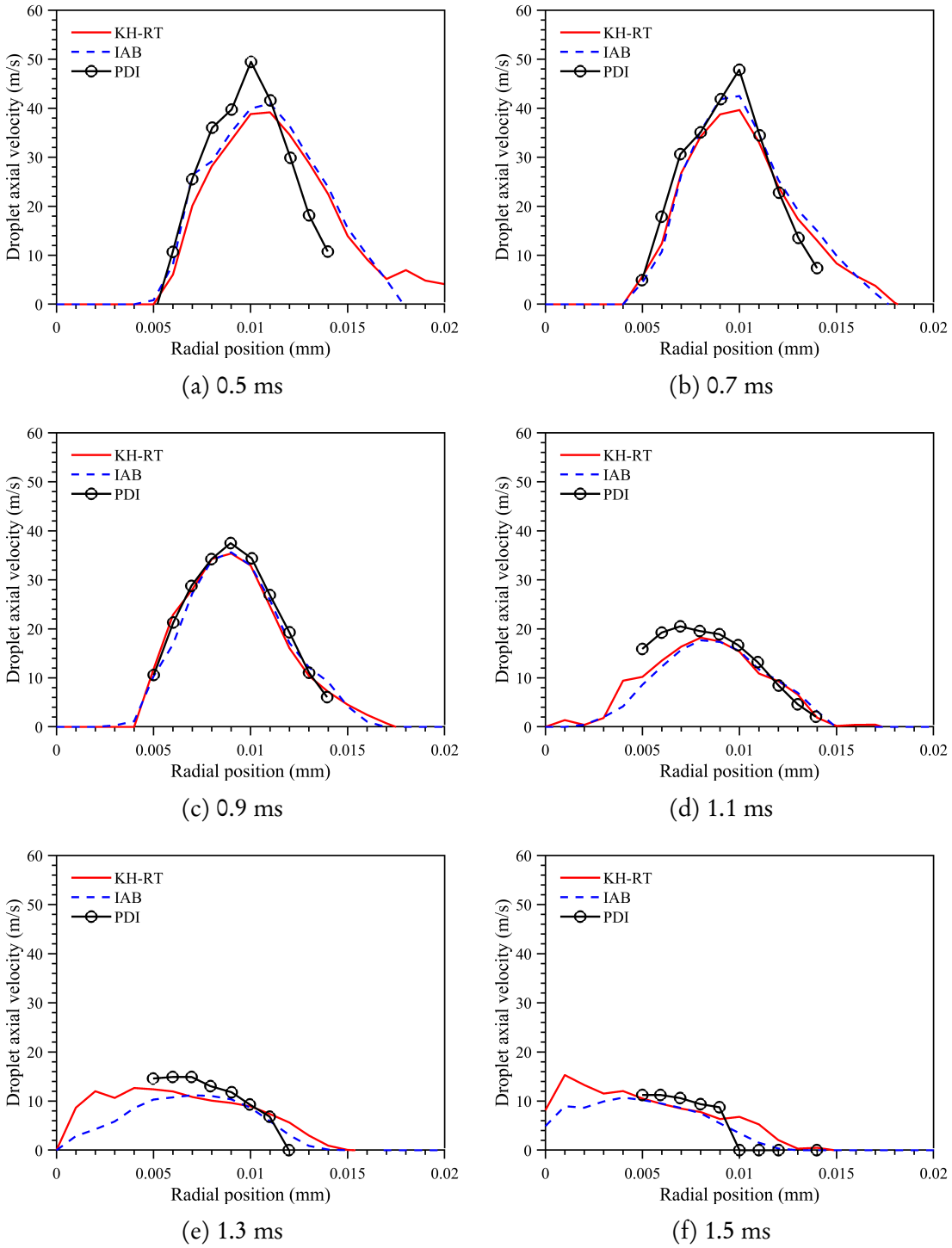

Figure 5.14: Plume-centered radial distribution of the axial droplet velocities for various selected times ASOI. Predicted results are ensemble-averaged over eight plumes and five realizations.

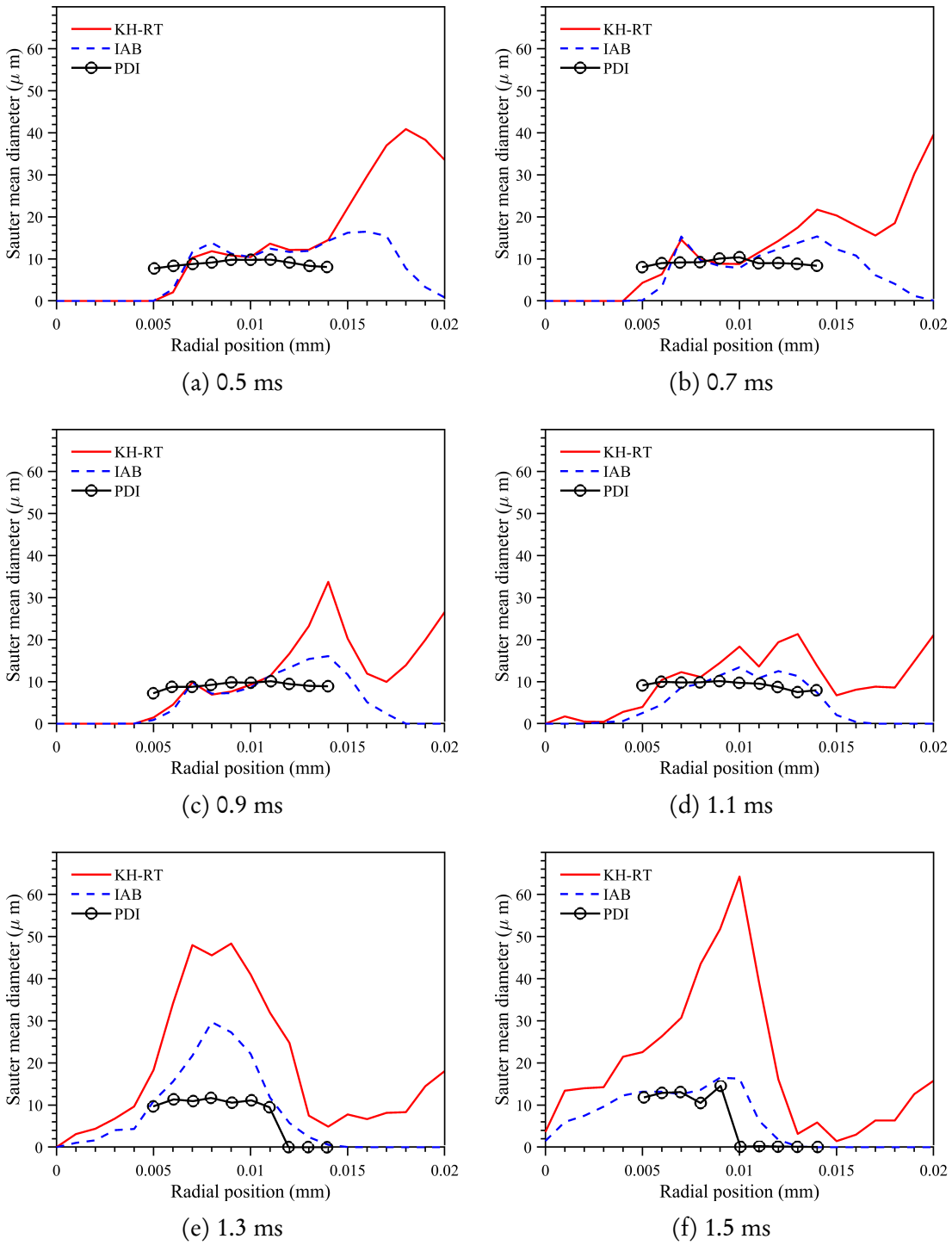

(a) 0.5 ms (b) 0.7 ms

(c) 0.9 ms (d) 1.1 ms

(e) 1.3 ms (f) 1.5 ms

Figure 5.15: Plume-centered radial distribution of the droplet SMD for various selected times ASOI. Predicted results are ensemble-averaged over eight plumes and five realizations.

hence the occurrence percentage of deformation mode. On the other hand, We number increases with the ambient density, leading to more droplets in the sheet-thinning or catastrophic breakup regimes.

Recall that the injection durations of Spray G and GM DISI sprays are 0.78 and 0.86 ms, respectively. In Figure 5.16, the occurrence percentages of the KH-RT sub-model are always larger than that of the bag sub-model before the injections end. The differences become more noticeable as the ambient density increases. After the end of injection, the bag sub-model begins to suppress the KH-RT sub-model and its occurrence percentage increases with time under high-temperature GM DISI spray conditions (i.e. case 2 - 4). This explains why the IAB model has better predictability in terms of capturing the liquid length and residence time of fuel droplets. For case 1, most of the liquid parcels undergo oscillation/deformation since the temperature is moderate. Bag/bag-stamen breakups are the leading mechanism of remaining parcels after the injection, which improves the predictions of the IAB model at 1.5 ms ASOI as shown in Figure 5.15f.

As discussed in Section 4.3, a "bi-modal" distribution is expected for bag breakup. However, the number of child droplets from bag rupture may overwhelmingly outnumber that from liquid torus breakup, hence discouraging this distribution to be observed in experiments [24, 81]. In simulations with the parcel approach, this limitation can be easily overcome if results are processed based on fuel parcels, as opposed to the velocities and SMD results discussed in Figures 5.14 and 5.15, which are processed based on fuel droplets. Recall that a parcel is a wrapper of several maybe hundreds of droplets with the same properties. In the bag breakup model, child droplets from the bag rupture and torus breakup are enclosed by two separate parcels. Figure 5.17 shows the PDFs of parcel

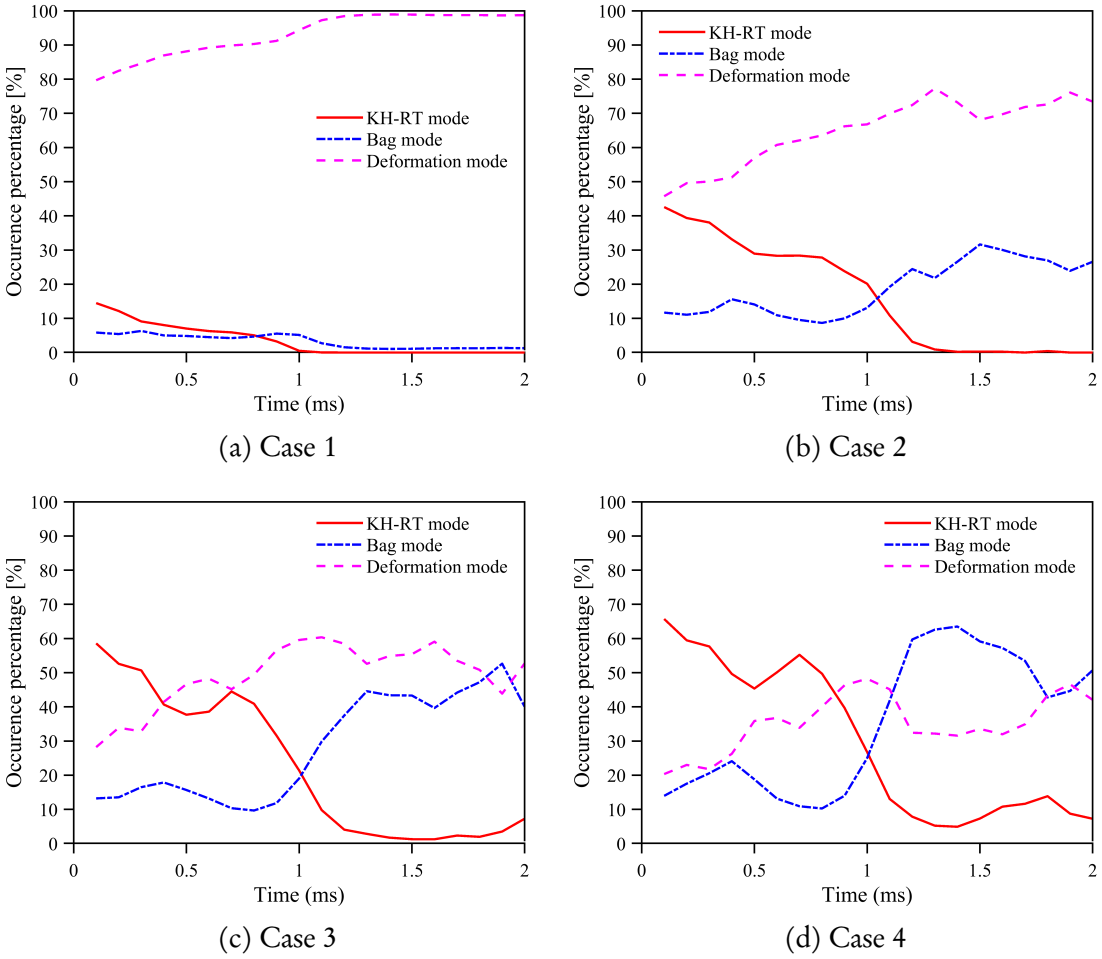

Figure 5.16: Occurrence percentage of the IAB breakup sub-models for test cases 1 - 4.

diameters at 1.1 ms ASOI for test cases 1 - 4. Results obtained using the IAB and KH-RT models are plotted on the left and right sub-figures, respectively. One can see that most residual parcels are smaller than 20 μm, and the peaks are located at around 10 μm. This corresponds to the deformation regime where parcels no longer break. Moving to larger parcels, a "bi-modal" distribution can be seen in results from the IAB model. The peaks in the middle correspond to the liquid torus rings after bag rupture, while the peaks on the right correspond to the growing bag. The micro-size parcels from bag rupture contribute to the left peaks. In Figure 5.17b, no such distribution can be observed.

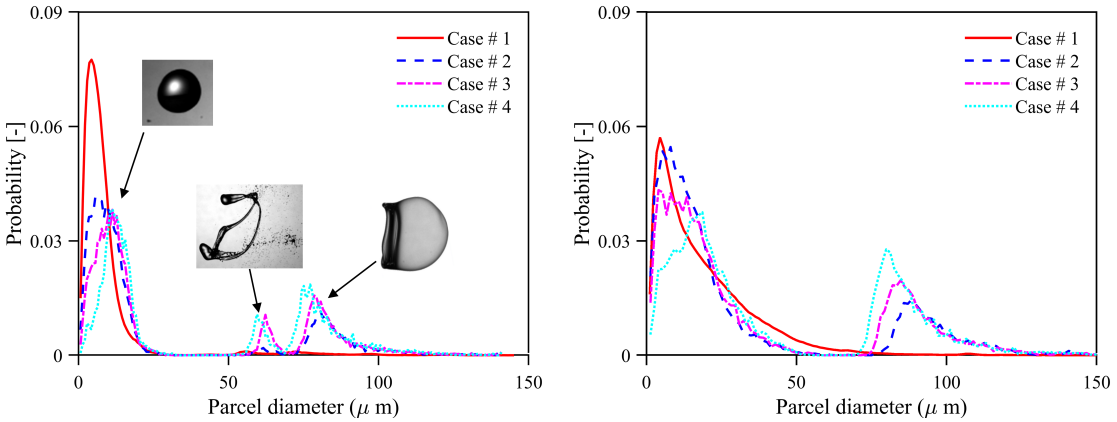

(a) IAB (b) KH-RT

Figure 5.17: PDF of parcel diameters at 1.1 ms ASOI for cases 1 - 4.

Moving to the PDFs of droplet diameters (i.e. PDF of parcel diameters weighted by the number of droplets per parcel), both models predict single mode PDFs as shown in Figure 5.18. The peaks shift to even smaller diameters compared to Figure 5.17, simply because micro-size parcels can contain hundreds of droplets owing to the extremely small droplet volume. As a result, those micro-size parcels carry much higher weights compared to larger parcels in the estimation of PDF. The differences among PDFs for

cases 1 - 4 predicted by the IAB model are smaller compared to the KHRT model, especially for case 2 which shows a much higher maximum around 3 μm.

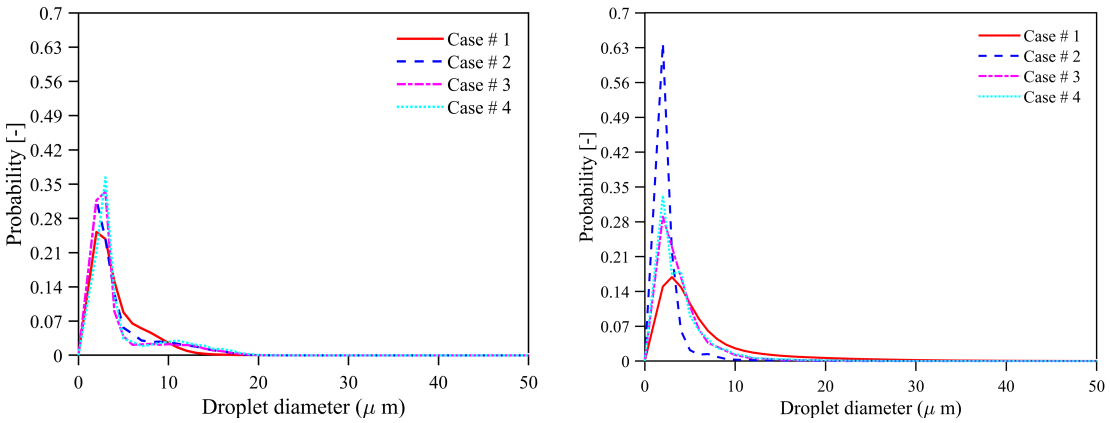

(a) IAB (b) KH-RT

Figure 5.18: PDF of droplet diameters at 1.1 ms ASOI for cases 1 - 4.

For additional insight into the models, Weber - Ohnesorge diagrams are analyzed by plotting scattered droplets in Figure 5.19 for case 1. In each sub-figure, liquid parcels in the computational domain are represented by solid circles with sizes proportionally to the parcel diameters and colors specified by the droplet velocity magnitudes. The breakup regimes of typical gasoline sprays presented in Figure 2.3 are also enclosed by boxed-region. Starting with Figure 5.19a, where results are presented at 0.7 ms ASOI, a timing when the spray reaches quasi-steady state. A considerable number of liquid parcels with We numbers as large as 4000 can be observed with both models. Results from the KH-RT model also show some large blue circles on the bottom left side of Figure5.19b. These correspond to large droplets with relatively small velocity magnitudes resulting from the one-time droplet enlargement process in the KH breakup modeling. Results from the IAB model, on the other hand, do not show such behavior even though the one-

time enlargement is also implemented. Note that most of the liquid parcels are located in the bag and deformation breakup regimes, as evidenced by Figure 5.16a. Figures 5.19c and 5.19f indicate that the residual droplets after the end of injection are breaking by the multi-mode and bag breakup mechanisms since the droplet We numbers range from 0 to 110. The small We numbers are primarily caused by low droplet velocity magnitudes, rather than from small droplet sizes. Overall, the Weber - Ohnesorge diagrams support the findings in Figure 5.16. In addition, one can argue that the residual droplets after the end of injection are having both a small number and a small mass in simulations with the IAB model, as evidenced by the lower SMD in Figure 5.15 and smaller regions in Figures 5.19c and 5.19f.

Application to more DISI spray conditions

More evaluations of the IAB model are done by extending the test matrix to all ambient conditions for GM DISI sprays. Instead of providing the "best practice" results as discussed in the previous section, an effort to unify the model parameter values and to reduce the need to calibrate the model across various conditions is made. Table 5.8 lists the “best practice” parameter values of the IAB model for cases 1 - 4. Note that C_β values for the density conditions listed in Table 5.8 are close to each other. Assuming the value of C_β is a constant for DISI sprays with a specific type of fuel, then a reasonable estimation can be made by averaging the C_β values in Table 5.8. On the other hand, the breakup time constant, B_1, appears to be highly dependent on the turbulent internal flow (and hence the injector geometry). Therefore, no effort is made to correlate B_1 with ambient conditions.

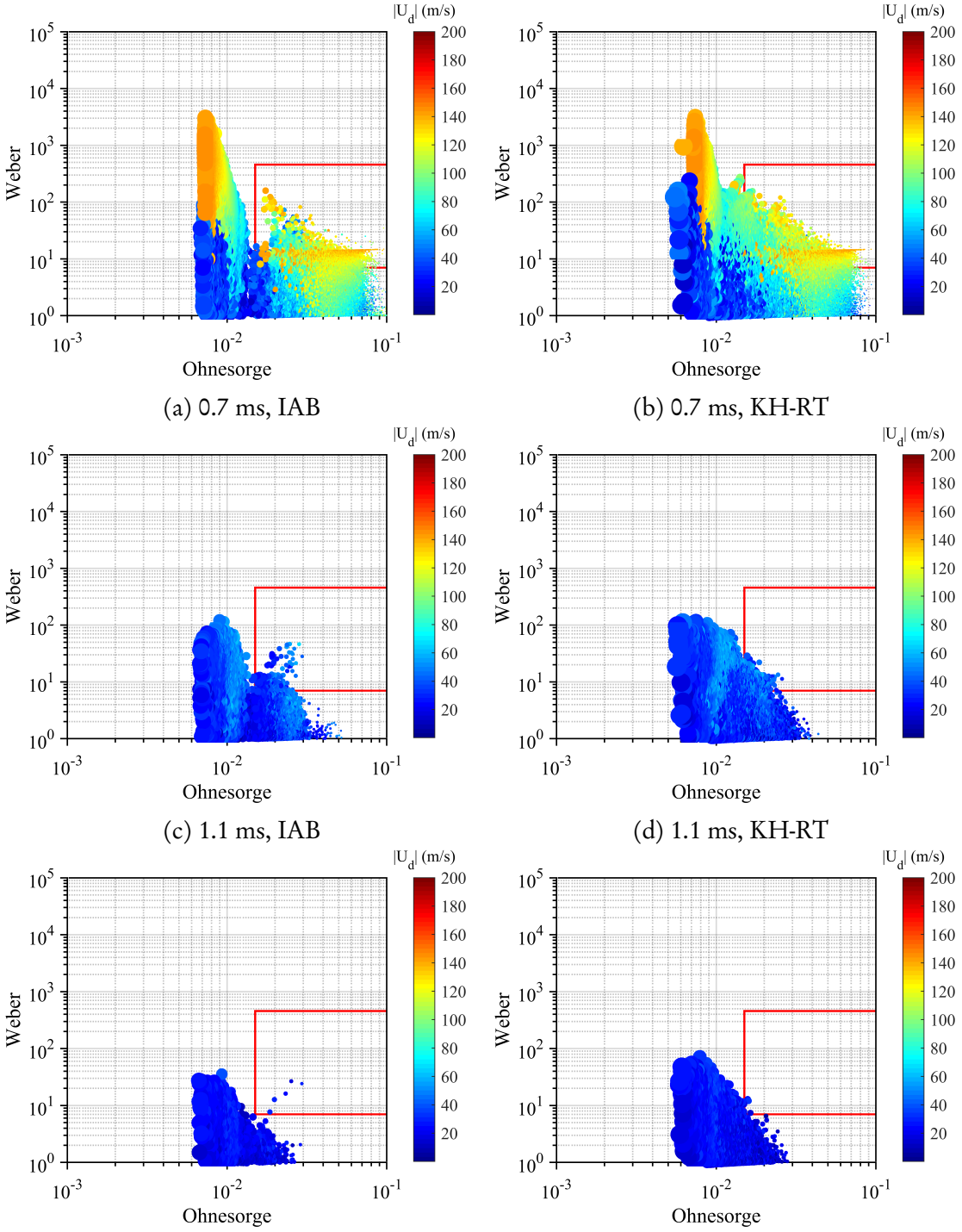

Figure 5.19: Weber-Ohnesorge diagrams for case 1 predicted by both IAB and KH-RT models. In each sub-figure, the scattered droplets are plotted as solid circles with sizes proportionally to the droplet diameter, and colors specified by the magnitudes of droplet velocities. The red boxed-region indicates the typical gasoline spray breakup regimes identified in Ref. [25].

Table 5.8: “Best practice” parameter values for the IAB and KH-RT models for cases 1 - 4.

-	-	Case 1	Case 2	Case 3	Case 4
Ambient density (kg/m^3)	-	3.5	3	6	9
Ambient temperature (K)	-	573	800	800	800
IAB	C_β in Equation 4.45	0.92	0.89	0.93	0.93
	B_1 in Equation 4.41	30	50	50	50
KH-RT	B_1 in Equation 4.41	30	50	50	50
	C_b in Equation 4.44	1	1.9	2	2.3
	C_{RT} in Equation 4.43	0.35	0.1	0.1	0.1

The model parameter values for the “best practice” KH-RT results discussed in the previous section are also listed in Table 5.8. Note that three parameters have to be tuned in order to obtain the optimal results, as opposed to the IAB model, which only needs two. Breakup lengths along the plume axis for cases 1 - 4 are calculated for both models using parameter values listed in Table 5.8. Results are plotted as dashed lines and dash-dotted lines in Figure 5.20. The estimated breakup lengths for cases 2 – 4 from the study of Van Dam [91] are also plotted as dotted lines for comparison purposes. Note that as the ambient density increases, the liquid-gas density ratio decreases, resulting in a reduced breakup length estimated by the IAB model. This result accords well with the expectation that higher ambient density promotes faster breakup and reduced breakup length. On the other hand, the breakup lengths estimated by the KH-RT model exabit very different trends between this work and Ref. [91]. Van Dam estimated the breakup length to increase as the density ratio decreases, while in this work the breakup length shows a more complex behavior with a local minimum in case 1.

Figures 5.21 and 5.22 show the liquid- and vapor-phase penetrations for all GM DISI

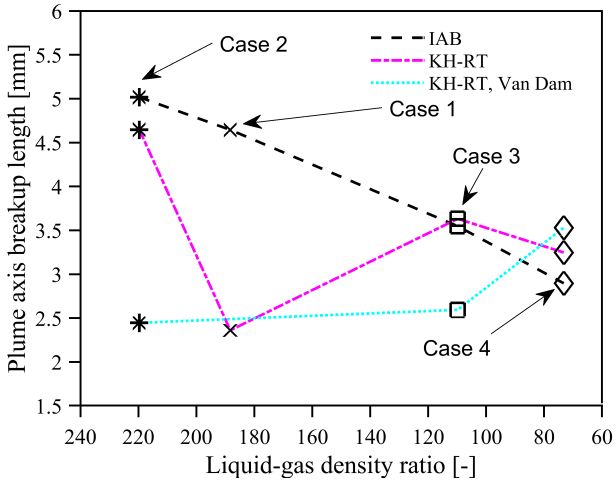

Figure 5.20: Nominal breakup length along the plum axis predicted by Equation 4.45 using $C_\beta = 0.92$ for cases 1 - 4. Also plotted are results estimated using the KH-RT model with "best practice" parameter values listed in Table 5.8 and from the work of Van Dam [91]. On each curve, the density ratios corresponding to cases 1 – 4 are overlaid with asterisks, crosses, squares, and diamonds, respectively.

temperature and density conditions (as illustrated in Figure 5.4). Simulation results are taken from single-realizations with the IAB model parameters $C_\beta = 0.92$ and $B_1 = 50$. Experimental data are the average of 25 duplicate measurements. The left columns show the liquid-phase penetrations, and the right ones show the vapor-phase penetrations. The top rows show results at 3.0 kg/m^3, and the following two rows show the results at 6.0 and 9.0 kg/m^3, respectively. In each sub-figure, experimental data are only plotted with the mean values for clarity purpose.

A general trend found in Figures 5.21 and 5.22 is that higher ambient density promotes reduced liquid length. The reduction at higher density is due to enhanced air entrainment, increased aerodynamic drag, and faster droplet breakup. In Figure 5.21, the density impact is more significant at 400 K compared to 500 K and higher. The liquid

residence time also shows the largest difference at 400 K, in which an increase in the ambient density will lead to longer liquid residence time. The simulations are able to reproduce the shape of the experimental curve at 3.0 kg/m^3 but fail to even capture the general trends at higher densities for the ambient temperature of 400 K. One possible explanation for this behavior could be attributed to the low temperature and high pressures, which may lead to a suppressed turbulent internal flow. Therefore, setting B_1 to be 50 will over-estimate the breakup speed. The comparison is more favorable at elevated temperatures and reduced densities, where both the liquid length and residence time are well predicted. In Figure 5.22, the predicted liquid penetrations match the experimental data reasonably well with the exception of 900 K at 6.0 and 9.0 kg/m^3, where the penetrations are over-predicted. Despite the magnitudes of liquid penetrations being off at these two conditions, the trend and the liquid residence time are still well captured.

The predicted vapor penetration curves in Figure 5.21 agree reasonably well with the Schlieren measurements. At 400 K, the vapor penetration results are under-predicted throughout the injection event at all three density conditions. One possible reason is the identical spray initial and boundary conditions at the nozzle exit for each density condition. While in reality the ambient temperature and pressure influence the spray behaviors such as the plume cone angle and injection velocity, in simulations they are kept as constants at each density conditions since the primary goal of this test is to see if the IAB model can perform well under conditions beyond the scope of cases 1 - 4. In Figure 5.22 at 800 K, the predicted vapor-phase penetrations match the experimental data quite well at 3.0 and 6.0 kg/m^3 even though they are not the "best practice" results. At 9.0 kg/m^3, the predicted vapor penetration results are somewhat discouraging. One possible

reason is the extra momentum gained from the over-penetrating liquid droplets as shown in the left columns. Considering the fact that the total simulation time is about four times larger than the injection duration, other factors including the turbulence model can come into play.

The liquid length and liquid residence time are two important macroscopic spray characteristics in DISI sprays. In general, the liquid length needs to be accurately captured since it affects the wall-impingement and hence the following mixing and combustion processes. The liquid residence time is also of importance as residual droplets can be a potential source of soot. Therefore, a comparison of these two quantities are extracted from Figures 5.21 and 5.22 and plotted in Figure 5.23. While the calculation of liquid length is straightforward, the definition of liquid residence time is somewhat vague. In experiments, the liquid residence time is defined as the time required for the penetration to fall to half the maximum due to evaporation [80]. In simulations, however, the residence time is defined as the time when the liquid penetration falls to zero. The difference caused by this discrepancy is expected to be negligible providing the liquid penetration falls rapidly back to zero in the simulations.

In Figure 5.23a, the predicted liquid length results are plotted as functions of ambient temperature for the three ambient densities. Experimental data from the Mie-scatter imaging are also plotted as symbols at each corresponding condition. It can be seen that the predictions match the experimental data very well at 3.0 kg/m^3. At 6.0 kg/m^3, the agreement is quite good as well except for 400 and 900K, where successful predictions are not achieved. At 9.0 kg/m^3, the simulation results only match the experimental data at 700 and 800 K. However, the general trend of reduced liquid length with increasing

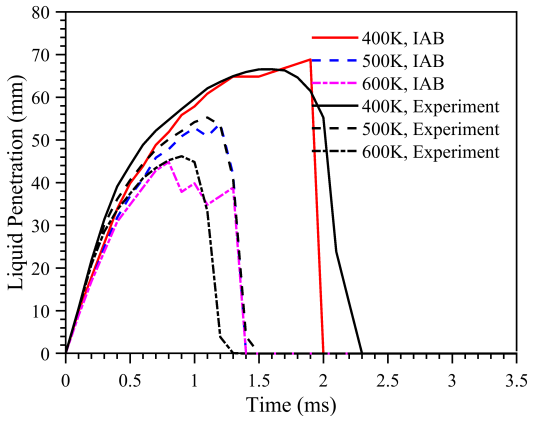

(a) Liquid-phase, ρ_g = 3.0 kg/m^3

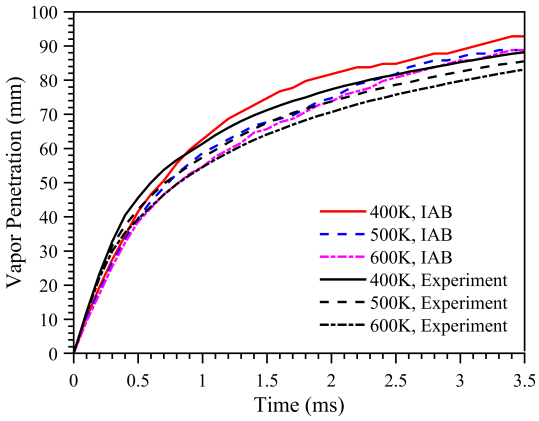

(b) Vapor-phase, ρ_g = 3.0 kg/m^3

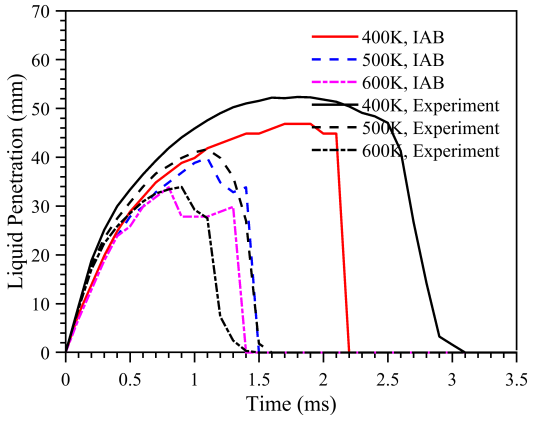

(c) Liquid-phase, ρ_g = 6.0 kg/m^3

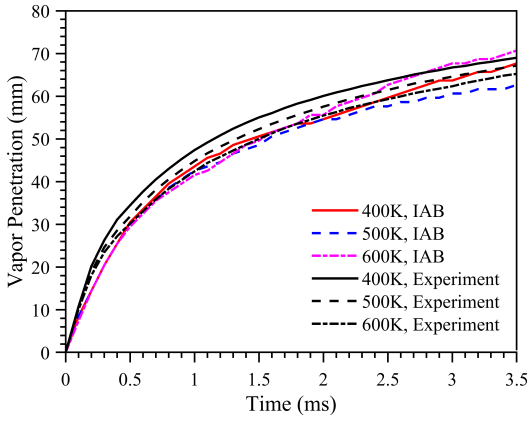

(d) Vapor-phase, ρ_g = 6.0 kg/m^3

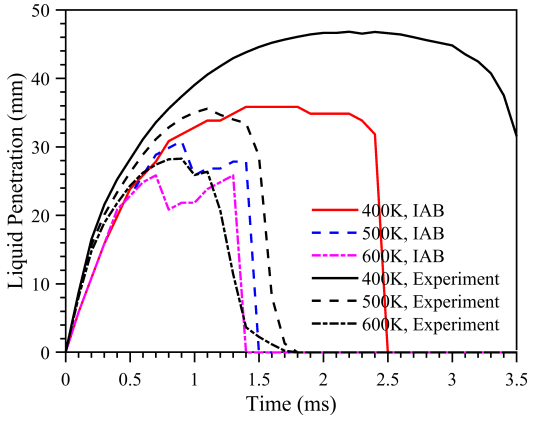

(e) Liquid-phase, ρ_g = 9.0 kg/m^3

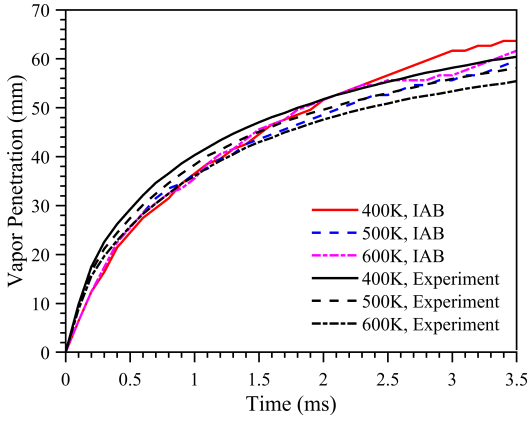

(f) Vapor-phase, ρ_g = 9.0 kg/m^3

Figure 5.21: Comparison of penetration curves between simulations and experiments at GM DISI spray conditions of 400 – 600 K. Experimental results are averaged over 25 measurements. Simulations results are taken from single-realizations.

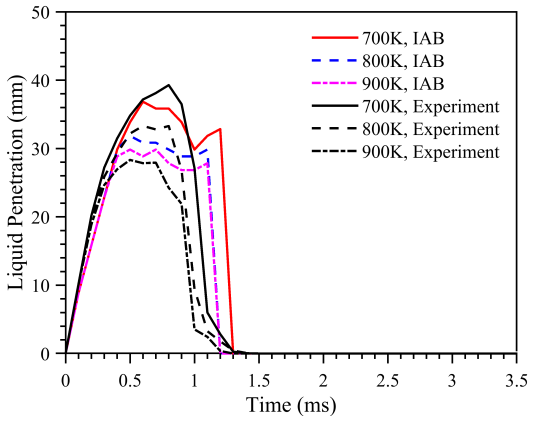

(a) Liquid-phase, ρ_g = 3.0 kg/m^3

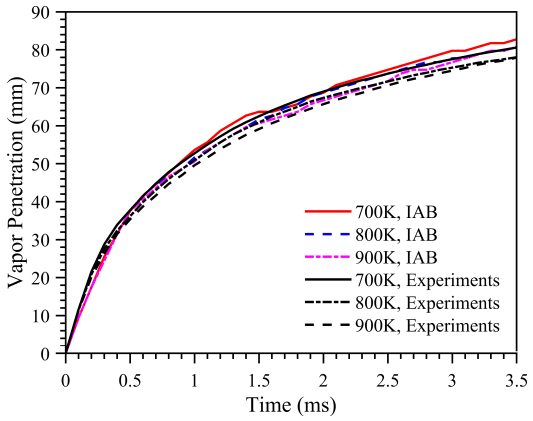

(b) Vapor-phase, ρ_g = 3.0 kg/m^3

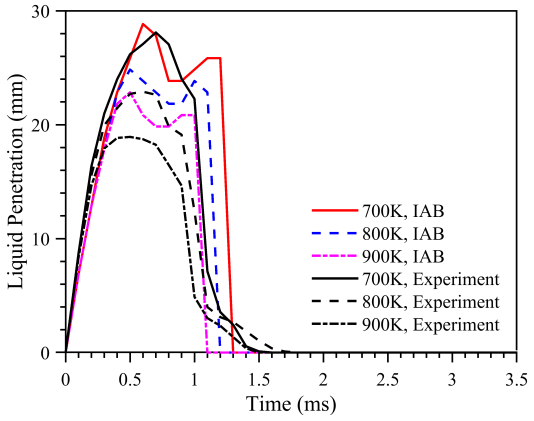

(c) Liquid-phase, ρ_g = 6.0 kg/m^3

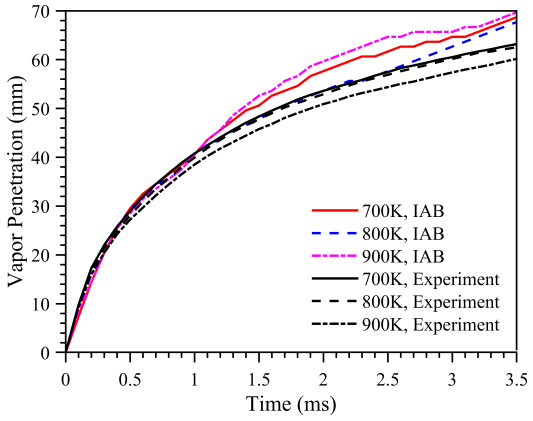

(d) Vapor-phase, ρ_g = 6.0 kg/m^3

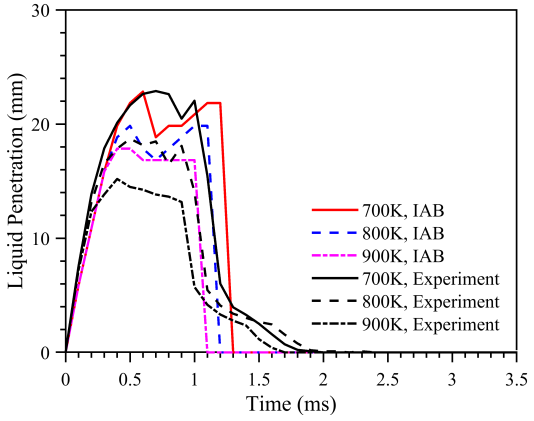

(e) Liquid-phase, ρ_g = 9.0 kg/m^3

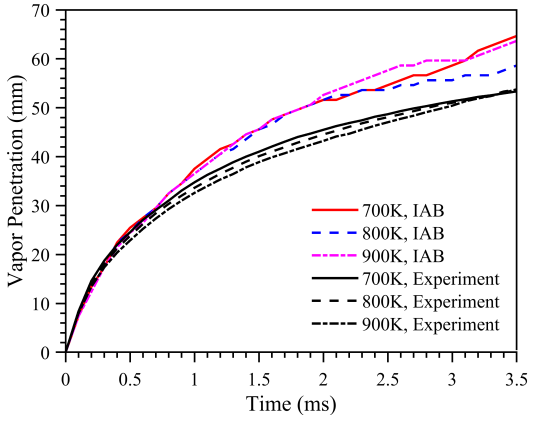

(f) Vapor-phase, ρ_g = 9.0 kg/m^3

Figure 5.22: Comparison of penetration curves between simulations and experiments at GM DISI spray conditions of 700 – 900 K. Experimental results are averaged over 25 measurements. Simulations results are taken from single-realizations.

ambient temperature is still captured by the model.

The results of liquid residence time are shown in Figure 5.23b. First, it can be seen that the liquid residence times show little differences among different densities at the temperatures of 500 K and higher. At the lowest temperature of 400 K, however, the liquid residence time increases aggressively as the ambient density increases. The model fails to capture the experimental trend at this temperature point but is able to give satisfactory predictions at other temperature conditions.

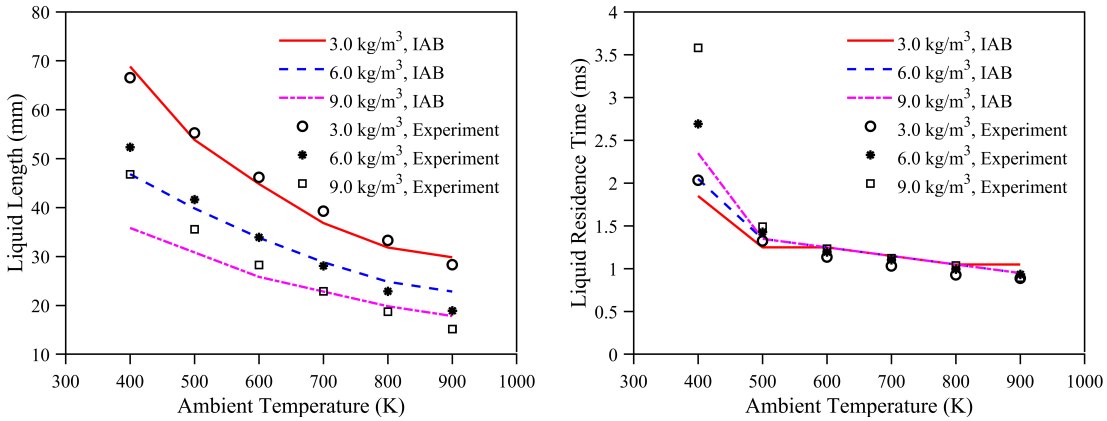

(a) Liquid length (b) Liquid residence time

Figure 5.23: Liquid length and liquid residence time as a function of ambient temperature. Symbols represent the measured data from Mie-scatter imaging. The continuous curves represent predicted results using the IAB model.

Uncertainty Quantification

A UQ study is conducted for case 3 to assess the effects of spray boundary conditions and model parameters on the predicted spray characteristics by the IAB model [83]. Four uncertain variables, namely, the transition Weber number, We_{bag}, bag rupture time constant, τ_{bag}, area contraction coefficient, C_A, and spray cone angle (i.e., plume direction

$\times$ 2), are selected for the UQ study. These variables are chosen based on a previous UQ study of Van Dam and Rutland [108] and personal experience. Recall that the transition Weber number and bag rupture time constant are model parameters of the IAB breakup model. The transition Weber number controls which sub-model is activated for a spray parcel. The bag rupture time constant controls when the bag-shaped droplet breaks into small droplets and a liquid torus ring. Table 5.9 lists the four uncertain variables along with their lower and upper bounds, which are set based on various previous studies on spray breakup mechanisms [16, 20, 23, 109], experimental work [90, 110], and other UQ-related studies [91, 108, 111]. Uniform distributions are assumed for all variables since the actual PDFs are unknown.

The Dakota toolkit developed at SNL is used to perform the UQ study. Dakota offers many UQ methods that specifically focus on the forward propagation of input uncertainties on model outputs, where probabilistic or interval information on parametric inputs is mapped through the computational model to assess statistics or intervals on outputs [112]. A non-intrusive approach is used to couple Dakota to OpenFOAM. In this approach, Dakota generates sets of input samples based on the probability distributions of uncertain variables. Then multiple instances of OpenFOAM simulations are launched simultaneously by Dakota each with one set of the input samples. After all the OpenFOAM simulations are finished, Dakota takes the response functions, i.e., simulation outputs of interest, and performs the final analysis.

Two probabilistic UQ methods, namely statistical Latin-hypercube sampling (LHS) and non-statistical Polynomial chaos expansion (PCE), are used to understand how variations in the uncertain variables affect spray characteristics such as liquid- and vapor-phase

penetrations, and spray probability contours. Statistical analysis of the interactions between uncertain variables and spray characteristics is also performed. An overview of the UQ methods and the statistics are provided in Appendix A. For the PCE method, second level orthogonal polynomial approximation (Smolyak sparse grids) is used requiring 49 simulations. The truncated polynomial chaos expansions include 45 terms, using polynomials up to fifth order. Fifty simulations were used for LHS to achieve a balance between efficiency and accuracy [91].

Table 5.9: Uncertain variables for the UQ of case 3. Nominal values are listed for reference only.

Uncertain variable	**Lower bound**	**Nominal**	**Upper bound**
Transition We, We_{bag} (-)	20	40	60
Bag rupture time constant, τ_{bag} (-)	0.75	0.9	1.05
Area contraction coefficient, C_A (-)	0.73	0.78	0.83
Spray cone angle (°)	45	50	55

Figure 5.24 shows the mean penetration curves from experiments, LHS, and PCE. The standard deviations from simulations and experiments are also plotted for the liquid-phase penetrations. Similar to the findings in Figure 5.22c and 5.22d, the predicted mean follows the measured data very well. Focusing on the standard deviations of liquid-phase, which are extracted from Figure 5.24 and plotted with asterisks in Figure 5.25, show very similar trends until the end of injection. All three curves show a spike between 1.0 and 1.3 ms ASOI, which is the time interval when the spray becomes fully vaporized. The spike appears due to different timings of the transition to fully vaporized spray, i.e., some experiments/simulations vaporize faster, thus give zero penetrations at earlier times, while others vaporize slower and predict zero penetrations at later times. Both

LHS and PCE show a delayed timing of the spike compared to the experiments. A possible reason for this delay is the presence of large droplets. Besides, PCE shows a much higher spike compared to LHS and experiments, while the latter two are almost identical to each other. A possible explanation is, during the spectral projection or assembly of PCE, a step change of response liquid-phase penetration may not be well modeled by polynomials. The step change may also violate the smoothness assumptions that are used in deriving the accuracy estimates for the Smolyak sparse grids method, as mentioned in Ref. [91].

Moving to the standard deviations of vapor-phase penetrations plotted in Figure 5.25, we can see that LHS results and experimental data grow with time and follow each other closely, while PCE gives larger variations at later times. To explain this, a feature of LES should be outlined first. In LES, the filtered flow field responds to the non-linearities in the Navier-stokes equation, and consequently, uncertainties in initial and boundary conditions will have a bigger impact on flow structures as the simulation proceeds. As mentioned before, PCE derives UQ statistics analytically based on the preselected sample space. Among all the simulation samples, the outer vapor bound would show larger variations at later times. This variation can be enhanced during the spectral projection or PCE assembly process, resulting in higher standard deviations. Expanding the sample space or increasing the number of polynomials in PCE may help but no definite conclusion can be drawn before a further study is conducted.

Partial correlation coefficients between uncertain variables and response functions are plotted in Figure 5.26. The correlation coefficients range from +1 to -1. A value of +1 implies a positive linear relationship between two variables. A value of -1 implies a

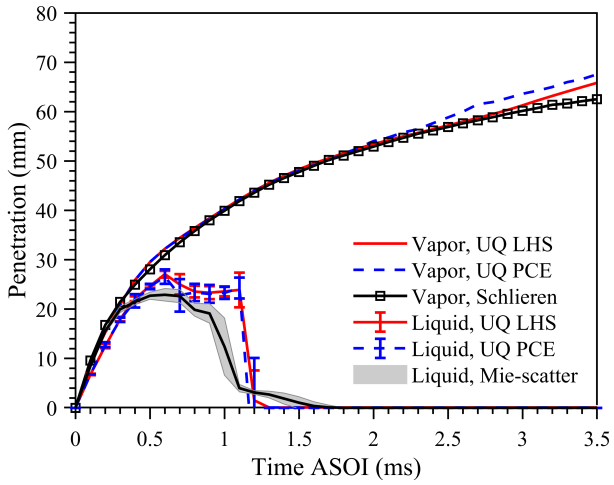

Figure 5.24: Mean penetration curves for case 3 from LHS (solid line), PCE (dashed line), and experiments (symbols). Liquid-phase penetrations are plotted with its one-standard-deviation as the upper and lower limits from the mean. Vapor-phase penetrations are plotted with the mean only.

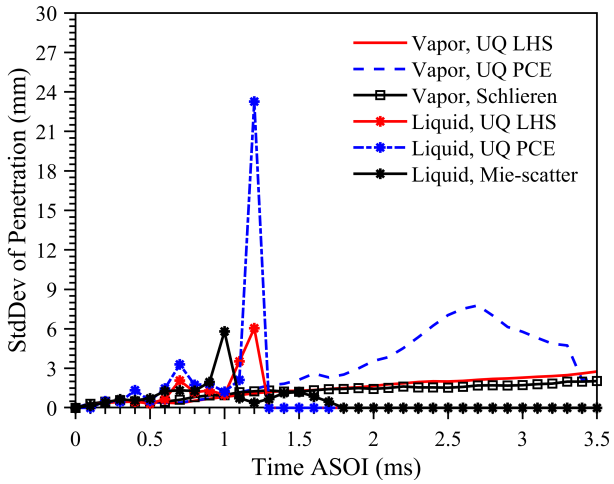

Figure 5.25: Standard deviations of penetration rates for case 3 from LHS (dashed line), PCE (dotted line), and experiments (solid line). Standard deviations of liquid-phase penetration are plotted with asterisks. Standard deviations of vapor-phase penetrations are plotted with squares.

negative linear relationship. A value of zero implies that there is no linear correlation between the variables. Begin with the liquid length, which shows nonlinear correlations with all uncertain variables. Note that a larger We_{bag} would lead to more parcels being modeled using the bag breakup sub-model, which results in smaller liquid length since the breakup prediction of low-speed droplets is accelerated. Therefore, the negative correlation between We_{bag} and liquid length in Figure 5.26 appears justified. The bag rupture time constant, τ_{bag}, is positively correlated with liquid length because larger τ_{bag} would allow droplets to travel further downstream before the breakup. As for the area contraction coefficient, the negative correlation is expected since the breakup time scales increase with increasing area contraction. From a geometric point of view, a larger spray cone angle should give smaller liquid penetration along the nozzle axis. However, it also leads to more thinly dispersed droplets in the computational domain. One can imagine that in a nearly quiescent vessel, scattered droplets in the near-nozzle region would be less likely to induce intensive turbulent gas flow, which may allow some droplets to penetrate further downstream before becoming fully vaporized.

The correlation coefficients between two model parameters and vapor-phase penetration at 0.5 ms ASOI indicate that faster breakup would result in higher vapor-phase penetration. After 1.3 ms (when liquid-phase penetration goes to zero), vapor-phase penetration has very weak linear correlations with these two parameters as demonstrated by the corresponding correlation coefficients at 1.5, 2.5, and 3.5 ms ASOI. Both spray boundary conditions are negatively correlated with vapor-phase penetration throughout the simulation because an increase in either one is matched by a decrease in droplet breakup speed and axial ambient velocity, respectively.

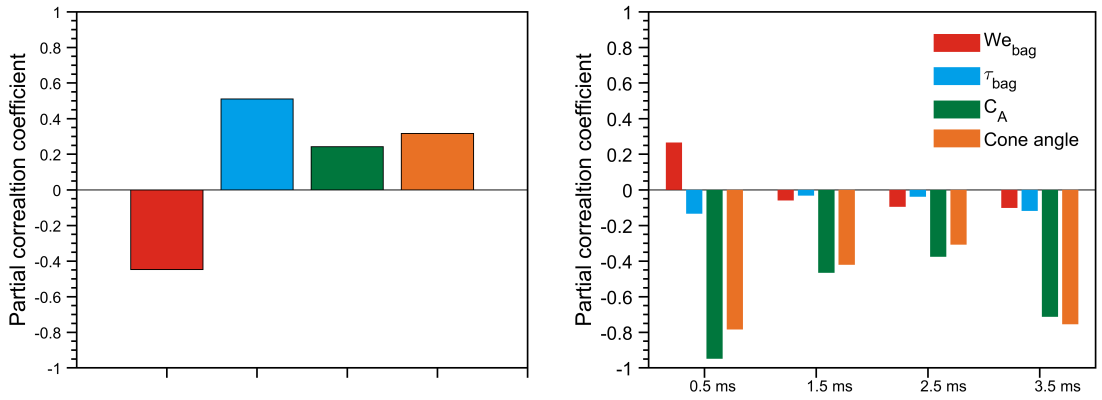

(a) Liquid length (b) Vapor-phase penetration

Figure 5.26: Partial correlation coefficients between four uncertain variables and five response functions for case 3. Four instantaneous vapor-phase penetrations at t = 0.5 ms, 1.5 ms, 2.5 ms, and 3.5 ms are chosen as response functions.

Sobol's main effect indices from PCE are shown in Figure 5.27. The main effect sensitivity index corresponds to contribution to the output variance by varying an uncertain variable alone. As demonstrated by the first group on the left, We_{bag} has the biggest impact on liquid length, followed by the spray cone angle and area contraction coefficient. The bag rupture time constant has the least impact compared to the other three. On the other hand, We_{bag} appears to have a much smaller impact on vapor-phase penetrations compared to area contraction coefficient and spray cone angle. Combining this with penetration curves in Figure 5.30 supports the idea that vapor-phase penetration at early times is strongly dependent on the injection speed. This further suggests that instead of taking area-contraction coefficient as a constant throughout the simulation, accurate description of its value as a function of time is needed for realistic prediction of liquid mass and momentum flow rates.

Another interesting finding from Figure 5.27 is that the effects of area contraction coefficient are much smaller at later times (1.5, 2.5, and 3.5 ms ASOI) as depicted by the right three groups. This is reasonable since no contribution to the vapor field will be made through phase-change after 1.3 ms ASOI. However, the spray cone angle appears to become more important at later times. One may notice that the effects of model parameters at 2.5 ms ASOI seem to be comparable to that of spray boundary conditions. A possible explanation is that impact of model parameters on spray breakup propagates and make the corresponding vapor field show more variations at later times. Numerical noises in PCE can also contribute to this. Nevertheless, the general findings from Figure 5.27 stand valid.

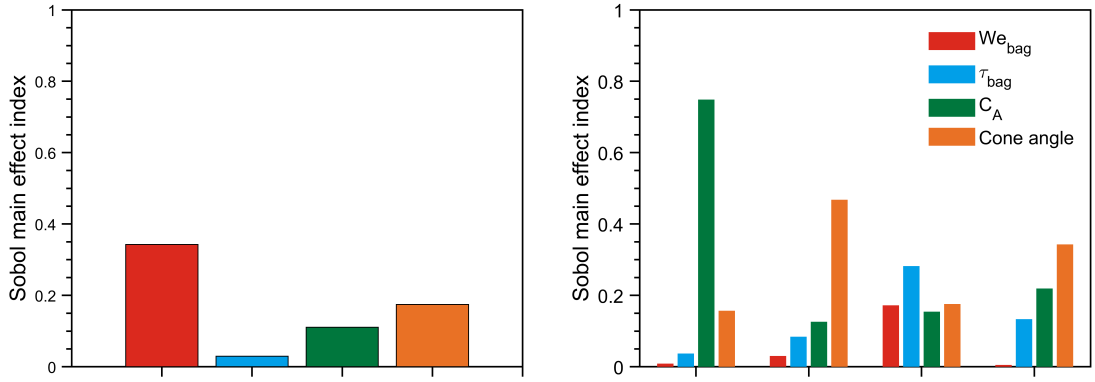

(a) Liquid length

(b) Vapor-phase penetration

Figure 5.27: Sobol's main effect indices for case 3. Each bar represents a contribution to the variance in one of the response functions by varying one specific uncertain variable. Four vapor-phase penetrations at t = 0.5 ms, 1.5 ms, 2.5 ms, and 3.5 ms are chosen as response functions.

Further analysis of the liquid- and vapor-phase contours can provide more insights into the variations from injection to injection. Figure 5.28 shows liquid probability con-

tours at four selected times. These probability contours are derived by mapping the two-dimensional array of integrated surface area for each simulation and then computing the probability of each array element that would exceed the detectability limit.

The contours in Figure 5.28 show the probabilities of finding a liquid region that has the same size as indicated by colored iso-lines. For example, there is a 95% chance of producing a liquid region that has the same size as the region enclosed by red color, while there is a 5% chance of producing a liquid region that has the same size as the region enclosed by blue color. The contours from experiments, LHS, and PCE show similar patterns at 0.1, 0.3, and 0.7 ms ASOI as shown in the first three rows. Four pairs of spray plumes, each having two plumes (one behind the other) are more discernible in simulations. However, the experimental iso-lines are very tightly spaced, appearing as a very thin color band along the perimeter of the spray. This observation suggests that there may be strong plume-to-plume interactions in the experiments that are not well reproduced by current LES models. The absence of a proper injection model that considers nozzle geometric effects, internal turbulence, or even cavitation may be another reason why simulations show more visible plume-to-plume boundaries. The last row in Figure 5.28 shows that there are some scattered droplets existing at approximately 20 mm below the nozzle tip in both LHS and PCE. In experiments, however, only a small amount of liquid fuel persists near the nozzle tip.

Vapor probability contours are derived using the similar method to liquid, but the detectability was set as 0.1% mixture fraction. As shown in Figure 5.29, the overall agreement between UQ methods and experiments is good at selected times. In contrast to liquid probability contours where individual spray plumes are discernible, the vapor prob-

ability contours exhibit a broadening of each plume thus no plume-to-plume boundary can be seen. Left and middle columns of Figure 5.29 also show an excellent agreement between experiments and LHS in terms of the thickness of each contour. On the other hand, PCE shows much more variations at 1.5, 2.5, and 3.5 ms ASOI. This may be due to numerical errors introduced during the spectral projection or PCE assembly.

One may also notice that the neck of each vapor probability contour from LHS and PCE is much wider compared to experimental data. One possible reason is the introducing of artificial viscosity to the dynamic structure turbulence model. While giving good results for high-pressure diesel sprays as stated in Ref. [75], the artificial viscosity may introduce too much diffusion in the near-nozzle region for gasoline sprays that utilize much lower injection pressure. This can be explored in future UQ study involving turbulence models. As for LHS and PCE, the primary difference between these two methods is the smoothness of iso-lines and width of contour bands. LHS has relatively smooth contours like the experiments, while PCE shows more variations, especially in the inner region.

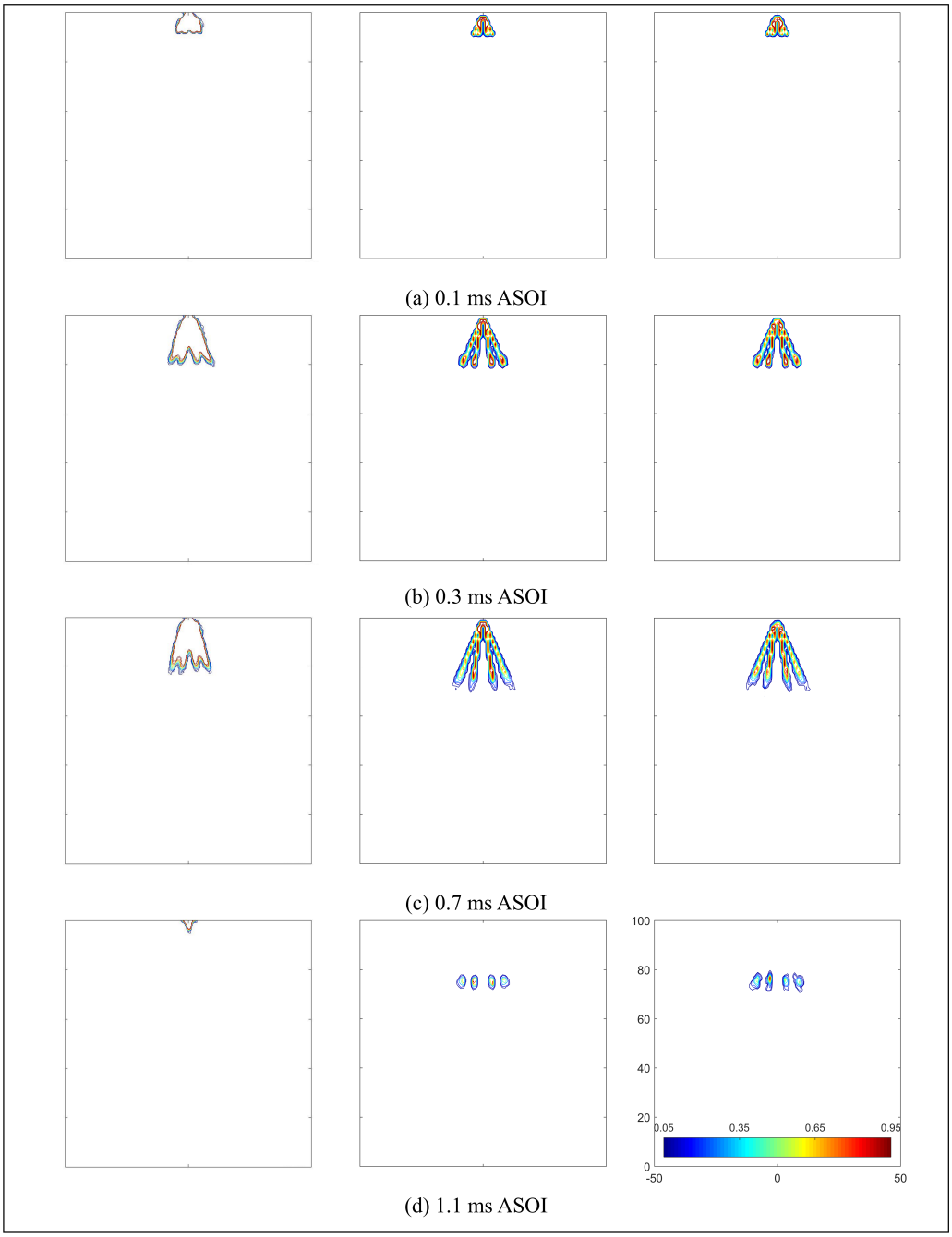

Figure 5.28: Liquid probability contours for case 3 at various times from experiments (left column), LHS (middle column), and PCE (right column). For each contour, there is a 95% chance of producing a liquid region that has the same size as indicated by the innermost region, and a 5% chance of producing a liquid region that has the same size as indicated by the outermost region.

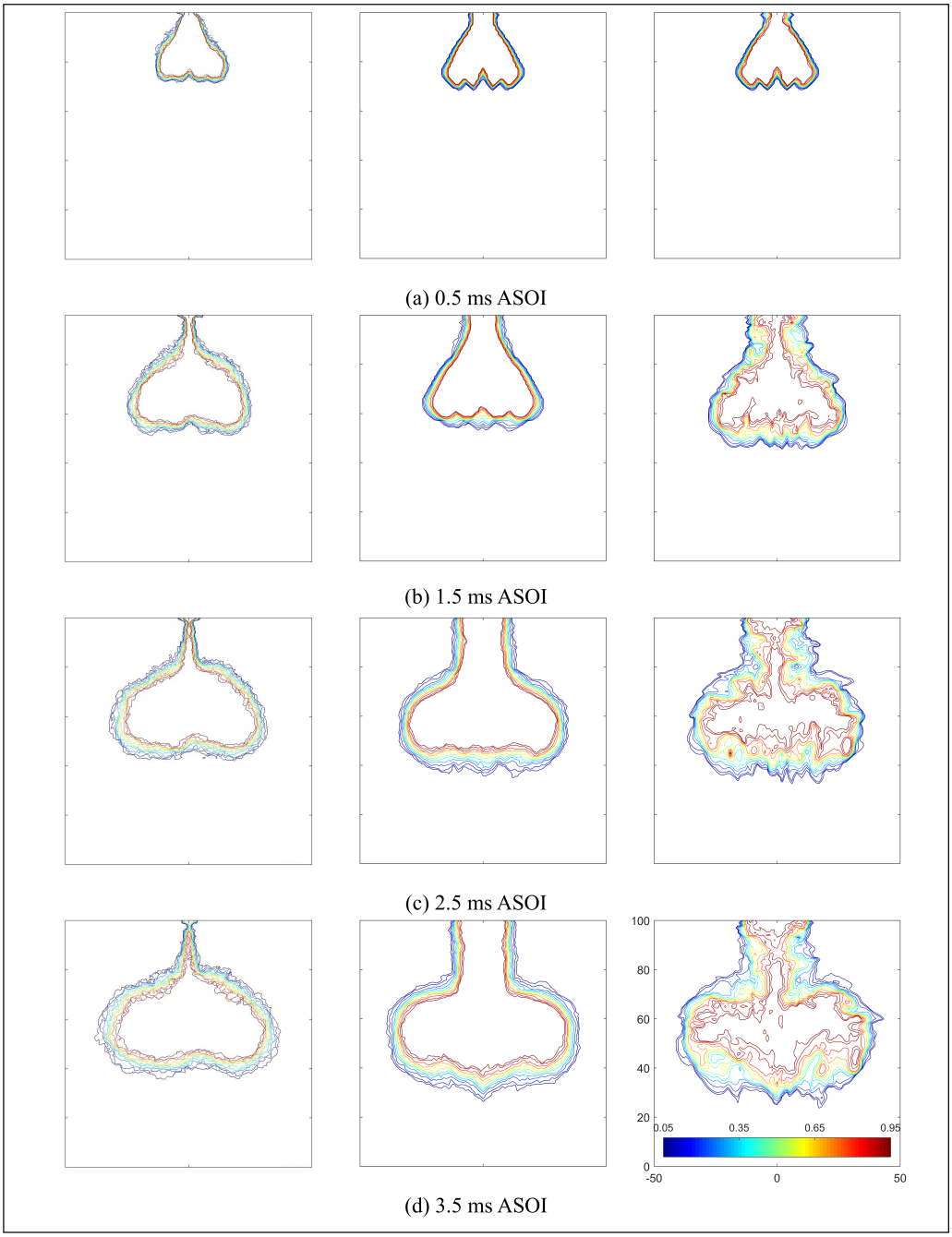

Figure 5.29: Vapor probability contours for case 3 at various times from experiments (left column), LHS (middle column), and PCE (right column). For each contour, there is a 95% chance of producing a vapor region that has the same size as indicated by the innermost region, and a 5% chance of producing a vapor region that has the same size as indicated by the outermost region.

5.5 SGS dispersion modeling

The discussion in this section will be focused on the dispersion modeling for case 1. The tested models include: no model (i.e., $u_i" = 0$ in Equation 4.67), the DRW model, and the SGS model. In the following, simulation results are ensemble-averaged over five realizations and presented as case 1a, 1b, and 1c for the no-model, the DRW model, and the SGS model, respectively (See Table 5.5). The spray characteristics examined include: liquid- and vapor-phase penetrations, droplet SMD and velocity, and projected liquid volume profiles.

Figures 5.30 – 5.31 plot the axial liquid penetrations from experiments and simulations. Experimental data are plotted with shaded area representing the standard deviations, if available. Predicted penetration results are processed using the MMS and PLV methods and ensemble-averaged over five realizations. The first observation concerning the results in Figures 5.30 – 5.31 is that the SGS dispersion model tends to predict shorter liquid residence time compared to the other two models. This is primarily due to the enhanced turbulent dispersion effects as will be discussed later. The turbulent dispersion does not affect the liquid penetration during the initial period of injection ($t < 0.5$ ms ASOI). As injection proceeds, however, it is noticed that the differences among simulation results become larger, especially in the far field where the droplets are significantly influenced by the turbulent ambient gas field. One possible reason is that the liquid droplets in the far field are having much smaller sizes and velocities compared to those in the near-nozzle region, due to droplet breakup, evaporation, and aerodynamic drag. Hence, the associated Stokes numbers are very small as well. According to Section 2.4, those droplets should maintain near velocity equilibrium with the ambient gas, which

eventually gives shorter liquid penetration since the liquid-phase are more dispersed. Overall, a better matching to the experiments is given by the SGS dispersion model, due to the improved prediction of liquid residence times.

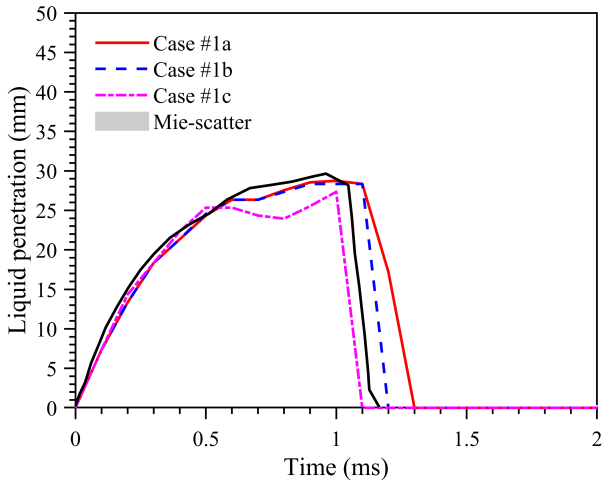

Figure 5.30: Liquid-phase penetrations for case 1 (spray G condition). The predicted results are processed with the MMS method. The experimental data are plotted with the mean only.

Moving to the vapor-phase penetration results plotted in Figure 5.32, the predicted curves appear very similar, suggesting little sensitivity of vapor-phase to the dispersion model. Similar findings were also noted in a recent study by Tsang *et al.* [68] for a diesel spray case. The simulations also over-predict the vapor-phase penetration by as much as 4 mm (about 8% of the maximum vapor penetration) compared to the SNL measurements. However, the trends look very similar. A good agreement can also be found between simulations and Institute Motori measurements.

In addition to the liquid-phase penetrations, the quantitative PLV distributions were obtained from DBI images. Figure 5.33 presents the PLV distributions on the nozzle

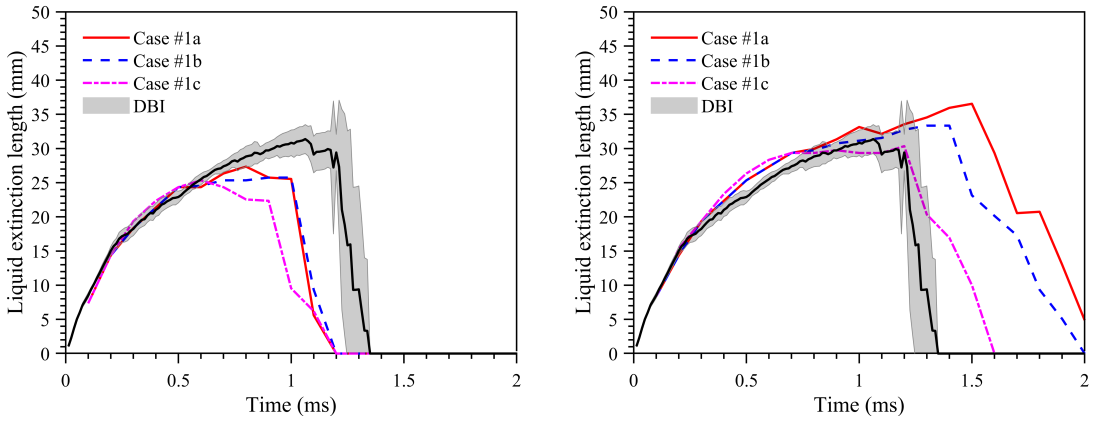

(a) "high" threshold (b) "low" threshold

Figure 5.31: Liquid extinction lengths for case 1 (spray G condition). The predicted results are processed from the PLV profiles with the “high” and "low" thresholds. The experimental data are plotted with the shaded area representing the 95% confidence levels.

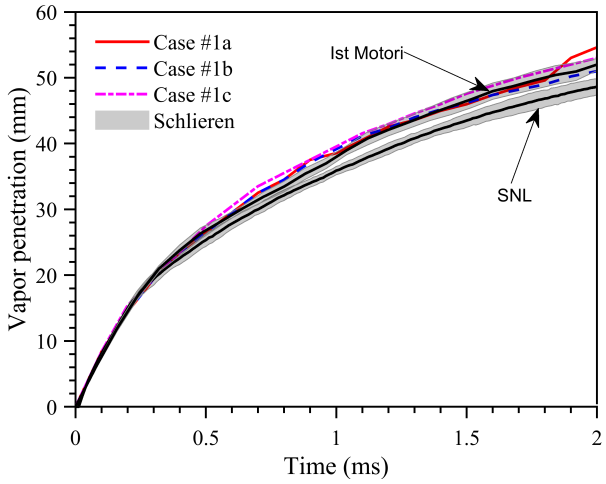

Figure 5.32: Vapor penetration lengths for case 1 (spray G condition). The experimental data are plotted with the shaded area representing the 95% confidence levels. The simulations are form single-realizations.

centerline from the DBI measurements by Joshua Lacey [102]. The measurement results were carefully processed according to the ECN standards. Also plotted are the ensemble averaged PLV profiles from simulations. Since the sampling is done along the nozzle centerline direction (as shown in Figure 5.4), only five samples are available for processing. Experimental data are not available within the first 3 mm to the injector tip due to the experimental difficulties. In each sub-figure, the spray tip determined from the measured liquid penetration in Figure 5.31 is illustrated as a vertical dotted line.

A good agreement between the DBI measurements and simulations with SGS dispersion can be observed at first sight. Simulations with no dispersion and DRW dispersion model, on the other hand, over-predict the PLV distributions at the selected times of 0.3, 0.4, 0.6, 0.7, and 0.8 ms ASOI. At 0.1 ms ASOI (Figure 5.33a), the liquid jet only penetrates about 8.5 mm. Clearly, neither of the simulations produce correct level of PLV within the dense spray region. However, it is questionable whether the PLV in the near-nozzle region should be smaller than that at locations further away from the injector tip. Moving further downstream, the agreement between simulations and experiments becomes better. Note that the SGS dispersion model already starts to play an important role in the radial dispersion of spray droplets at this very early injection time, as evidenced by the reduced PLV values within the dense spray region.

Figures 5.33b – 5.33e show the axial PLV distributions at 0.3, 0.4, 0.6, and 0.7 ms ASOI. As time ASOI increases, the agreement between experiments and simulations with SGS dispersion becomes better, with the best agreement maintained at distances larger than 8 mm. The large differences between simulations and experiments within the dense spray region could be attributed to two factors: uncertainties and difficulties

associated with the experiments, and insufficient breakup descriptions by the model. The near-nozzle analysis from DBI images has always been qualitative due to its long-distance, line-of-sight nature [98]. The second factor is possibly associated with missing or imperfect representation of spray breakup in the near-nozzle region; either because the internal turbulence effects are not considered (which can enhance the spray breakup in the near-nozzle region) or because insufficient experimental data about the plume angle exists. At 0.8 ms ASOI, the measured axial PLV curve drops rapidly towards zero as shown in Figure 5.33f. The predicted PLV distributions also decrease but neither simulation showed a better correlation with the measured data.

Figure 5.34 presents the contour plots of PLV profiles at five selected times of 0.1, 0.3, 0.5, 0.7, and 0.9 ms ASOI [102]. In each sub-figure, experimental data and simulation results with the SGS dispersion model are plotted on the top and bottom rows, respectively. Note that the simulation results show a lower resolution compared to the measured data since the PLV profiles are processed on a 100 × 100 mm grid with a grid size of 1.0 mm. Increasing the grid resolution will show more details but the general trend will not change, since the data are normalized by the grid area (i.e., mm^3 droplet volume per mm^2 grid area). Very good agreement can be observed between DBI measurements and case 1c results in Figures 5.34a - 5.34d. At 0.9 ms ASOI, the measured PLV data are close to zeros, while in simulations there is still a considerable amount of liquid fuel in the computational domain, especially near the nozzle exit.

To investigate the reason for the significant impact of dispersion models on axial PLV distributions, we include the mass-averaged droplet velocity in Figure 5.35. The three components of droplet velocity are sampled at z = 10 mm axial position at 0.7 ms ASOI,

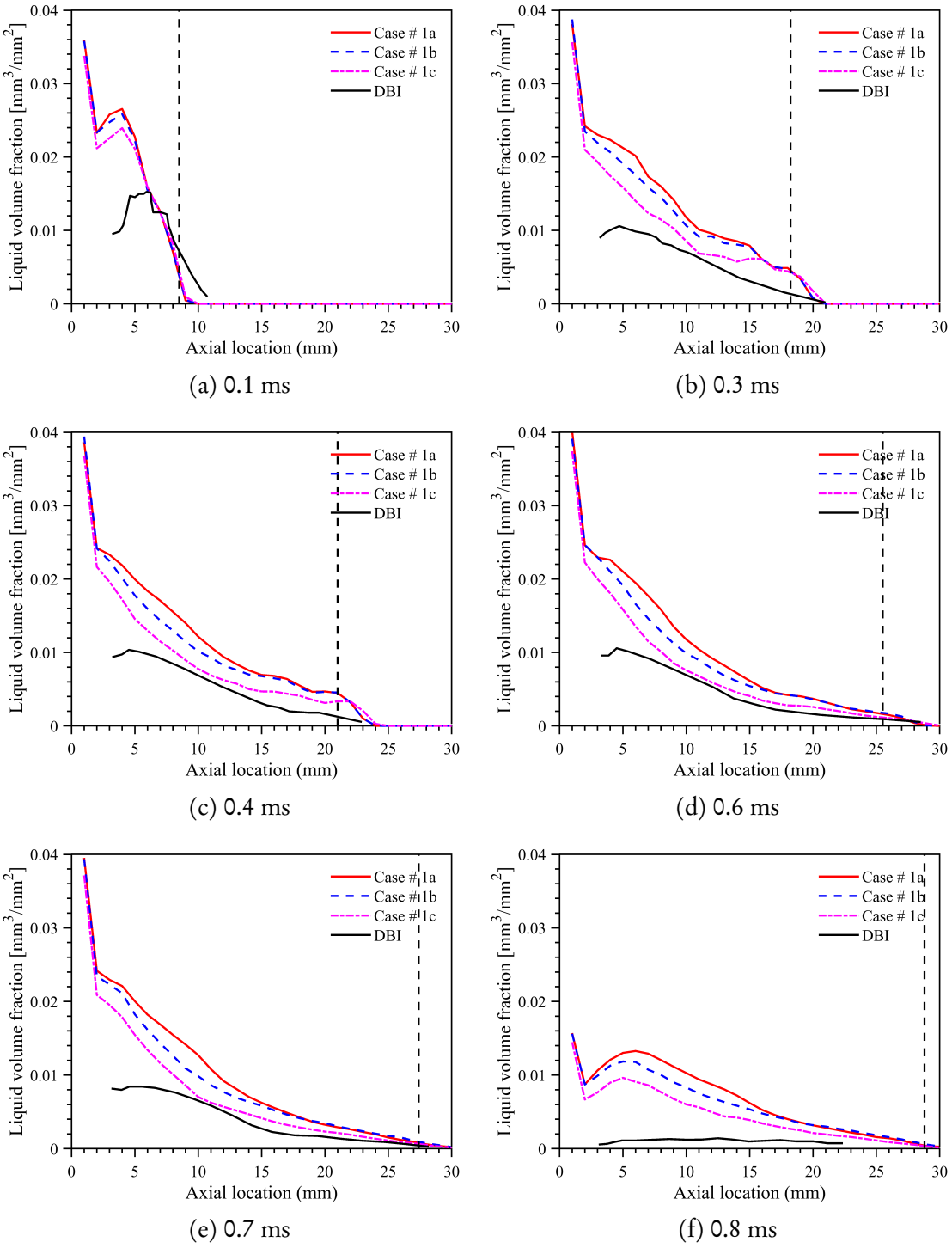

Figure 5.33: Projected liquid volume fractions on the nozzle centerline at various times. Experimental data are plotted using mean values only. LES results are ensemble-averaged over five realizations. In each sub-figure, the instantaneous liquid penetration is illustrated as vertical dotted line.

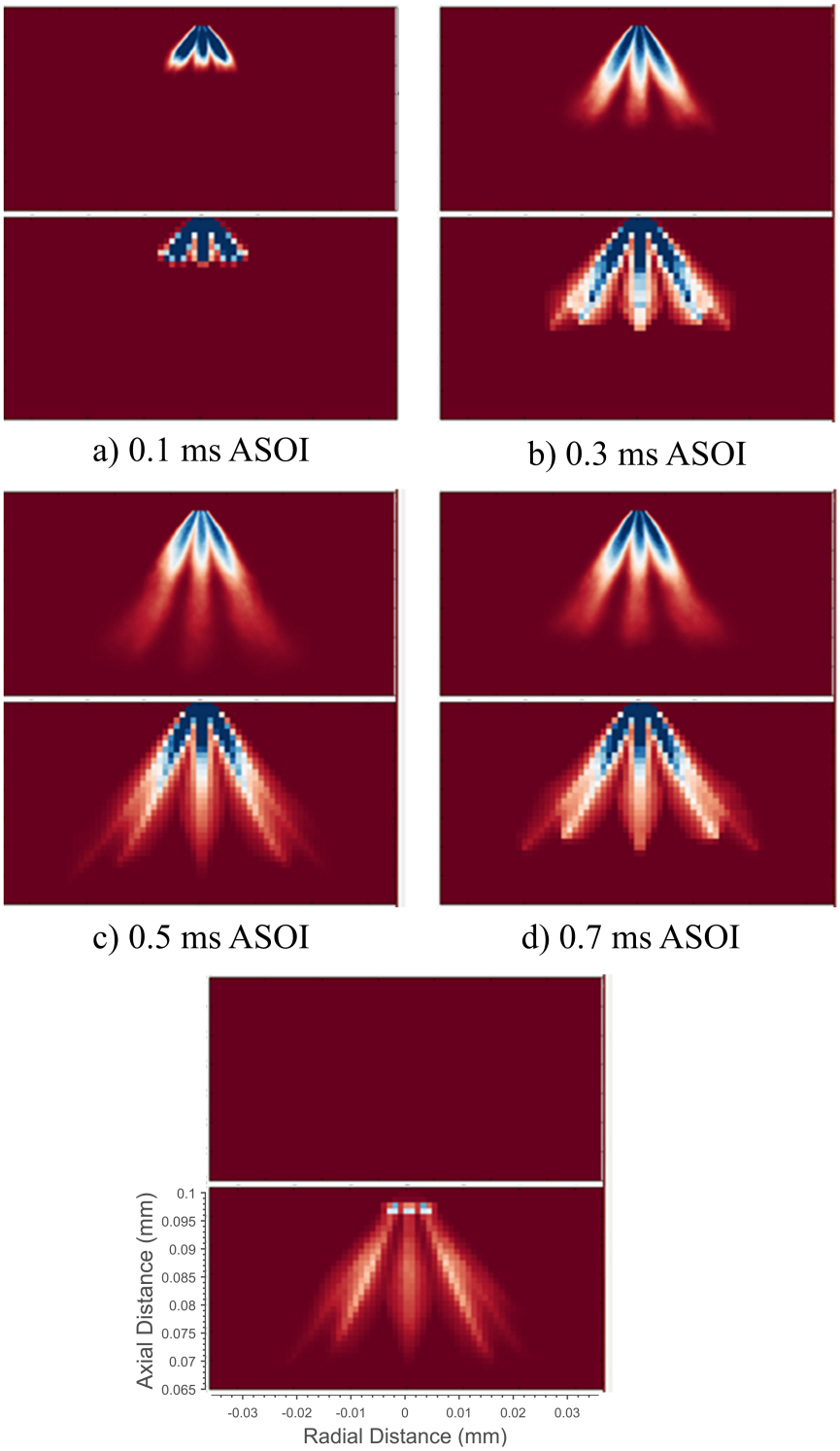

Figure 5.34: PLV maps at five selected times ASOI. In each sub-figure, results from DBI measurements and case 1c simulations are shown on the top and bottom rows, respectively. The ranges are the same (0.0 – 0.01 mm^3/mm^2) between simulations and experiments [102].

a timing when the differences between simulations appear to be the largest as illustrated in Figure 5.33e. A comparison between the left and right columns in Figure 5.35 shows higher velocity magnitudes for the simulations with SGS dispersion model. These are indications that spray droplets are directed in all directions in case 1c. Considering that same spray initial/boundary conditions are used, the higher droplet velocity predicted by simulations with SGS dispersion can be related to smaller droplet acceleration. Note that the higher droplet velocities in the x and y directions produce more disperse spray plumes. Therefore, the less concentrated PLV on the injector centerline is expected.

Continuing to focus on the droplet acceleration, the mass-averaged aerodynamic drag force along the plume center direction (as shown in Figure 5.4) is examined. Results are ensemble-averaged over 40 samples (five realizations each with eight individual plumes) and plotted in Figure 5.36 at four selected times ASOI. Intuitively, one can correlate slower droplet acceleration with smaller aerodynamic drag force. However, this is not necessarily true for the current case. On the contrary, Figure 5.36 shows that the mass-averaged drag force is larger in simulations with SGS dispersion, especially at 0.5 and 0.8 ms ASOI. To explain this, one needs to understand how the acceleration is calculated.

Equation 4.30 indicates that the aerodynamic drag force is proportional to the droplet surface area. On the other hand, droplet mass is proportional to the droplet volume. This leads to the following correlation for droplet acceleration

$$a_d = \frac{F_{i,d}}{m_d} \propto \frac{d^2}{d^3}. \tag{5.2}$$

where a_d is the droplet acceleration. Equation 5.2 indicates that the droplet acceleration is inversely proportionally to the droplet diameter. Combining the observations from

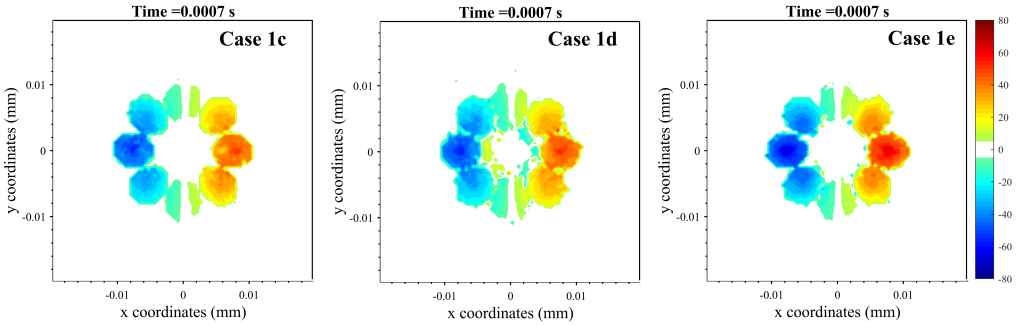

(a) U_x

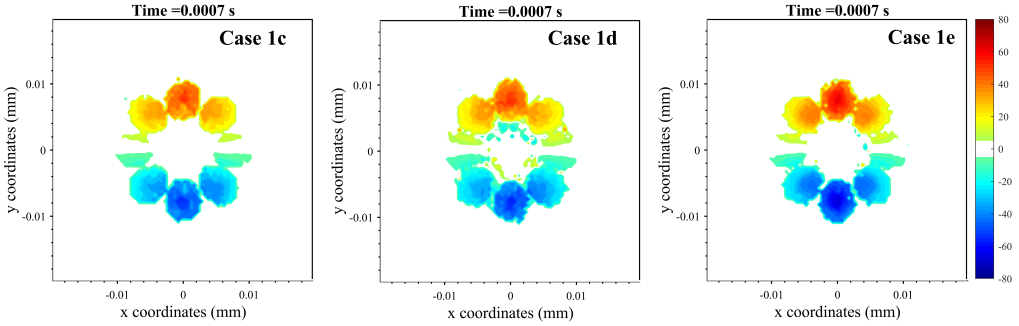

(b) U_y

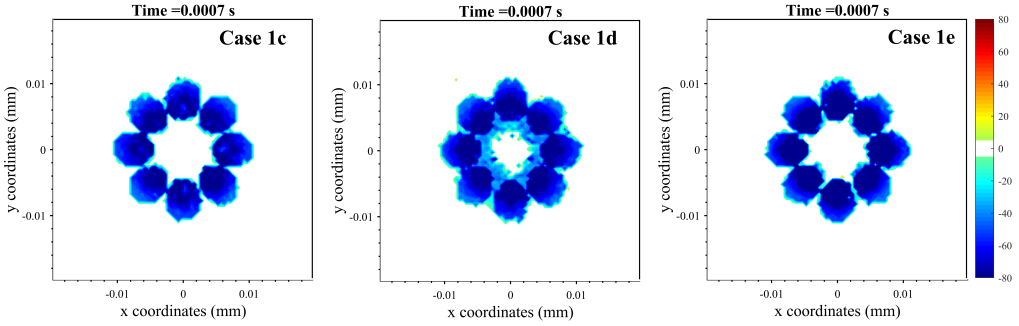

(c) U_z

Figure 5.35: Mass-averaged droplet velocity components at z = 10mm axial position. Results are processed from the first of five realizations for each case at 0.7 ms ASOI.

Figure 5.33 suggests that the spray breakup may be less violent (i.e., larger droplet sizes) in simulations with SGS dispersion.

Another interesting finding from Figure 5.36 is that the aerodynamic drag force decreases dramatically within 3 mm from the nozzle exit during injection, indicating a significant amount of momentum transfer from the liquid-phase to the surrounding ambient. The drag force gradually decreases further downstream until it becomes negligible in the far field, which indicates either a droplet-gas equilibrium (i.e., droplets move with the gas field) or complete vaporization of liquid droplets. At 0.9 ms ASOI, the injection has already ended, hence no droplets are present in the near-nozzle area. The residual droplets in the downstream region also experience much smaller aerodynamic drag.

A comparison of the axial droplet velocity and SMD distributions is then made in Figures 5.37 and 5.38. Sampling is done along the inter plume direction (as shown in Figure 5.4) at z = 15 mm downstream of the injector tip similar to Figures 5.14 and 5.15. The droplet velocity will be discussed first. An immediate observation is that predictions with SGS dispersion match the experimental curve very well. At 0.7 ms ASOI, a timing when the spray has reached a quasi-steady state, the measured maximum axial velocity is about 48 m/s. Predictions with the DRW model and no dispersion model under-estimate this velocity by 6 and 10 m/s, or roughly 13% and 20%, respectively. After the end of injection, the droplet velocities drop gradually. All simulations predict velocity profiles that match the measured curve quite well. A better matching is given by DRW model, but the difference is not significant. In addition to the reduced maximum velocity, a shifting of the spray plumes towards the injector axis can also be observed in both simulations and experiments.

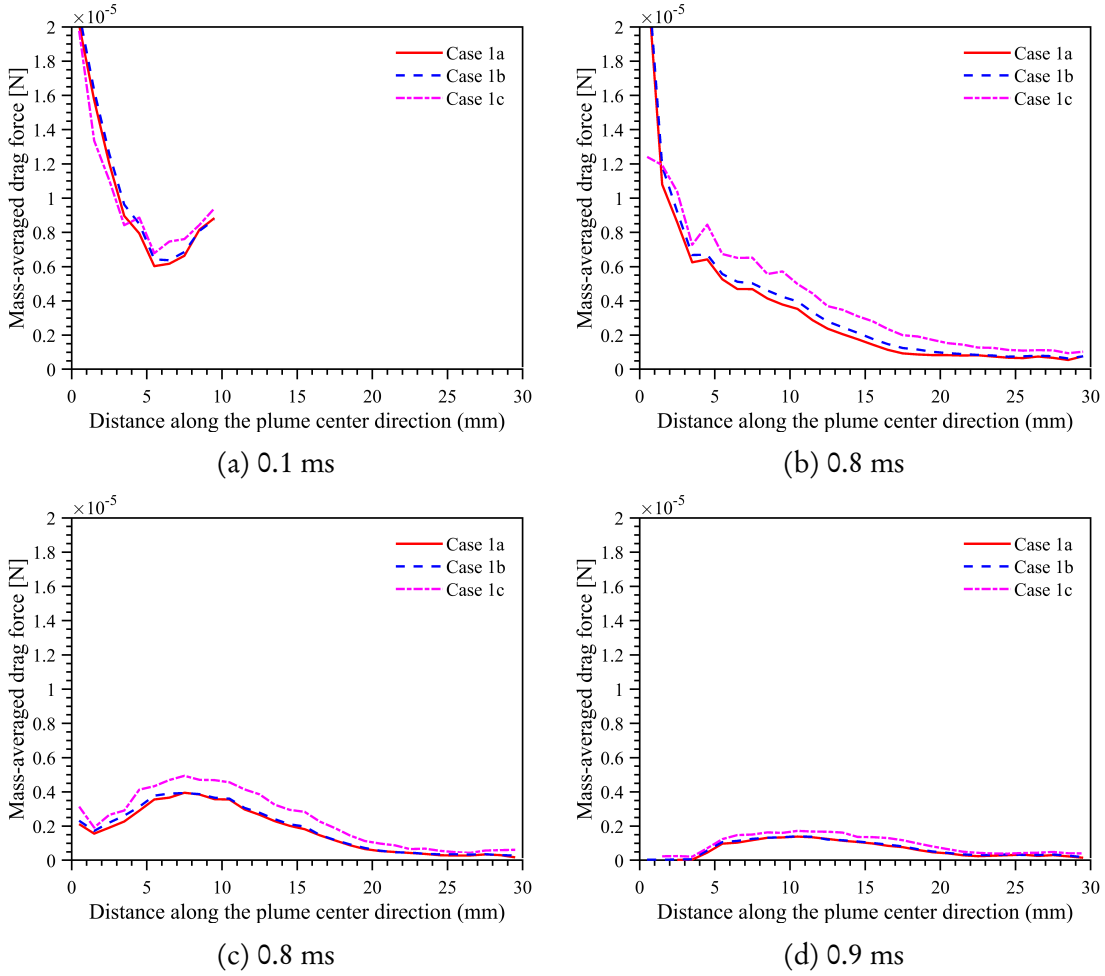

Figure 5.36: Mass-averaged aerodynamic drag force sampled along the plume center direction. Results are ensemble-averaged over five realizations and eight plumes (40 samples in total).

Although showing more fluctuations, the modeling results of droplet SMD match the PDI measurements reasonably well. A major difference between simulations and experiments is that the predicted SMD profiles show a plateau at the plume centers while the measured curves do not. Simulations with SGS dispersion model also predict a higher SMD compared to the other two models. This can be explained by further examining Figure 5.36. In a constant volume chamber where the ambient is initially stagnant, the high-speed liquid jet and fuel droplets contribute to both the resolved and SGS scales through the source terms in Equations 4.34 and 4.37. Most of the momentum exchange between liquid-phase and ambient gas happens in the near-nozzle area, as evidenced in Figure 5.36, where a rapidly reducing drag force magnitude within 3 mm of the nozzle exit can be observed. For simulations with SGS dispersion model, the relative velocity between the liquid parcel and ambient gas is smaller compared to the other two models in the near-nozzle region. Consequently, the drag force magnitudes are smaller, and the breakup is less violently. This also explains why simulations without a dispersion model under-predict the droplet axial velocity at further locations since small droplets tend to accelerate faster as demonstrated in Equation 5.2.

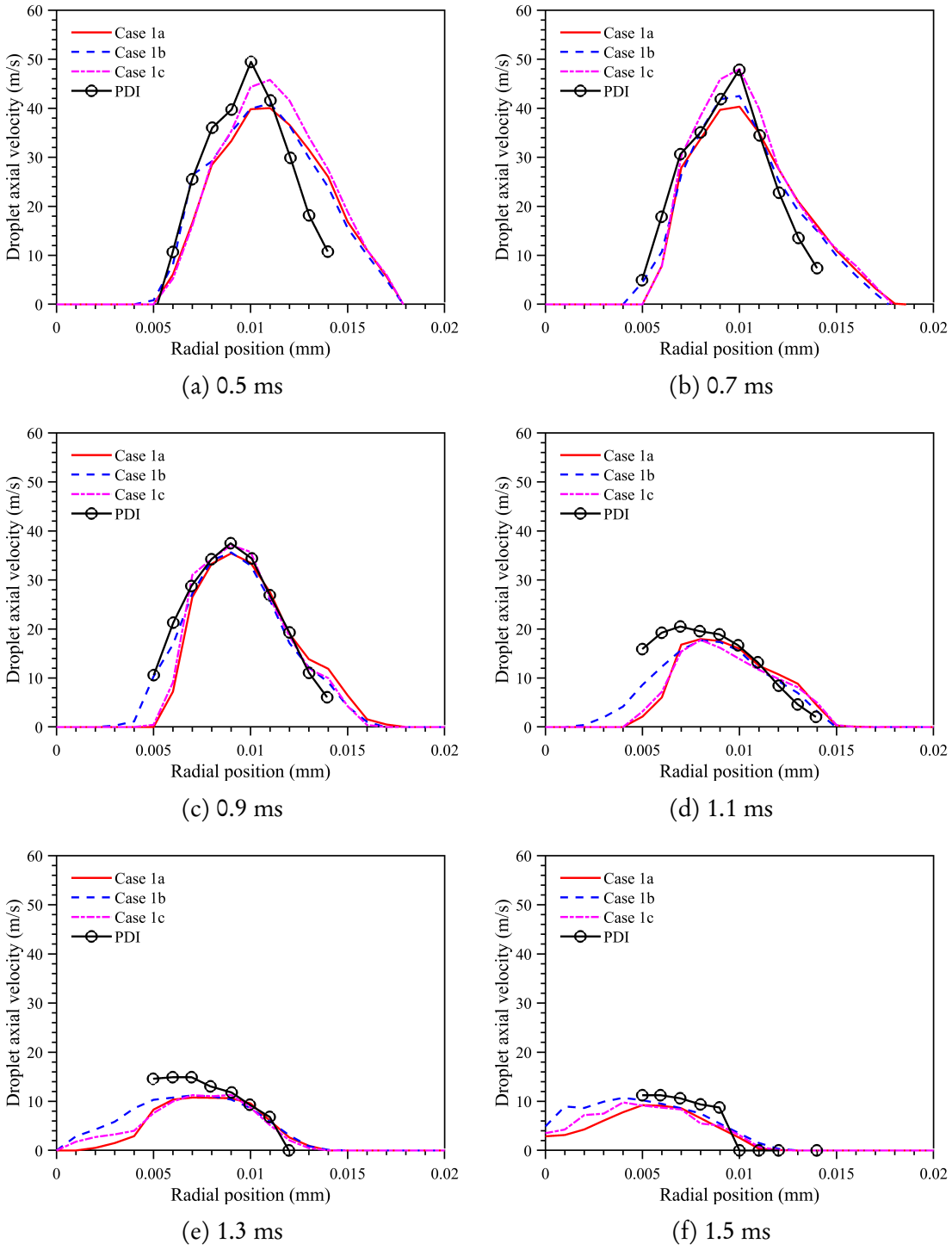

Figure 5.37: Plume-centered radial distribution of the axial droplet velocity for various selected times ASOI. Predicted results are averaged over eight plumes and five realizations.

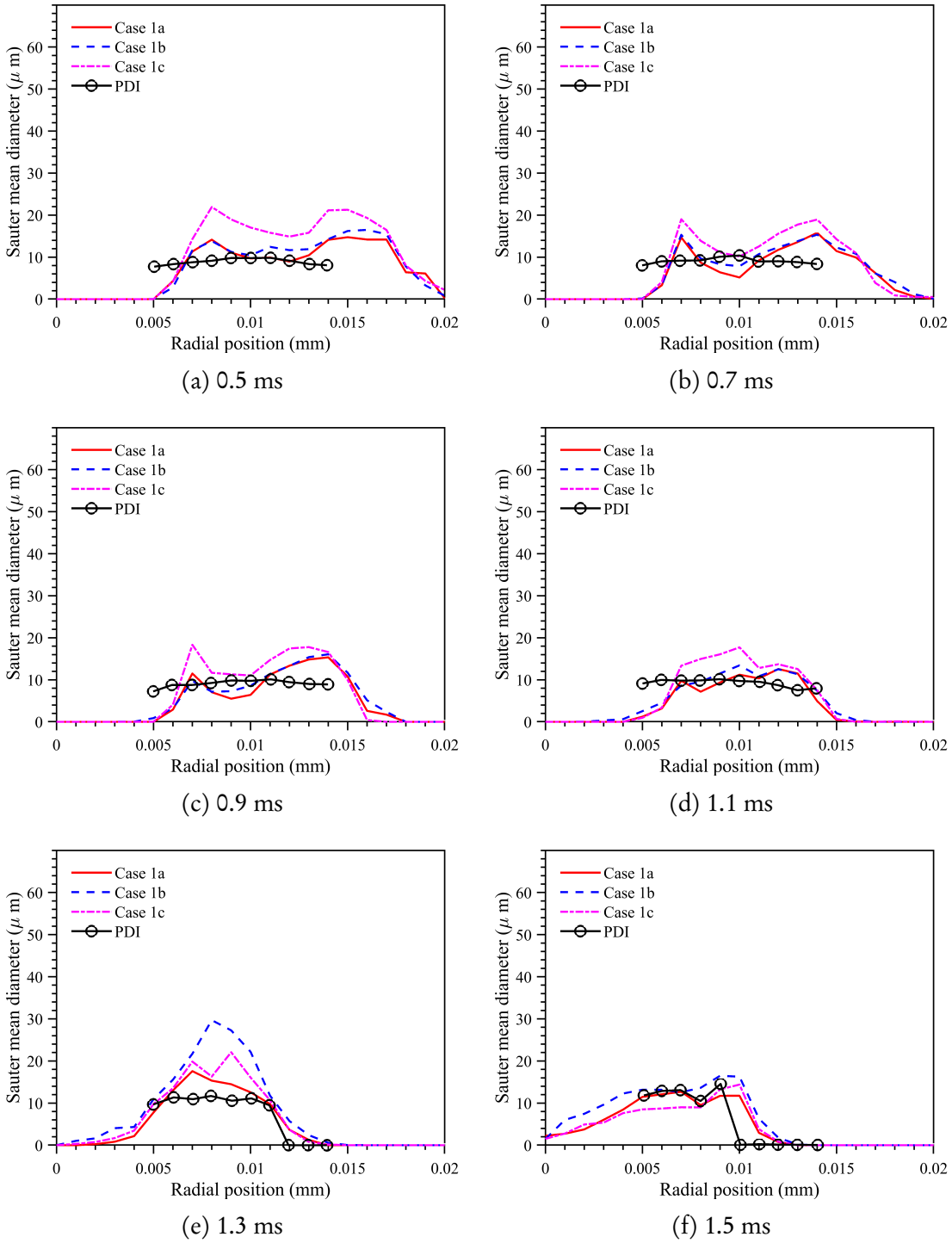

Figure 5.38: Plume-centered radial distribution of the droplet SMD for various selected times ASOI. Predicted results are averaged over eight plumes and five realizations.

5.6 SGS energy dissipation rate modeling

Evaluation of the SGS energy dissipation rate model developed in this work (see Section 4.5) is carried out using the three meshes described in Section 5.2. Simulations results with the classic model with and without scaling of the model parameter are also presented in this section for comparison purposes. As listed in Table 5.5, simulations are conducted with the IAB breakup model and the SGS dispersion model.

Figure 5.39 presents the vapor-phase penetrations from experiments and simulations for cases 1c, 1d, and 1e, respectively. Starting with the top and middle rows, where the results are obtained using the classic dissipation rate model with and without the parameter scaling, respectively. It can be seen in Figure 5.39a that while the scaling of the model parameter reduces the mesh sensitivity, the variance among all three meshes is still noticeable. The classic model severely over-predicts the vapor-phase penetration with the 0.375 mm mesh. This is caused by the over-estimation of the energy dissipation rate. This hypothesis will be explored in detail later. On the other hand, results for case 5.39c show significantly improved mesh independence. The vapor-phase penetrations after the end of injection also show improved matching with the SNL data.

The liquid-phase penetrations are estimated using the PLV method with the "low threshold" and plotted in Figure 5.40 for cases 1c – 1e. Similar to the vapor penetrations, the liquid penetrations also show more noticeable variance for the classic model without scaling, as shown in Figure 5.40b. In cases 1c and 1e, the results are less mesh sensitive similar to the vapor penetrations. However, the liquid lengths for case 1e are underestimated, indicating that the spray breakup model may need to be re-calibrated. Note that as the mesh resolution increases, the predicted liquid-phase penetration shows a

"zigzag" evolution. The reason for this behavior is unknown at this point. However, the penetration curves show similar trends after EOI, which are also consistent with the experiments.

To help explain the different mesh dependencies observed in cases 1c – 1e, the following discussion will be focused on the energy dissipation rate, ε_{sgs}, for the 0.375 mm mesh. Results on the x-y plane are plotted in Figure 5.41 at three selected times of 0.3, 0.7, and 1.1 ms ASOI. Start with the results at 0.3 ms ASOI presented on the left column, an immediate observation is that predicted shapes and characteristic sizes of ε_{sgs} are very similar among all three cases. However, case 1d shows higher values of ε_{sgs} in the near-nozzle area compared to the other two cases. Recall that the time derivative of SGS kinetic energy, k_{sgs}, is directly linked to ε_{sgs} (see Equation 4.23)

$$\frac{\partial k_{sgs}}{\partial t} \propto= -\varepsilon_{sgs}. \tag{5.3}$$

This implies that too much k_{sgs} may have been removed from the SGS field for case 1d. Proceed to the middle column, where results are shown at 0.7 ms ASOI, noticeable differences among case 1c – 1e can be observed. Compared to the other two cases in the near-nozzle area, case 1d continues to show higher ε_{sgs} but the characteristic footprint below the injector is much smaller. This suggests that the energy budget of k_{sgs} and the energy cascade may not be properly described in case 1d. The differences become even larger at 1.1 ms ASOI, as the right column in Figure 5.41 shows. Cases 1c and 1e exhibit a plume collapsing toward the injector centerline, which correlates well with the findings in Ref. [95]. Case 1d, on the other hand, does not show such behavior as evidenced by the distinct boundaries between the plume pairs. Note that case 1e also shows more variance

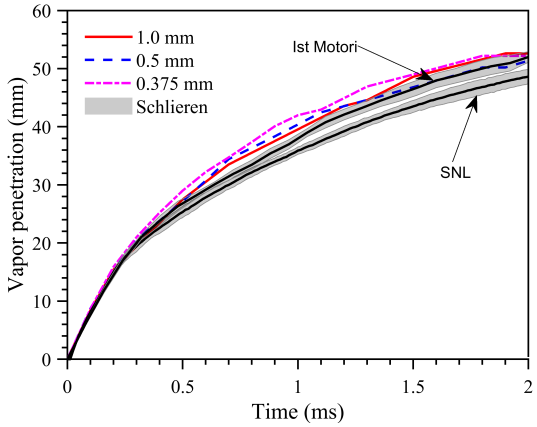

(a) Case 1c

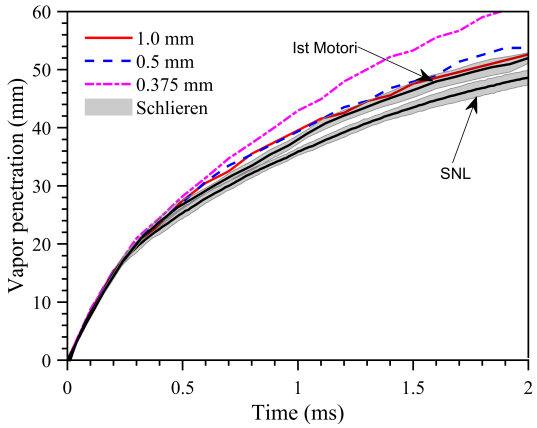

(b) Case 1d

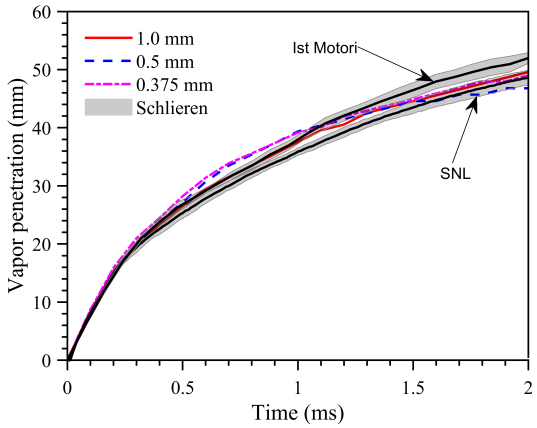

(c) Case 1e

Figure 5.39: Vapor-phase penetrations predicted by Cases 1c – 1e using three meshes with minimum cell sizes of 1.0, 0.5, and 0.375 mm. The predicted results are processed with a local fuel mass fraction of 0.001.

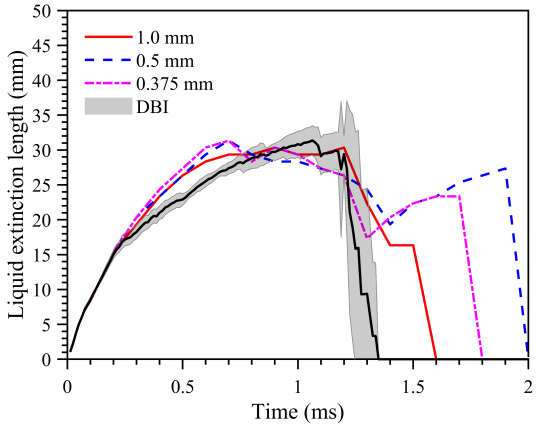

(a) Case 1c

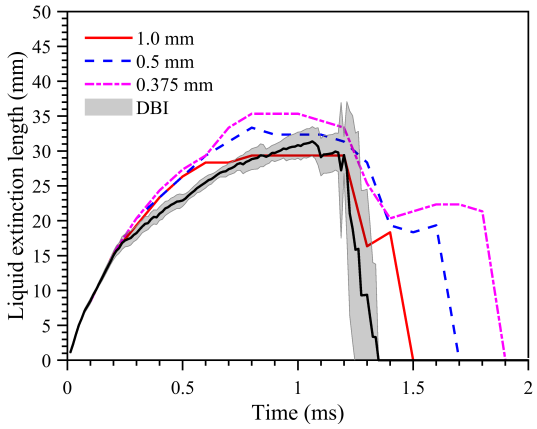

(b) Case 1d

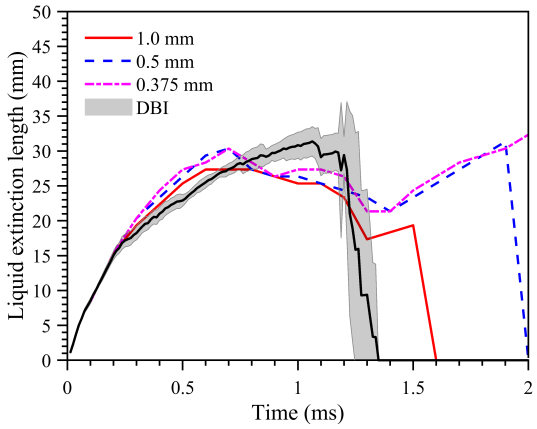

(c) Case 1e

Figure 5.40: Liquid-phase penetrations predicted by cases 1c – 1e using three meshes with minimum cell sizes of 1.0, 0.5, and 0.375 mm. Results are processed using the PLV method with the “low” threshold.

on the outer side, which may be introduced by the Leonard-type term in Equation 4.83.

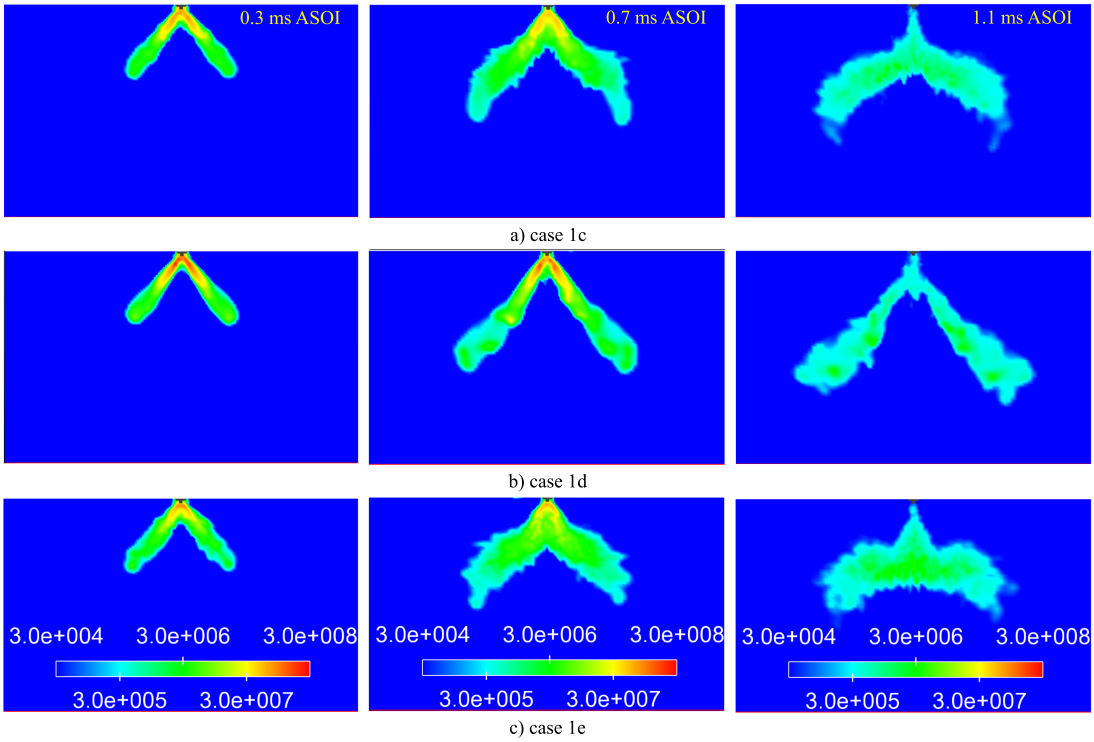

Figure 5.41: SGS energy dissipation rates with 0.375 mm mesh for cases 1c - 1e. Results are plotted on the x-y plane through nozzle centerline. From the left to the right, results are presented at 0.3, 0.7, and 1.1 ms ASOI, respectively.

Continue focusing on the energy cascade, one can now examine the ratio of k_{sgs} to the total kinetic energy, calculated as the summation of k_{sgs} and resolved kinetic energy, K. Results are plotted in Figure 5.42 for cases 1c – 1e. Similar findings to ε_{sgs} are observed for the kinetic energy ratio. According to Equation 5.3, the over-estimation of ε_{sgs} in case 1d will lead to under-estimated k_{sgs}, which is supported by the smaller kinetic energy ratios found in Figure 5.42. The energy removal from the resolved filed is also under-estimated, since, in the dynamic structure turbulent closure, the SGS stress tensor scales with the

k_{sgs} (See Equation 4.17). As a consequence, the vapor-phase penetration is over-predicted as shown in Figure 5.39.

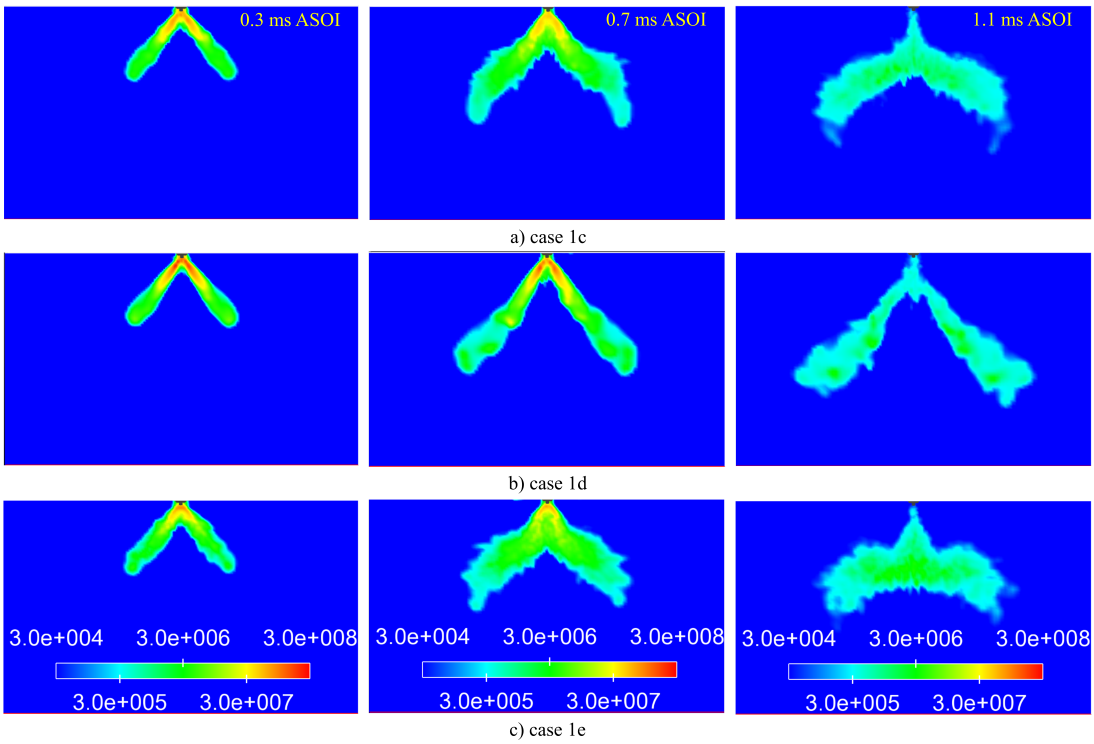

Figure 5.42: Ratio of k_{sgs} to total kinetic energy with 0.375 mm mesh for cases 1c, 1d, and 1e. Results are plotted on the x-y plane through nozzle centerline. From the left to the right, results are presented at 0.3, 0.7, and 1.1 ms ASOI, respectively.

6 CONCLUSIONS AND FUTURE WORK

6.1 Conclusions

The research carried out during this Ph.D. has focused on the development of predictive models for turbulent mixing in direct injection spark-ignition engines. Over the course of this work, three models have been developed

- A model for the spray breakup
- A model for the SGS turbulent dispersion
- A model for the SGS energy dissipation rate.

The new models were incorporated into the large-eddy simulation framework developed at the Engine Research Center, University of Wisconsin-Madison. A variation of the OpenFOAM-2.3.x code was used as the CFD platform. A mixed-type dynamic structure model was used as the LES turbulent closure. The model utilizes a transport equation for the SGS kinetic energy, therefore gives satisfactory results with relatively coarse meshes commonly found in engine simulations. The SGS kinetic energy obtained by solving the transport equation also serves as a basis for the SGS models developed in this work.

The spray breakup model, termed as the "Integrated Atomization/Breakup (IAB)" model, has been developed based on the Lagrangian-Eulerian approach. Atomization and breakup of the liquid parcels are divided into two regimes, namely, the bag/bag-stamen breakup regime, and the high Weber number regime. In the first regime, a phenomenological bag breakup model has been developed to track the breakup process. In the second

regime, the KH-RT model developed by Reitz and coworkers is adopted with a modified RT breakup length concept to account for the plume-interactions in DISI engines.

The SGS turbulent dispersion model builds on the idea of velocity decomposition, in which the instantaneous gas-phase velocity is assumed to have a deterministic part and a stochastic part. The deterministic part is reconstructed from the resolved fields using the approximate deconvolution method. The stochastic part, on the other hand, is assumed to be locally isotropic and hence governed by a Langevin-type stochastic differential equation. The SGS energy dissipation rate model belongs to the dynamic structure SGS models, in which the modeled energy dissipation rate term is constructed from the corresponding Leonard term and a scaling term, which was developed based on the findings from reported direct numerical simulation study of decaying isotropic turbulence.

Extensive a posteriori tests have been carried out under DISI engine-like conditions. Experimental data available in the literature were used for the calibration and evaluation of all three models. The evaluation of spray models was carried out in a step-wise fashion, from spray breakup modeling to SGS turbulent dispersion modeling, focusing primarily on DISI breakup characteristics. The study finished with a preliminary test of the SGS energy dissipation rate modeling. The most important findings obtained in this study are listed below

DISI spray breakup modeling

- The IAB model showed better predictability in comparison with the widely used KH-RT model, due to the newly developed bag breakup sub-model

- After the end-of-injection, most of the residual liquid droplets break via the defor-

mation, bag, and multi-model breakup mechanisms

- The IAB model showed great promise for predicting reduced, more accurate droplet SMD distributions
- The modified RT breakup length concept can be extended to a wide range of operating conditions without further tuning the parameter value
- An uncertainty quantification study revealed that the IAB model predicts accelerated breakup speed in the bag and bag-stamen breakup regimes.

SGS turbulent dispersion modeling

- The SGS model showed improved predictions of the projected liquid volume fraction for the ECN experiments on the injector centerline for Spray G conditions
- For high-speed sprays in constant volume chambers, the majority of momentum exchange between the liquid-phase and ambient gas occurs in the near-nozzle region
- In the near-nozzle region, the SGS model predicts lower aerodynamic drag magnitudes in comparison with the discrete random walk model and no dispersion model and hence results in slightly higher droplet SMD
- Downstream of the injector exit, the predicted aerodynamic drag magnitudes are higher with the SGS model, due to the larger droplet sizes
- Overall, the SGS model showed improved predictions of radial dispersion of liquid droplets.

SGS energy dissipation rate modeling

- The SGS model achieves good mesh independence among three mesh resolutions studied. This is most likely due to the improved scaling of energy dissipation rates with the SGS kinetic energy and LES filter width
- The classic model developed based on the dimensional analysis cannot guarantee accurate budgets of SGS kinetic energy across different mesh resolutions without tuning the model parameter for each mesh.

6.2 Future work

The proposed outline of the future work is as follows:

- **Linking with internal flow simulations.** The initial and boundary conditions at DISI injector exits are essential for high-fidelity DISI spray simulations. Yet their values are hard to measure in experiments due to the noticeable plume-to-plume interactions. Internal flow simulations with the volume of fluid (no phase-change) or homogeneous relaxation (with phase-change) approach seem to offer promising and realistic flow conditions at the nozzle orifices, which can be utilized to initialize the external spray simulations. However, the methodology to correctly link the internal flow and external spray simulations still remains a challenge
- **Cavitation, flash boiling, in-nozzle turbulence.** A recent study by Agarwal and Trujillo [38] raises questions about the validity of linking linear stability analysis with atomization for a high-pressure diesel spray case. This is also true for DISI

sprays with more volatile gasoline fuels since internal turbulence and phase-change phenomena can contribute to the atomization as well. Cavitation and flash boiling are likely two important phenomena that the model needs to capture when internal phase-change is considered. Unlike detailed internal flow simulations, semi-theoretical and/or correlations exist in the literature which can be readily used to assess the impact of these phenomena

- **More testing of the SGS turbulent dispersion model.** Though *a posteriori* test results are encouraging at this point. *A priori* testing needs to be conducted to further evaluate the model. Particle dispersion in free shear flows (e.g., jets, mixing layer, wakes . . .) and particle-laden flows is ideal for such testing. Besides, the Stokes number in Equation 2.5 is ambiguously defined even though it is widely used in the reported studies. Recently, Trujillo and Parkhill [113] gave another definition which avoids the ambiguity by using the local flow quantities. It is therefore suggested to examine the Droplet Stokes number effects.

- **More testing of the SGS energy dissipation rate model.** It would be useful to perform *a priori* testing of the model such as decaying isotropic turbulence simulations. If good correlations with the DNS results are obtained, then proceed with high-pressure diesel spray and/or gas jet simulations.

7 BIBLIOGRAPHY

[1] Zhao, F., Lai, M.-C., and Harrington, D., 1999. "Automotive spark-ignited direct-injection gasoline engines". *Progress in Energy and Combustion Science,* ***25***(5), pp. 437–562.

[2] Chryssakis, C., and Assanis, D., 2008. "A unified fuel spray breakup model for internal combustion engine applications". *Atomization and Sprays,* ***18***, pp. 1–52.

[3] Ashgriz, N., ed. *Handbook of Atomization and Sprays: Theory and Applications*. Springer New York, Toronto Ontario.

[4] Rutland, C. J., 2011. "Large-eddy simulations for internal combustion engines - A review". *International Journal of Engine Research,* ***12***(5), pp. 421–451.

[5] Foundation, O., 2015. OpenFOAM-2.3.x. https://github.com/OpenFOAM/OpenFOAM-2.3.x.

[6] Tsang, C.-w., 2017. "Large-Eddy Simulation Modeling of Diesel".

[7] Reitz, R.D.; Bracco, F., 1982. "Mechanism of Atomization of Liquid Jets". *The Physics of Fluids,* ***25***.

[8] Baumgarten, C., 2006. *Mixture Formation in Internal Combustion Engine*. Springer Berlin Heidelberg.

[9] Balewski, B., Heine, B., and Tropea, C., 2010. "Experimental investigation of the correclation between nozzle flow and spray using laser doppler velocimeter,

phase doppler system, high-speed photography, and radiography". *Atomization and Sprays,* ***20***(September 2008), pp. 57–70.

[10] Pilch, M., and Erdman, C. A., 1987. "Use of breakup time data and velocity history data to predict the maximum size of stable fragments for acceleration-induced breakup of a liquid drop". *International Journal of Multiphase Flow,* ***13***(6), pp. 741–757.

[11] Krzeczkowski, S. A., 1980. "Measurement of liquid droplet disintegration mechanisms". *International Journal of Multiphase Flow,* ***6***(3), pp. 227–239.

[12] Hsiang, L. P., and Faeth, G. M., 1992. "Near-limit drop deformation and secondary breakup". *International Journal of Multiphase Flow,* ***18***(5), pp. 635–652.

[13] Hsiang, L.-P., and Faeth, G. M., 1995. "Drop Deformation and breakup due to shock wave and steady disturbances". *Int. J. Multiphase Flow,* ***21***(4), pp. 545–560.

[14] Faeth, G. M., Hsiang, L. P., and Wu, P. K., 1995. "Structure and breakup properties of sprays". *International Journal of Multiphase Flow,* ***21***, pp. 99–127.

[15] Chou, W.-H., Hsiang, L.-P., Faeth, G., Chou, W.-H., Hsiang, L.-P., and Faeth, G., 1997. "Dynamics of drop deformation and formation during secondary breakup in the bag breakup regime". *35th Aerospace Sciences Meeting and Exhibit*(January).

[16] Chou, W.-H., and Faeth, G., 1998. "Temporal properties of secondary drop breakup in the bag breakup regime". *International Journal of Multiphase Flow,* ***24***(6), pp. 889–912.

[17] Dai, Z., and Faeth, G. M., 2001. "Temporal properties of secondary drop breakup in the multimode breakup regime". *International Journal of Multiphase Flow,* ***27***(2), pp. 217–236.

[18] Liu, Z., and Reitz, R. D., 1997. "An analysis of the distortion and breakup mechanisms of high speed liquid drops". *International Journal of Multiphase Flow,* ***23***(4), pp. 631–650.

[19] Lee, C. S., and Reitz, R. D., 2001. Effect of Liquid Properties on the Breakup Mechanisms of High Speed Liquid Drops.

[20] Opfer, L., Roisman, I. V., and Tropea, C., 2012. "Aerodynamic Fragmentation of Drops : Dynamics of the Liquid Bag". *ICLASS 2012, 12th Triennial International Conference on Liquid Atomization and Spray Systems*, pp. 1–8.

[21] Theofanous, T. G., Li, G. J., and Dinh, T. N., 2004. "Aerobreakup in Rarefied Supersonic Gas Flows". *Journal of Fluids Engineering,* ***126***(4), p. 516.

[22] Gelfand, B. E., 1996. "Droplet breakup phenomena in flows with velocity lag". *Progress in Energy and Combustion Science,* ***22***(3), pp. 201–265.

[23] Girin, A. G., 2012. "on the Mechanism of Inviscid Drop Breakup At Relatively Small Weber Numbers". *Atomization and Sprays,* ***22***(11), pp. 921–934.

[24] Guildenbecher, D. R., López-Rivera, C., and Sojka, P. E., 2009. "Secondary atomization". *Experiments in Fluids,* ***46***(3), pp. 371–402.

[25] Chryssakis, C. A., Assanis, D. N., and Tanner, F. X., 2011. *Handbook of atomization and sprays*.

[26] Girin, A. G., and Ivanchenko, Y. A., 2012. “Model of Liquid Film Disintegration At "Bag" Mode of Drop Breakup”. *Atomization and Sprays,* ***22***(11), pp. 935–949.

[27] Giffen, Edmund; Muraszew, A., 1953. *The atomisation of liquid fuels*. Chapman & Hall, London.

[28] Jalaal, M., and Mehravaran, K., 2012. “Fragmentation of falling liquid droplets in bag breakup mode”. *International Journal of Multiphase Flow,* ***47***, pp. 115–132.

[29] Nicholls, J. A., and Ranger, A. A., 1969. “Aerodynamic shattering of liquid drops.”. *AIAA Journal,* ***7***(2), pp. 285–290.

[30] Chou, W. H., Hsiang, L. P., and Faeth, G. M., 1997. “Temporal properties of drop breakup in the shear breakup regime”. *International Journal of Multiphase Flow,* ***23***(4), pp. 651–669.

[31] Liu, A. B., Mather, D., and Reitz, R. D., 1993. “Modeling the Effects of Drop Drag and Breakup on Fuel Sprays.”. *SAE International Congress and Exposition,* ***298***(412), pp. 1–6.

[32] Hiroyasu, H., 1991. “Break-up length of a liquid jet and internal flow in a nozzle”. In Proc. 5th. ICLASS, pp. 275–282.

[33] Silverman, I., and Sirignano, W. A., 1994. “Multi-droplet interaction effects in dense sprays”. *International Journal of Multiphase Flow,* ***20***(1), pp. 99–116.

[34] Jiang, X., Siamas, G. A., Jagus, K., and Karayiannis, T. G., 2010. “Physical modelling and advanced simulations of gas-liquid two-phase jet flows in atomization and sprays”. *Progress in Energy and Combustion Science,* ***36***(2), pp. 131–167.

[35] Crowe, C. T., Chung, J. N., and Troutt, T. R., 1988. "Particle mixing in free shear flows". *Progress in Energy and Combustion Science,* ***14***(3), pp. 171–194.

[36] Pope, S. B., 2013. "Small scales, many species and the manifold challenges of turbulent combustion". *Proceedings of the Combustion Institute,* ***34***(1), pp. 1–31.

[37] Amsden, A. A., O'Rourke, P. J., and Butler, T. D., 1989. "KIVA-II: A Computer Program for Chemically Reactive Flows with Sprays". *Los Alamos National Lab.*,, pp. LA–11560–MS.

[38] Agarwal, A., and Trujillo, M. F., 2018. "A Closer Look at Linear Stability Theory in Modeling Spray Atomization". *International Journal of Multiphase Flow,* ***0***, pp. 1–13.

[39] Umemura, A., and Shinjo, J., 2018. "Detailed SGS atomization model and its implementation to two-phase flow LES". *Combustion and Flame,* ***195***, pp. 232–252.

[40] Reitz, R. D., 1987. "Modeling Atomization Processes in High-Pressure Vaporizing Sprays". *Atomization and Sprays,* ***3***, pp. 309–337.

[41] Levy, N., Amara, S., and Champoussin, J.-C., 1998. "Simulation of a diesel jet assumed fully atomized at the nozzle exit".

[42] Huh, K. Y., Lee, E. J., and Koo, J. Y., 1998. Diesel spray atomization model considering nozzle exit turbulence conditions.

[43] Arcoumanis, C., Gavaises, M., and French, B., 1997. "Effect of Fuel Injection Processes on the Structure of Diesel Sprays".

[44] Baumgarten, C., Stegemann, J., Merker, G. P., Verbrennung, T., and Hannover, U., 2002. "a new model for cavitation induced primary break-up of diesel sprays". In ILASS-Europe 2002, no. September.

[45] Arai, J., Oshima, M., Oshima, N., Ito, H., and Kubota, M., 2007. "Large Eddy Simulation of Spray Injection to Turbulent Duct Flow from a Slit Injector". *Journal of Fluid Science and Technology,* ***2***(2007-01-1403), pp. 2917–2923.

[46] Nishad, K. P., Sadiki, A., and Janicka, J., 2011. "A Comprehensive Modeling and Simulation of Gasoline Direct Injection using KIVA-4 code". *SAE Paper*, pp. 626–633.

[47] Nishad, K., Pischke, P., Goryntsev, D., Sadiki, A., and Kneer, R., 2012. "LES Based Modeling and Simulation of Spray Dynamics including Gasoline Direct Injection (GDI) Processes using KIVA-4 Code". *SAE Technical Paper*(2012-01-1257).

[48] Schmidt, D. P., Nouar, I., Senecal, P. K., Rutland, C. J., Martin, J. K., Reitz, R. D., and Hoffman, J. A., 1999. "Pressure-Swirl Atomization in the Near Field".

[49] Tanner, F., 1997. "Liquid jet atomization and droplet breakup modeling of non-evaporating diesel fuel sprays". *SAE Interational,* ***106***(412), pp. 127–140.

[50] IBRAHIM, E. A., YANG, H. Q., and PRZEKWAS, A. J., 1993. "Modeling of spray droplets deformation and breakup". *Journal of Propulsion and Power,* ***9***(4), jul, pp. 651–654.

[51] Park, J.-H., Yoon, Y., and Hwang, S.-S., 2002. Improved Tab Model for Prediction of Spray Droplet Deformation and Breakup. http://www.dl.begellhouse.com/journals/6a7c7e10642258cc,0aadde6445fb7bec,70702cf147adee86.h

[52] Dan, T., Takagishi, S., Senda, J., and Fujimoto, H., 1997. "Effect of ambient gas properties for characteristics of non-reacting Diesel fuel sprays". *SAE technical paper 970352,* ***970352***(412).

[53] Tanner, F. F. X., 2003. "A cascade atomization and drop breakup model for the simulation of high-pressure liquid jets". *SAE transactions*(724).

[54] Reitz, R. D., and Diwakar, R., 1987. "Structure of High-Pressure Fuel Sprays". In SAE Tech. Pap. Ser.

[55] Su, T. F., Patterson, M. A., Reitz, R. D., and Farrell, P. V., 1996. "Experimental and numerical studies of high pressure multiple injection sprays". *SAE Technical Papers*(412).

[56] Ricart, L. M., Xin, J., Bower, G. R., and Reitz, R. D., 1997. "In-Cylinder Measurement and Modeling of Liquid Fuel Spray Penetration in a Heavy-Duty Diesel Engine". *SAE Technical Papers*(412).

[57] Reitz, R. D., and Beale, J. C., 1999. "Modeling Spray Atomization With the Kelvin-Helmholtz/Rayleigh-Taylor Hybrid Model". *Atomization and Sprays,* ***9***(6), pp. 623–650.

[58] Li, Z. H., He, B. Q., and Zhao, H., 2014. "Application of a hybrid breakup model for the spray simulation of a multi-hole injector used for a DISI gasoline engine". *Applied Thermal Engineering,* ***65***(1-2), pp. 282–292.

[59] Shen, S., Che, Z., Wang, T., Jia, M., and Sun, K., 2017. "Numerical Study on Flash Boiling Spray of Multi-Hole Injector". *SAE International Journal of Fuels and Lubricants,* ***10***(2), pp. 2017–01–0841.

[60] Bharadwaj, N., 2010. "Large Eddy Simulation Turbulence Modeling of Spray Flows". PhD thesis.

[61] Van Dam, N., and Rutland, C., 2016. "Adapting diesel large-eddy simulation spray models for direct-injection spark-ignition applications". *International Journal of Engine Research,* ***17***(3), pp. 291–315.

[62] Bode, M., Falkenstein, T., Chenadec, V. L., Kang, S., Pitsch, H., Arima, T., and Taniguchi, H., 2015. "A New Euler/Lagrange Approach for Multiphase Simulations of a Multi-Hole GDI Injector". *SAE 2015 World Congress & Exhibition*.

[63] Bode, M., Falkenstein, T., Davidovic, M., Pitsch, H., Taniguchi, H., Murayama, K., Arima, T., Moon, S., Wang, J., and Arioka, A., 2017. "Effects of Cavitation and Hydraulic Flip in 3-Hole GDI Injectors". *SAE International Journal of Fuels and Lubricants,* ***10***(2), pp. 2017–01–0848.

[64] Gosman, A. D., and Loannides, E., 1983. "Aspects of Computer Simulation of Liquid-Fueled Combustors". *Journal of Energy,* ***7***(6), pp. 482–490.

[65] Kuerten, J. G., 2006. "Subgrid modeling in particle-laden channel flow". *Physics of Fluids,* ***18***(2).

[66] Shotorban, B., and Mashayek, F., 2005. "Modeling subgrid-scale effects on particles by approximate deconvolution". *Physics of Fluids,* ***17***(8), pp. 1–4.

[67] Pozorski, J., and Apte, S. V., 2009. "Filtered particle tracking in isotropic turbulence and stochastic modeling of subgrid-scale dispersion". *International Journal of Multiphase Flow,* ***35***(2), pp. 118–128.

[68] Tsang, C. W., Kuo, C. W., Trujillo, M., and Rutland, C., 2018. "Evaluation and validation of large-eddy simulation sub-grid spray dispersion models using high-fidelity volume-of-fluid simulation data and engine combustion network experimental data". *International Journal of Engine Research*.

[69] Pomraning, E., and Rutland, C. J., 2002. "Dynamic One-Equation Nonviscosity Large-Eddy Simulation Model". *AIAA Journal,* ***40***(4).

[70] Ghosal, S., Lund, T. S., Moin, P., and Akselvoll, K., 1995. "A dynamic localization model for large-eddy simulation of turbulent flows". *Journal of Fluid Mechanics,* ***286***, pp. 229–255.

[71] Chumakov, S. G., and Rutland, C. J., 2005. "Dynamic structure subgrid-scale models for large eddy simulation". *International Journal for Numerical Methods in Fluids,* ***47***(8-9), pp. 911–923.

[72] Chumakov, S. G., 2007. "Scaling properties of subgrid-scale energy dissipation". *Physics of Fluids,* ***19***(5).

[73] Chumakov, S. G., 2005. "Subgrid models for large eddy simulation: scalar flux, scalar dissipation and energy dissipation". *Thesis*, p. 135.

[74] Van Romunde, R., 2011. "Factors affecting the development of sprays produced by multihole injectors for direct-injection engine applications". *Doctoral thesis, UCL (University College London).*

[75] Tsang, C. W., Trujillo, M. F., and Rutland, C. J., 2014. "Large-eddy simulation of shear flows and high-speed vaporizing liquid fuel sprays". *Computers and Fluids, **105***, pp. 262–279.

[76] Bharadwaj, N., Rutland, C. J., and Chang, S., 2009. "Large eddy simulation modelling of spray-induced turbulence effects". *International Journal of Engine Research, **10***(2), pp. 97–119.

[77] Lilly, D. K., 1967. "The Representation of Small-Scale Turbulence in Numerical Simulation Experiments". *Proceedings of the IBM Scientific Computing Symposium on Environmental Sciences*(November), pp. 195–210.

[78] Tsang, C.-w., 2013. "Large-eddy Simulation of Non-reacting Diesel Sprays".

[79] Siebers, D. L., 1999. "Scaling liquid-phase fuel penetration in diesel sprays based on mixing-limited vaporization". *SAE technical paper*(724), pp. 01–0528.

[80] Parrish, S. E., 2014. "Evaluation of Liquid and Vapor Penetration of Sprays from a Multi-Hole Gasoline Fuel Injector Operating Under Engine-Like Conditions". *SAE International Journal of Engines, **7***(2), pp. 2014–01–1409.

[81] Kulkarni, V., 2013. "An Analytical and Experimental Study of Secondary Atomization for Vibrational and Bag Breakup Modes". PhD thesis.

[82] Villermaux, E., and Bossa, B., 2009. "Single-drop fragmentation determines size distribution of raindrops". *Nature Physics,* ***5***(9), pp. 697–702.

[83] Li, H., and Rutland, C., 2017. "Uncertainty Quantification of Direct Injection Diesel and Gasoline Spray Simulations". In SAE International.

[84] Khosla, S., and Smith, C., 2006. "Detailed Understanding of Drop Atomization by Gas Crossflow Using the Volume of Fluid Method". *ILASS Americas*(May).

[85] MacInnes, J. M., and Bracco, F. V., 1992. "Stochastic particle dispersion modeling and the tracer-particle limit". *Physics of Fluids A,* ***4***(12), pp. 2809–2824.

[86] Stolz, S., Adams, N. A., and Kleiser, L., 2001. "An approximate deconvolution model for large-eddy simulation with application to incompressible wall-bounded flows". *Physics of Fluids,* ***13***(4), pp. 997–1015.

[87] Apte, S. V., Gorokhovski, M., and Moin, P., 2003. "LES of atomizing spray with stochastic modeling of secondary breakup". *International Journal of Multiphase Flow,* ***29***(9), pp. 1503–1522.

[88] Sphicas, P., Pickett, L. M., Skeen, S. A., and Frank, J. H., 2017. "Inter-plume aerodynamics for gasoline spray collapse". *International Journal of Engine Research*, p. 146808741774030.

[89] ECN. Engine Combustion Network(ECN): Diesel Spray Data Search. https://ecn.sandia.gov/diesel-spray-combustion/experimental-data-search/.

[90] Parrish, S. E., and Zink, R. J., 2012. "Development and Application of Imaging System To Evaluate Liquid and Vapor Envelopes of Multi-Hole Gasoline Fuel Injector Sprays Under Engine-Like Conditions". *Atomization and Sprays,* ***22***(8), pp. 647–661.

[91] Dam, N. E. V., 2015. "Large-eddy Simulations of Direct-injection Spark-ignition Engine Spray and Flow Variability".

[92] Weller, H. G., Tabor, G., Jasak, H., and Fureby, C., 1998. "A tensorial approach to computational continuum mechanics using object-oriented techniques". *Computers in Physics,* ***12***(6), p. 620.

[93] Holzmann, T., 2016. *Mathematics, Numerics, Derivations and OpenFOAM®*. Holzmann CFD.

[94] ECN, 2018. Engine Combustion Network(ECN): Details of the Fluid Mechanic Conditions in the Combustion Vessel. https://ecn.sandia.gov/velocity-distribution/.

[95] Sphicas, P., Pickett, L. M., Skeen, S., Frank, J., Lucchini, T., Sinoir, D., D'Errico, G., Saha, K., and Som, S., 2017. "A Comparison of Experimental and Modeled Velocity in Gasoline Direct-Injection Sprays with Plume Interaction and Collapse". *SAE International Journal of Fuels and Lubricants,* ***10***(1), pp. 2017–01–0837.

[96] ECN, 2018. Engine Combustion Network(ECN): Injector Characterization: 2007 - Present. https://ecn.sandia.gov/diesel-spray-combustion/sandia-cv/injector-characterization/2007-to-present/.

[97] Payri, R., Gimeno, J., Marti-Aldaravi, P., and Vaquerizo, D., 2015. "Momentum Flux Measurements on an ECN GDi Injector".

[98] Manin, J., Skeen, S. A., Pickett, L. M., Parrish, S. E., and Markle, L. E., 2015. "Experimental Characterization of DI Gasoline Injection Processes".

[99] Pickett, L. M., 2016. "Spray G Langrangian Modeling". In ECN 5 proceedings.

[100] Ranz, W. E. and Marshall, W. R., 1952. "Evaporation from Drops". *Chemical Engineering Progress,* ***48***.

[101] Malcolm W. Chase, J., 1998. *NIST-JANAF thermochemical tables*. Fourth edition. Washington, DC : American Chemical Society ; New York : American Institute of Physics for the National Institute of Standards and Technology, 1998.

[102] Lucchini;, T., Paredi;, D., and Lacey, J., 2018. "Topic 10: Evaporative Spray G (external, plume interaction, flash boiling)". In ECN 6 proceedings.

[103] Parrish, S., 2014. "Gasoline Spray (Spray G) Topic 3.4 Drop Size Measurement". In Engine Combustion Network 3rd Workshop, Engine Combustion Network.

[104] ECN, 2018. Engine Combustion Network(ECN): Gasoline Data Search. https://ecn.sandia.gov/gasoline-spray-combustion/experimental-data-search/.

[105] ECN. Modeling Standards and Recommendations.

[106] Lavision, 2018. Techniques Mie/Rayleigh/Raman. https://www.lavision.de/en/techniques/mie-rayleigh-raman/.

[107] ECN, 2018. Engine Combustion Network(ECN): Liquid Penetration Length. https://ecn.sandia.gov/gasoline-spray-combustion/experimental-diagnostics/liquid-penetration-length/.

[108] Van Dam, N., and Rutland, C., 2016. "Uncertainty Quantification of Large-Eddy Spray Simulations". *Journal of Verification, Validation and Uncertainty Quantification,* ***1***(2), p. 021006.

[109] Rotondi, R., and Bella, G., 2006. "Gasoline direct injection spray simulation". *International Journal of Thermal Sciences,* ***45***(2), pp. 168–179.

[110] Blessinger, M., Manin, J., Skeen, S. A., Meijer, M., Parrish, S., and Pickett, L. M., 2015. "Quantitative mixing measurements and stochastic variability of a vaporizing gasoline direct-injection spray". *International Journal of Engine Research,* ***16***(2), pp. 238–252.

[111] McKay, M. D., Beckman, R. J., and Conover, W. J., 1979. "Comparison of Three Methods for Selecting Values of Input Variables in the Analysis of Output from a Computer Code". *Technometrics,* ***21***(2), pp. 239–245.

[112] Adams, B. M., Ebeida, M. S., Eldred, M. S., Jakeman, J. D., Swiler, L. P., and Eddy, J. P., 2014. Dakota , A Multilevel Parallel Object-Oriented Framework for Design Optimization , Parameter Estimation , Uncertainty Quantification , and Sensitivity Analysis Version 5 . 4 User ' s Manual. Tech. Rep. December 2009.

[113] Trujillo, M. F., and Parkhill, A. E., 2011. "A local lagrangian analysis of passive particle advection in a gas flow field". *International Journal of Multiphase Flow,* ***37***(9), pp. 1201–1208.

[114] Faragher, J., 2004. Probabilistic Methods for the Quantification of Uncertainty and Error in Computational Fluid Dynamics Simulations.

[115] Najm, H. N., 2009. "Uncertainty Quantification and Polynomial Chaos Techniques in Computational Fluid Dynamics". *Annual Review of Fluid Mechanics,* ***41***(1), pp. 35–52.

[116] Bungartz, H. J., and Griebel, M., 2004. "Sparse grids". *Acta Numerica,* ***13***, pp. 147–269.

[117] Trucano, T., Swiler, L., Igusa, T., Oberkampf, W., and Pilch, M., 2006. "Dakota, A Multilevel Parallel Object-Oriented Framework for Design Optimization, Parameter Estimation, Uncertainty Quantification, and Sensitivity Analysis". *Reliability Engineering & System Safety,* ***91***(10-11), pp. 1331–1357.

[118] Marzban, C., 2013. "Variance-Based Sensitivity Analysis: An Illustration on the Lorenz'63 Model". *Monthly Weather Review,* ***141***(11), pp. 4069–4079.

A.1 Uncertainty quantification methods

Latin Hypercube Sampling

LHS is a "constrained sampling" method in which the selection of sampling points is highly constrained. The first half of the name, "Latin hypercube", came from the idea of Latin squares that have been widely used in experimental design. A Latin square is an $n \times n$ matrix filled with n different colors, each occurring exactly once in each row and exactly once in each column. The second half of the name refers to a parameter space of size N^M with M parameters ($M > 3$) and N segments [114].

In LHS, the range of each uncertain variable is divided into N segments of equal probability. The length of each segment is determined by a user-specified PDF. For example, a "uniform" PDF specifies that the uncertain variable is divided into N bins each with the same length. For M uncertain variables, this partitioning will yield a total of N^M bins in the parameter space. Following the partitioning, N bins are sampled by randomly selecting one bin from each uncertain variable PDF, and repeating this step N times without replacement. A detailed description of the algorithm and its implementation in Dakota can be found in Ref. [112].

One advantage of LHS is that the full range of uncertain variables is covered, i.e., random samples are generated from all the ranges of possible values. However, accurate estimation of response function statistics is not guaranteed unless a large number of evaluations are made. LHS requires about five times fewer samples than the Monte Carlo (MC) method and is considered very useful when uncertain variables have small

disturbances rather than large, sudden changes [114].

Polynomial Chaos Expansions

Unlike LHS which estimates point probabilities, deterministic methods like PCE form approximations to express the functional relationships between response functions and uncertain variables. Dakota implemented the generalized polynomial chaos approach using Wiener-Askey scheme. A brief overview of PCE is adapted from Ref. [115] and provided here.

In PCE, effects of continuous random variables are modeled by orthogonal polynomials. We can represent this with truncated PCE written as

$$X \approx \sum_{k=0}^{M} \zeta_k(x,t)\Psi_k(\xi_1, \xi_2, ..., \xi_n). \tag{A.1}$$

where Ψ_k are multivariate polynomials from a set of random variables $\xi = (\xi_1, \xi_2, ..., \xi_n)$, ζ_k are mode strengths, X is response variable, and M is number of terms.

Dakota propagates the polynomial chaos represented uncertainties using a non-intrusive approach, in which the calculation of mode strengths is based on response functions from a set of simulations. The spectral projection approach is used in this study to calculate these mode strengths. This approach takes the inner products between response variables and basis polynomials and employs the polynomial orthogonality to calculate mode strengths, which can be written as

$$\zeta_k = \frac{1}{\langle \Psi_k^2 \rangle} \frac{1}{N} \sum_{j=1}^{N} X_j \Psi_k(\xi), \quad k = 0, 1, ..., P \tag{A.2}$$

where N is number of samples.

The advantage of non-intrusive approach is that it does not require modification to the CFD code. However, it may require many simulations to achieve a certain convergence criterion. To retain a reasonable number of samples, Smolyak sparse grids were used in this study. This approach has a weak dependence on problem dimensionality, thus overcomes the "curse of dimension" to some extent [116].

A.2 Uncertainty quantification statistics

Correlation Coefficient

Results of LHS include four types of correlation coefficients, i.e., simple correlations among all inputs and outputs, partial correlations between each input and output, and simple and partial "Rank" correlations. Simple and partial correlations are computed based on the actual values of inputs and outputs. Rank correlations are computed on input and output ranks, which are obtained by replacing the actual value by ranks. For example, the smallest value would be given a rank one, the second smallest value would be given a rank two, etc. [112].

The simple correlation is Pearson's correlation coefficient, which is defined for two variables a and b as

$$\varrho_{a,b} = \frac{\sum_{i=1}^{m}(a_i - \bar{a})(b_i - \bar{b})}{\sqrt{\sum_{i=1}^{m}(a_i - \bar{a})^2}\sqrt{\sum_{i=1}^{m}(b_i - \bar{b})^2}}, \tag{A.3}$$

where m, ¯ represent the size and mean of each variable, respectively.

The correlation coefficient ranges from +1 to -1. A value of +1 implies a positive

linear relationship between two variables. A value of -1 implies a negative linear relationship. A value of zero implies that there is no linear correlation between the variables. The partial correlation coefficient is similar to simple correlation, but partial correlation measures the correlation while taking away the effects of one or more additional variables.

The rank coefficient in Dakota is computed using Spearman's rank correlation, which is same as Pearson's correlation except that it is obtained based on the ranks.

Sobol's Indices

For SE techniques like PCE, Dakota also has the capability to calculate variance-based sensitivity indices through Variance-based Decomposition (VBD). VBD is a global sensitivity analysis method which decomposes the variance of response function X into fractions which can be attributed to uncertainties in each individual input variables ξ_i. VBD uses two primary measures, namely main effect index S_i and total effect index T_i. These two measures are also referred to as Sobol's indices.

The main effect sensitivity index corresponds to contribution to the output variance by varying ξ_i alone. The total effect index corresponds to contribution to the output variance caused by varying ξ_i and its interactions with other uncertain variables [117, 118]. Formulas for these two indices are

$$S_i = \frac{V[E(X|\xi_i)]}{V[X]} \tag{A.4}$$

$$T_i = \frac{V[X] - V[E(X|\xi_{\sim i})]}{V[X]} \tag{A.5}$$

where $E[\cdot]$ and $V(\cdot)$ are expected value and variance, respectively, $E[Y|\xi_i]$ and $V(Y|\xi_i)$

are conditional expected value and conditional variance, respectively, and $\xi_{\sim i} = (\xi_1, \xi_2, \xi_{(i-1)}, \xi_{(i+1)}, \ldots, \xi_n)$.